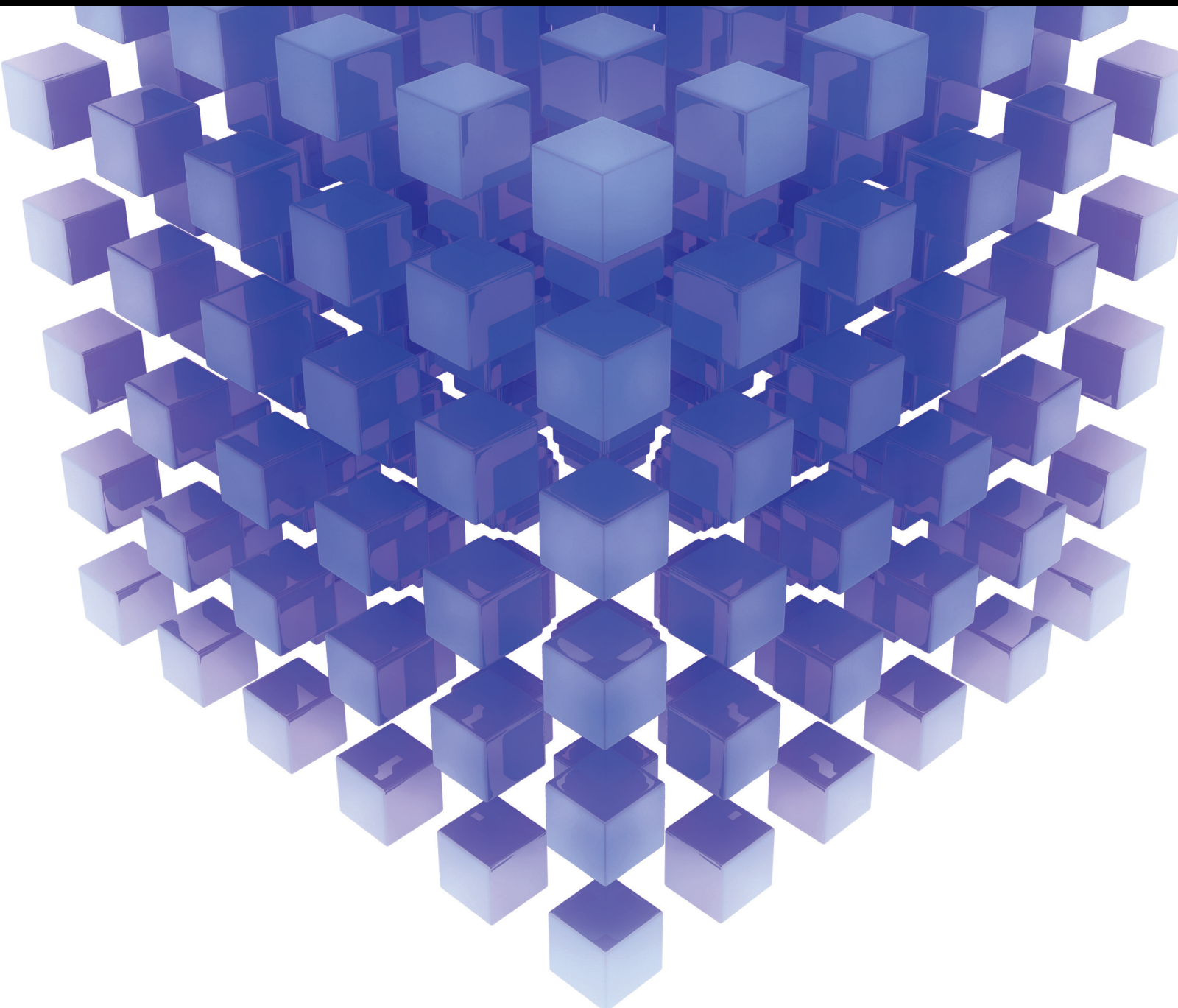# Complex Problem Solving with Digital Technologies

Lead Guest Editor: Zhihan Lv
Guest Editors: Jaime Lloret, Kaoru Ota, Paolo Bellavista, and Wei Xiang

Complex Problem Solving with Digital Technologies

Complex Problem Solving with Digital Technologies

Lead Guest Editor: Zhihan Lv
Guest Editors: Jaime Lloret, Kaoru Ota, Paolo Bellavista, and Wei Xiang

Chief Editor

Academic Editors

Paolo Boscariol, Italy
Daniela Boso (iD), Italy
Guillermo Botella-Juan, Spain
Abdesselem Boulkroune (iD), Algeria
Boulaïd Boulkroune, Belgium
Fabio Bovenga (iD), Italy
Francesco Braghin (iD), Italy
Ricardo Branco, Portugal
Julien Bruchon (iD), France
Matteo Bruggi (iD), Italy
Michele Brun (iD), Italy
Maria Elena Bruni, Italy
Maria Angela Butturi (iD), Italy
Bartłomiej Błachowski (iD), Poland
Dhanamjayulu C (iD), India
Raquel Caballero-Águila (iD), Spain
Filippo Cacace (iD), Italy
Salvatore Caddemi (iD), Italy
Zuowei Cai (iD), China
Roberto Caldelli (iD), Italy
Francesco Cannizzaro (iD), Italy
Maosen Cao (iD), China
Ana Carpio, Spain
Rodrigo Carvajal (iD), Chile
Caterina Casavola, Italy
Sara Casciati, Italy
Federica Caselli (iD), Italy
Carmen Castillo (iD), Spain
Inmaculada T. Castro (iD), Spain
Miguel Castro (iD), Portugal
Giuseppe Catalanotti (iD), United Kingdom
Alberto Cavallo (iD), Italy
Gabriele Cazzulani (iD), Italy
Fatih Vehbi Celebi, Turkey
Miguel Cerrolaza (iD), Venezuela
Gregory Chagnon (iD), France
Ching-Ter Chang (iD), Taiwan
Kuei-Lun Chang (iD), Taiwan
Qing Chang (iD), USA
Xiaoheng Chang (iD), China
Prasenjit Chatterjee (iD), Lithuania
Kacem Chehdi, France
Peter N. Cheimets, USA
Chih-Chiang Chen (iD), Taiwan
He Chen (iD), China

Kebing Chen (iD), China
Mengxin Chen (iD), China
Shyi-Ming Chen (iD), Taiwan
Xizhong Chen (iD), Ireland
Xue-Bo Chen (iD), China
Zhiwen Chen (iD), China
Qiang Cheng, USA
Zeyang Cheng, China
Luca Chiapponi (iD), Italy
Francisco Chicano (iD), Spain
Tirivanhu Chinyoka (iD), South Africa
Adrian Chmielewski (iD), Poland
Seongim Choi (iD), USA
Gautam Choubey (iD), India
Hung-Yuan Chung (iD), Taiwan
Yusheng Ci, China
Simone Cinquemani (iD), Italy
Roberto G. Citarella (iD), Italy
Joaquim Ciurana (iD), Spain
John D. Clayton (iD), USA
Piero Colajanni (iD), Italy
Giuseppina Colicchio, Italy
Vassilios Constantoudis (iD), Greece
Enrico Conte, Italy
Alessandro Contento (iD), USA
Mario Cools (iD), Belgium
Gino Cortellessa, Italy
Carlo Cosentino (iD), Italy
Paolo Crippa (iD), Italy
Erik Cuevas (iD), Mexico
Guozeng Cui (iD), China
Mehmet Cunkas (iD), Turkey
Giuseppe D'Aniello (iD), Italy
Peter Dabnichki, Australia
Weizhong Dai (iD), USA
Zhifeng Dai (iD), China
Purushothaman Damodaran (iD), USA
Sergey Dashkovskiy, Germany
Adiel T. De Almeida-Filho (iD), Brazil
Fabio De Angelis (iD), Italy
Samuele De Bartolo (iD), Italy
Stefano De Miranda (iD), Italy
Filippo De Monte (iD), Italy

José António Fonseca De Oliveira Correia, Portugal
Jose Renato De Sousa, Brazil
Michael Defoort, France
Alessandro Della Corte, Italy
Laurent Dewasme, Belgium
Sanku Dey, India
Gianpaolo Di Bona, Italy
Roberta Di Pace, Italy
Francesca Di Puccio, Italy
Ramón I. Diego, Spain
Yannis Dimakopoulos, Greece
Hasan Dinçer, Turkey
José M. Domínguez, Spain
Georgios Dounias, Greece
Bo Du, China
Emil Dumic, Croatia
Madalina Dumitriu, United Kingdom
Premraj Durairaj, India
Saeed Eftekhar Azam, USA
Said El Kafhali, Morocco
Antonio Elipe, Spain
R. Emre Erkmen, Canada
John Escobar, Colombia
Leandro F. F. Miguel, Brazil
FRANCESCO FOTI, Italy
Andrea L. Facci, Italy
Shahla Faisal, Pakistan
Giovanni Falsone, Italy
Hua Fan, China
Jianguang Fang, Australia
Nicholas Fantuzzi, Italy
Muhammad Shahid Farid, Pakistan
Hamed Faroqi, Iran
Yann Favennec, France
Fiorenzo A. Fazzolari, United Kingdom
Giuseppe Fedele, Italy
Roberto Fedele, Italy
Baowei Feng, China
Mohammad Ferdows, Bangladesh
Arturo J. Fernández, Spain
Jesus M. Fernandez Oro, Spain
Francesco Ferrise, Italy
Eric Feulvarch, France
Thierry Floquet, France

Eric Florentin, France
Gerardo Flores, Mexico
Antonio Forcina, Italy
Alessandro Formisano, Italy
Francesco Franco, Italy
Elisa Francomano, Italy
Juan Frausto-Solis, Mexico
Shujun Fu, China
Juan C. G. Prada, Spain
HECTOR GOMEZ, Chile
Matteo Gaeta, Italy
Mauro Gaggero, Italy
Zoran Gajic, USA
Jaime Gallardo-Alvarado, Mexico
Mosè Gallo, Italy
Akemi Gálvez, Spain
Maria L. Gandarias, Spain
Hao Gao, Hong Kong
Xingbao Gao, China
Yan Gao, China
Zhiwei Gao, United Kingdom
Giovanni Garcea, Italy
José García, Chile
Harish Garg, India
Alessandro Gasparetto, Italy
Stylianos Georgantzinos, Greece
Fotios Georgiades, India
Parviz Ghadimi, Iran
Ştefan Cristian Gherghina, Romania
Georgios I. Giannopoulos, Greece
Agathoklis Giaralis, United Kingdom
Anna M. Gil-Lafuente, Spain
Ivan Giorgio, Italy
Gaetano Giunta, Luxembourg
Jefferson L.M.A. Gomes, United Kingdom
Emilio Gómez-Déniz, Spain
Antonio M. Gonçalves de Lima, Brazil
Qunxi Gong, China
Chris Goodrich, USA
Rama S. R. Gorla, USA
Veena Goswami, India
Xunjie Gou, Spain
Jakub Grabski, Poland

Francisco J. Martos, Spain
Elio Masciari, Italy
Paolo Massioni, France
Alessandro Mauro, Italy
Jonathan Mayo-Maldonado, Mexico
Pier Luigi Mazzeo, Italy
Laura Mazzola, Italy
Driss Mehdi, France
Zahid Mehmood, Pakistan
Roderick Melnik, Canada
Xiangyu Meng, USA
Jose Merodio, Spain
Alessio Merola, Italy
Mahmoud Mesbah, Iran
Luciano Mescia, Italy
Laurent Mevel, France
Constantine Michailides, Cyprus
Mariusz Michta, Poland
Prankul Middha, Norway
Aki Mikkola, Finland
Giovanni Minafò, Italy
Edmondo Minisci, United Kingdom
Hiroyuki Mino, Japan
Dimitrios Mitsotakis, New Zealand
Ardashir Mohammadzadeh, Iran
Francisco J. Montáns, Spain
Francesco Montefusco, Italy
Gisele Mophou, France
Rafael Morales, Spain
Marco Morandini, Italy
Javier Moreno-Valenzuela, Mexico
Simone Morganti, Italy
Caroline Mota, Brazil
Aziz Moukrim, France
Shen Mouquan, China
Dimitris Mourtzis, Greece
Emiliano Mucchi, Italy
Taseer Muhammad, Saudi Arabia
Ghulam Muhiuddin, Saudi Arabia
Amitava Mukherjee, India
Josefa Mula, Spain
Jose J. Muñoz, Spain
Giuseppe Muscolino, Italy
Marco Mussetta, Italy

Hariharan Muthusamy, India
Alessandro Naddeo, Italy
Raj Nandkeolyar, India
Keivan Navaie, United Kingdom
Soumya Nayak, India
Adrian Neagu, USA
Erivelton Geraldo Nepomuceno, Brazil
AMA Neves, Portugal
Ha Quang Thinh Ngo, Vietnam
Nhon Nguyen-Thanh, Singapore
Papakostas Nikolaos, Ireland
Jelena Nikolic, Serbia
Tatsushi Nishi, Japan
Shanzhou Niu, China
Ben T. Nohara, Japan
Mohammed Nouari, France
Mustapha Nourelfath, Canada
Kazem Nouri, Iran
Ciro Núñez-Gutiérrez, Mexico
Wlodzimierz Ogryczak, Poland
Roger Ohayon, France
Krzysztof Okarma, Poland
Mitsuhiro Okayasu, Japan
Murat Olgun, Turkey
Diego Oliva, Mexico
Alberto Olivares, Spain
Enrique Onieva, Spain
Calogero Orlando, Italy
Susana Ortega-Cisneros, Mexico
Sergio Ortobelli, Italy
Naohisa Otsuka, Japan
Sid Ahmed Ould Ahmed Mahmoud,
Saudi Arabia
Taoreed Owolabi, Nigeria
EUGENIA PETROPOULOU, Greece
Arturo Pagano, Italy
Madhumangal Pal, India
Pasquale Palumbo, Italy
Dragan Pamučar, Serbia
Weifeng Pan, China
Chandan Pandey, India
Rui Pang, United Kingdom
Jürgen Pannek, Germany
Elena Panteley, France
Achille Paolone, Italy

Bekir Sahin, Turkey
Laxminarayan Sahoo, India
John S. Sakellariou, Greece
Michael Sakellariou, Greece
Salvatore Salamone, USA
Jose Vicente Salcedo, Spain
Alejandro Salcido, Mexico
Alejandro Salcido, Mexico
Nunzio Salerno, Italy
Rohit Salgotra, India
Miguel A. Salido, Spain
Sinan Salih, Iraq
Alessandro Salvini, Italy
Abdus Samad, India
Sovan Samanta, India
Nikolaos Samaras, Greece
Ramon Sancibrian, Spain
Giuseppe Sanfilippo, Italy
Omar-Jacobo Santos, Mexico
J Santos-Reyes, Mexico
José A. Sanz-Herrera, Spain
Musavarah Sarwar, Pakistan
Shahzad Sarwar, Saudi Arabia
Marcelo A. Savi, Brazil
Andrey V. Savkin, Australia
Tadeusz Sawik, Poland
Roberta Sburlati, Italy
Gustavo Scaglia, Argentina
Thomas Schuster, Germany
Hamid M. Sedighi, Iran
Mijanur Rahaman Seikh, India
Tapan Senapati, China
Lotfi Senhadji, France
Junwon Seo, USA
Michele Serpilli, Italy
Silvestar Šesnić, Croatia
Gerardo Severino, Italy
Ruben Sevilla, United Kingdom
Stefano Sfarra, Italy
Dr. Ismail Shah, Pakistan
Leonid Shaikhet, Israel
Vimal Shanmuganathan, India
Prayas Sharma, India
Bo Shen, Germany
Hang Shen, China

Xin Pu Shen, China
Dimitri O. Shepelsky, Ukraine
Jian Shi, China
Amin Shokrollahi, Australia
Suzanne M. Shontz, USA
Babak Shotorban, USA
Zhan Shu, Canada
Angelo Sifaleras, Greece
Nuno Simões, Portugal
Mehakpreet Singh, Ireland
Piyush Pratap Singh, India
Rajiv Singh, India
Seralathan Sivamani, India
S. Sivasankaran, Malaysia
Christos H. Skiadas, Greece
Konstantina Skouri, Greece
Neale R. Smith, Mexico
Bogdan Smolka, Poland
Delfim Soares Jr., Brazil
Alba Sofi, Italy
Francesco Soldovieri, Italy
Raffaele Solimene, Italy
Yang Song, Norway
Jussi Sopanen, Finland
Marco Spadini, Italy
Paolo Spagnolo, Italy
Ruben Specogna, Italy
Vasilios Spitas, Greece
Ivanka Stamova, USA
Rafał Stanisławski, Poland
Miladin Stefanović, Serbia
Salvatore Strano, Italy
Yakov Strelniker, Israel
Kangkang Sun, China
Qiuqin Sun, China
Shuaishuai Sun, Australia
Yanchao Sun, China
Zong-Yao Sun, China
Kumarasamy Suresh, India
Sergey A. Suslov, Australia
D.L. Suthar, Ethiopia
D.L. Suthar, Ethiopia
Andrzej Swierniak, Poland
Andras Szekrenyes, Hungary
Kumar K. Tamma, USA

Yong (Aaron) Tan, United Kingdom
Marco Antonio Taneco-Hernández (iD), Mexico
Lu Tang (iD), China
Tianyou Tao, China
Hafez Tari (iD), USA
Alessandro Tasora (iD), Italy
Sergio Teggi (iD), Italy
Adriana del Carmen Téllez-Anguiano (iD), Mexico
Ana C. Teodoro (iD), Portugal
Efstathios E. Theotokoglou (iD), Greece
Jing-Feng Tian, China
Alexander Timokha (iD), Norway
Stefania Tomasiello (iD), Italy
Gisella Tomasini (iD), Italy
Isabella Torcicollo (iD), Italy
Francesco Tornabene (iD), Italy
Mariano Torrisi (iD), Italy
Thang nguyen Trung, Vietnam
George Tsiatas (iD), Greece
Le Anh Tuan (iD), Vietnam
Nerio Tullini (iD), Italy
Emilio Turco (iD), Italy
Ilhan Tuzcu (iD), USA
Efstratios Tzirtzilakis (iD), Greece
FRANCISCO UREÑA (iD), Spain
Filippo Ubertini (iD), Italy
Mohammad Uddin (iD), Australia
Mohammad Safi Ullah (iD), Bangladesh
Serdar Ulubeyli (iD), Turkey
Mati Ur Rahman (iD), Pakistan
Panayiotis Vafeas (iD), Greece
Giuseppe Vairo (iD), Italy
Jesus Valdez-Resendiz (iD), Mexico
Eusebio Valero, Spain
Stefano Valvano (iD), Italy
Carlos-Renato Vázquez (iD), Mexico
Martin Velasco Villa (iD), Mexico
Franck J. Vernerey, USA
Georgios Veronis (iD), USA
Vincenzo Vespri (iD), Italy
Renato Vidoni (iD), Italy
Venkatesh Vijayaraghavan, Australia

Anna Vila, Spain
Francisco R. Villatoro (iD), Spain
Francesca Vipiana (iD), Italy
Stanislav Vítek (iD), Czech Republic
Jan Vorel (iD), Czech Republic
Michael Vynnycky (iD), Sweden
Mohammad W. Alomari, Jordan
Roman Wan-Wendner (iD), Austria
Bingchang Wang, China
C. H. Wang (iD), Taiwan
Dagang Wang, China
Guoqiang Wang (iD), China
Huaiyu Wang, China
Hui Wang (iD), China
J.G. Wang, China
Ji Wang (iD), China
Kang-Jia Wang (iD), China
Lei Wang (iD), China
Qiang Wang, China
Qingling Wang (iD), China
Weiwei Wang (iD), China
Xinyu Wang (iD), China
Yong Wang (iD), China
Yung-Chung Wang (iD), Taiwan
Zhenbo Wang (iD), USA
Zhibo Wang, China
Waldemar T. Wójcik, Poland
Chi Wu (iD), Australia
Qiuhong Wu, China
Yuqiang Wu, China
Zhibin Wu (iD), China
Zhizheng Wu (iD), China
Michalis Xenos (iD), Greece
Hao Xiao (iD), China
Xiao Ping Xie (iD), China
Qingzheng Xu (iD), China
Binghan Xue (iD), China
Yi Xue (iD), China
Joseph J. Yame (iD), France
Chuanliang Yan (iD), China
Xinggang Yan (iD), United Kingdom
Hongtai Yang (iD), China
Jixiang Yang (iD), China
Mijia Yang, USA
Ray-Yeng Yang, Taiwan

Zaoli Yang, China

Jun Ye, China

Min Ye, China

Luis J. Yebra, Spain

Peng-Yeng Yin, Taiwan

Muhammad Haroon Yousaf, Pakistan

Yuan Yuan, United Kingdom

Qin Yuming, China

Elena Zaitseva, Slovakia

Arkadiusz Zak, Poland

Mohammad Zakwan, India

Ernesto Zambrano-Serrano, Mexico

Francesco Zammori, Italy

Jessica Zangari, Italy

Rafal Zdunek, Poland

Ibrahim Zeid, USA

Nianyin Zeng, China

Junyong Zhai, China

Hao Zhang, China

Haopeng Zhang, USA

Jian Zhang, China

Kai Zhang, China

Lingfan Zhang, China

Mingjie Zhang, Norway

Qian Zhang, China

Tianwei Zhang, China

Tongqian Zhang, China

Wenyu Zhang, China

Xianming Zhang, Australia

Xuping Zhang, Denmark

Yinyan Zhang, China

Yifan Zhao, United Kingdom

Debao Zhou, USA

Heng Zhou, China

Jian G. Zhou, United Kingdom

Junyong Zhou, China

Xueqian Zhou, United Kingdom

Zhe Zhou, China

Wu-Le Zhu, China

Gaetano Zizzo, Italy

Mingcheng Zuo, China

Contents

Research Article

Test on the Policy Effect of Natural Forest Protection Project Using Double Difference Model from the Perspective of Forestry Total Factor Productivity

Hui Yin and Yukun Cao [ID]

College of Economics and Management, Northeast Forestry University, Harbin 150040, China

Correspondence should be addressed to Yukun Cao; cyklk@163.com

As one of the largest forestry ecological protection projects in China, the natural forest protection project has been implemented for 20 years, and great changes have taken place in the natural resources and social appearance of the forest area. This article regards the implementation of the natural forest protection project as a policy impact and makes an objective evaluation of the implementation effect of the policy through measurement and accounting. Based on the panel data of forestry total factor productivity (TFP) in 31 provinces in China from 1997 to 2018, this article uses the double difference model to investigate the impact of the policy impact of natural forest protection projects on the implementation of provincial forestry TFP from the perspective of quasinatural experiment. The results show that the natural forest protection project significantly improves the TFP of forestry in the province where the policy is implemented, and the higher the forest resource coverage, the more significant the provincial impact of policy implementation. From other influencing factors, the reduction of human investment, the rationalization of industrial structure, and the improvement of the level of scientific, technological, and economic development can also effectively mend the TFP of forestry in the region.

1. Introduction and Literature Review

According to the results of the Ninth National Forest Resources Inventory (2014–2018), China's forest area is 220 million hectares hm^2, the forest coverage rate is 22.96% [1], and the forest volume is 17.56 billion m^3, realizing the "double growth" of forest area and volume [2] in the past 30 years. China's global contribution to forest protection and afforestation has been affirmed by the FAO. Since the 1980s, China has put forward and implemented a number of ecological plans, including the project of returning farmland to forests, the construction project of a farmland shelterbelt system in the Yangtze River and Pearl River basins, and the natural forest protection project (NFPP). After the catastrophic floods in the Yangtze River Basin, Songhua River, and Nenjiang river basins in 1998, China decided to carry out pilot projects of NFPP in key state-owned forest areas in

12 provinces (autonomous regions and cities) such as Yunnan. In 2000, the execution plan of NFPP in the upper reaches of the Yangtze River and the upper and middle reaches of the Yellow River was approved and implemented by the government, and then the implementation plan of NFPP in key state-owned forest areas such as the northeast and Inner Mongolia was issued. So far, NFPP has been implemented in key forest areas of 17 provinces (autonomous regions and cities) in China, including Yunnan, Sichuan Guizhou, Chongqing, Hubei and Tibet, Shaanxi, Gansu, Qinghai, Ningxia, Inner Mongolia, Shanxi and Henan in the upper and middle reaches of the Yellow River, and Jilin, Heilongjiang, Hainan, and Xinjiang in Northeast China. The execution of NFPP is aimed at the deterioration of the ecological environment caused by excessive consumption of natural forest resources in China for a long time. The government has made major decisions from the

perspective of social and economic sustainable development strategy [3]. As the largest forestry ecological protection project in China, the NFPP has been implemented for 20 years. The total investment of the government has exceeded 400 billion yuan [4], and great changes have been brought to pass in the natural resources and social outlook of the forest area.

Now, the first phase of the NFPP has been successfully completed. As the second phase of the project enters a critical period, there are many problems to be solved around the ecological protection project: how to objectively evaluate the execution effect of NFPP? If the implementation effect of the ecological protection project is significant, what influencing factors have a significant impact on it? Previous studies concentrate on the following three aspects: the first is a summary of the practice of natural forest protection engineering, which includes the implementation means and achievements of natural forest protection engineering. For example, Chen et al. [5] showed the time distribution and researched hotspot evolution of the natural forest protection engineering research field by drawing a visual knowledge map and revealed the overall context of natural forest protection engineering research in China; Cao et al. [6] systematically analyzed the main characteristics and methods of benefit evaluation of natural forest protection projects by combining the research literature on benefit evaluation of natural forest protection projects in China. The second is the research on the performance and value of NFPP. For example, Qin and Zhang [7] used the fuzzy comprehensive evaluation method to comprehensively evaluate the performance of phase II policy execution of NFPP in the Yichun forest region by constructing the comprehensive evaluation index system of policy implementation performance of NFPP; Cui et al. [8] used the relevant data and existing achievements of the natural conservation project in Jingbian County to construct the forest ecosystem service function evaluation index system and evaluate the forest ecosystem service function value of the natural conservation project in Jingbian County. The third is the research on the relevant impact of the natural protection project. For example, Zang et al. [9] used the panel data of 11 provinces in the west to study the impact of project construction on farmers' income using panel vector autoregression and impulse response analysis; Zhai et al. [10] used the forestry industry data of state-owned forest areas in Heilongjiang Province to analyze the impact of the execution of NFPP on the overall structure change of forestry industry in state-owned forest areas. It can be seen that most of the existing literature has focused on qualitative evaluation and analysis of NFPP through literature induction and sorting, there is a lack of quantitative evaluation based on quantitative accounting, and the research objects or panel data are mostly concentrated in natural forest protection projects in the west, northeast, and other regions, There are few studies on the evaluation of the implementation effect of the national natural forest protection project policy, especially the combination with forestry total factor productivity (TFP).

Therefore, this thesis attempts to use the multistage double difference method (did), use China's provincial panel data from 1997 to 2018, and from the perspective of forestry total factor productivity, regard the execution of NFPP as a policy impact, evaluate the implementation effect of the policy, and provide a reference for China's forest resources management and ecological resources protection.

2. Methods and Materials

2.1. Model Setting and Method Selection. For studying the policy effect of natural forest protection projects on forestry total factor productivity, this thesis selects the double difference method (DID) to verify the policy implementation areas. The application basis of the double difference model is to accurately divide the observation samples into the experimental group and the control group. In this article, the provinces implementing the natural forest protection project are selected as the "experimental group" and other provinces as the corresponding "control group." The DID regression equation is set as follows:

$$y_{it} = \alpha + \beta_1 d_i d_t + \beta_2 d_i + \beta_3 d_t + \mu_{it}. \tag{1}$$

Among the explanatory variables of the above formula, set the policy influence variable as y_{it}; the observation group is d representing the experimental group and the control group, respectively. The year of observation is d_t; μ_{it} is the residual term. On the premise of referring to relevant research, this article adds some control variables to the original basic model. The expanded DID equation is as follows:

$$Y_{pt} = \alpha + \beta_1 \text{Treat}_{pt} \times \text{Year}_{pt} + \beta_2 \text{Treat}_{pt} + \beta_3 \text{Year}_{pt}$$
$$+ \delta X_{pt} + \gamma_p + \eta_t + \mu_{pt}. \tag{2}$$

In the equation, the subscript p represents the province and t represents the observation year. In the assignment Treat_{pt}, 17 provinces or cities implementing ecological protection policies, including Gansu, Guizhou, and Chongqing, are experimental group 1, and other regions are the control group 0. Year_{pt} is the implementation year of the natural protection project, and the value assigned in 1998 and later is 1, and the other is 0; X_{pt} is the control variable; γ_p is the regional fixed effect; η_t is the year fixed effect; μ_{pt} is a random disturbance term. In equation (2), β_1 is the key concern coefficient; $\text{Treat}_{pt} \times \text{Year}_{pt}$, which is the multiplication variable reflecting the net effect of the policy. Secondly, parameter β_2 represents the time change of target variables between the experimental group and the control group if there is no natural forest protection engineering policy, and parameter β_3 represents the difference between the experimental group and the control group that does not change with time. Equation (2) includes regional dummy variables γ_p and year dummy variables η_t [11].

2.2. Index Selection and Data Source. The explanatory variable of this thesis is to measure the TFP of 31 provincial forestries in China through the Malmquist index DEA model with dynamic change in total factor productivity. Malmquist index takes t period as the base period, and the formula is as follows:

TABLE 1: Malmquist index and decomposition of average TFP of forestry in 31 provinces in China during 1997~2018.

Region	EFFCH	TECHCH	PECH	SECH	TFP
Shanxi	1.015	1.078	1.007	1.003	1.090
Inner Mongolia	1.046	1.019	1.000	1.046	1.052
Jilin	1.000	1.007	1.000	1.000	1.007
Heilongjiang	1.057	0.951	1.000	1.057	0.999
Henan	0.993	0.978	1.000	0.992	0.971
Hubei	1.014	1.015	0.996	1.018	1.025
Hainan	1.000	1.125	1.000	1.000	1.125
Chongqing	1.000	1.086	1.000	1.000	1.086
Sichuan	1.077	1.050	1.004	1.078	1.126
Guizhou	1.012	1.028	1.005	1.002	1.040
Yunnan	1.021	1.010	1.001	1.020	1.008
Xizang	1.000	1.004	1.000	1.000	1.004
Shanxi	0.981	0.980	0.994	0.983	0.948
Gansu	1.013	0.997	0.994	1.024	1.008
Qinghan	0.998	1.015	1.000	0.998	1.010
Ningxia	1.016	1.020	0.999	1.018	1.045
Xinjiang	1.010	1.041	1.003	1.008	1.051
Beijing	0.994	1.047	1.000	0.994	1.040
Tianjin	1.000	1.019	1.000	1.000	1.019
Hebei	1.001	1.042	1.000	1.001	1.042
Liaoning	1.007	1.007	1.004	0.997	1.003
Shanghai	1.000	1.046	1.000	1.000	1.046
Jiangsu	1.001	1.105	1.000	1.001	1.107
Zhejiang	1.000	1.161	1.000	1.000	1.161
Anhui	1.011	0.945	1.001	1.009	0.953
Fujian	1.008	1.079	1.000	1.008	1.080
Jiangxi	0.998	1.002	1.000	0.998	0.998
Shandong	1.000	1.040	1.000	1.000	1.040
Hunan	1.049	1.004	1.007	1.032	1.057
Guangdong	1.030	1.116	1.001	1.028	1.140
Guangxi	1.032	1.043	1.003	1.037	1.068
Average	1.012	1.034	1.001	1.011	1.043

Note. According to deap2 1, the software processing results are calculated according to the annual average.

$$\mathrm{MALM}_{v,t}^{t,t+1}\left(x^{t+1}, y^{t+1}, x^t, y^t\right) = \frac{D_v^{t+1}\left(x^{t+1}, y^{t+1}\right)}{D_v^t\left(x^t, y^t\right)} \times \left[\frac{D_v^t\left(x^t, y^t\right)}{D_c^t\left(x^t, y^t\right)} \cdot \frac{D_c^{t+1}\left(x^{t+1}, y^{t+1}\right)}{D_v^{t+1}\left(x^{t+1}, y^{t+1}\right)}\right] \times \left[\frac{D_c^t\left(x^{t+1}, y^{t+1}\right)}{D_c^{t+1}\left(x^{t+1}, y^{t+1}\right)} \cdot \frac{D_c^t\left(x^t, y^t\right)}{D_c^{t+1}\left(x^t, y^t\right)}\right],$$

$$= \mathrm{PECH}^{t,t+1} \times \mathrm{SECH}^{t,t+1} \times \mathrm{TECHCH}^{t,t+1},$$

$$= \mathrm{EFFCH}^{t,t+1} \times \mathrm{TECHCH}^{t,t+1}.$$

(3)

In the above formula, MALM is the TFP of forestry from t to $t+1$, PECH is the pure technical efficiency change index from t to $t+1$, SECH is the scale efficiency change index from t to $t+1$, TECHCH is the technical progress change index from t to $t+1$, and EFFCH is the technical efficiency change index from t to $t+1$. Moreover, x^t and x^{t+1} are the input vectors of units from t to $t+1$; y^t and y^{t+1} are the output vectors of units from t to $t+1$, respectively. $D^t(x^t, y^t)$ and $D^{t+1}(x^{t+1}, y^{t+1})$ are the reference distance functions based on the technologies in T and $T+1$, respectively. In the above formula, the subscript v is the assumption of variable returns to scale and C is the assumption of constant returns to scale. The calculation results are shown in Table 1.

After referring to the relevant research results, this thesis selects a series of control variables to determine the economic development level, urbanization level, opening-up level, scientific and technological development level, industrial modernization level, government intervention level, and natural disasters based on the three dimensions of natural forest protection project implementation system, management, and environment, taking into account the availability of data indicators, forestry human capital level, and other variables. The variable value is determined as the calculated ratio value. The logarithm of regional per capita GDP is used to represent the level of economic development, the urbanization rate of the permanent urban population in

TABLE 2: Descriptive statistics of samples during 1997~2018.

Variable	Mean value	SD	Minimum	Maximum	Sample capacity
Forestry TFP	1.0435	0.2558	0.3770	2.2530	651
Logarithm of regional per capita GDP	0.7296	0.9034	0.4271	2.6405	651
Population urbanization rate	0.4794	0.1627	0.1404	0.8961	651
Proportion of import and export trade volume	0.2928	0.3676	0.0168	1.7215	651
Investment in research and experimental development	223.4371	383.5977	0.1000	2,704.700	651
Proportion of output value of secondary and tertiary industries	0.4084	0.2351	0.0152	0.9521	651
Proportion of government supported investment	0.6422	0.2542	0.0691	1.0000	651
Area logarithm of forest diseases and insect pests	12.3041	1.1187	8.5839	14.5144	651
Average annual salary of on-the-job employees	2.7144	2.5151	0.3238	17.6654	651

TABLE 3: Regression results.

Variable	Model (1)	Model (2)	Model (3)	Model (4)	Model (5)
DID	0.1057**	0.0892**	0.0866**	0.0882**	0.0877**
	(0.0447)	(0.0431)	(0.0420)	(0.0410)	(0.0410)
Industrial structure		0.1272**	0.1275**	0.1206*	0.1149*
		(0.0616)	(0.0617)	(0.0625)	(0.0667)
lnpergdp		0.1699*	0.1699*	0.1534	0.1592
		(0.0945)	(0.0937)	(0.1003)	(0.1000)
RD		−0.0001*	−0.0001*	−0.0001*	−0.0001*
		(0.0000)	(0.0000)	(0.0000)	(0.0000)
Wage		−0.0155**	−0.0154**	−0.0150**	−0.0146**
		(0.0062)	(0.0062)	(0.0061)	(0.0062)
Urban-rate		0.0177	0.0319	0.0431	0.0309
		(0.2608)	(0.2850)	(0.2851)	(0.2793)
Trade-rate			−0.0243	−0.0441	−0.0449
			(0.0865)	(0.0868)	(0.0870)
Government intervention				−0.0542	−0.0535
				(0.0745)	(0.0745)
Natural disaster					−0.0103
					(0.0289)
_cons	1.0038***	1.0548***	1.0557***	1.0741***	1.2040***
	(0.0361)	(0.0934)	(0.0911)	(0.0950)	(0.3637)
R^2	0.2008	0.2191	0.2192	0.2203	0.2204
N	651	651	651	651	651

Standard errors in parentheses $*p < 0.1$, $**p < 0.05$, $***p < 0.01$.

the proportion of the total population is used to measure the level of urbanization, the proportion of import and export trade represents the degree of opening to the outside world, the investment of research and experimental development funds represents the level of scientific and technological development, and forestry is the second. The proportion of tertiary industry in the total output value of the forestry industry represents the industrial structure, the proportion of central government investment in the total forestry investment represents the degree of government intervention, the area of forest diseases and pests represents the situation of natural disasters, and the average annual salary of on-the-job employees represents the investment level of forestry human capital. The data are mainly from the China Urban Statistical Yearbook, forestry statistical yearbook, and database of the National Bureau of Statistics from 1998 to 2018. In this article, a total of 5859 samples from 31 provincial regions in China from 1998 to 2018 are selected for empirical verification; the descriptive statistics of specific variables are shown in Table 2.

3. Empirical Results

3.1. Empirical Results and Differential Analysis. In this article, control variables are gradually added to the model calculation to investigate the net effect of NFPP policies; the estimated results are shown in Table 3. After the gradual addition of control variables such as the implementation system, management, and environment of NFPP, the coefficient symbol and significance of explanatory variables have not changed essentially, indicating that the estimation results are stable. Because the empirical results are between 0.0866 and 0.1057, which is significant at the confidence level of 5%, they indicate that the execution of NFPP has significantly improved the total factor production efficiency of forestry in 17 provincial areas, such as Shanxi, Inner Mongolia, and Jilin. Among the control variables affecting the productivity improvement of natural forest protection project, industrial structure, human capital, scientific and technological development level, and economic development level have a significant impact. Among them, the

TABLE 4: Heterogeneity analysis and grouping regression results of forest resource coverage.

Variable	Heterogeneity analysis	Test group	Test group	Control group	Control group
DID	0.1175**	0.1505**	0.1175*	0.1068*	0.0904*
	−0.0461	−0.0586	−0.0577	−0.0704	−0.063
did * minor	0.0883*				
	−0.0951				
Structure	0.1107		0.1793*		−0.0068
	−0.0674		−0.0956		−0.1221
lnpergdp	0.1518		0.2704*		0.0234
	−0.1003		−0.15		−0.1101
RD	−0.0001*		0		−0.0002*
	0		−0.0001		−0.0001
Wage	−0.0147**		−0.0162		−0.0108
	−0.0061		−0.0099		−0.0186
Urban-rate	0.0569		−0.376		0.5904
	−0.2869		−0.4646		−0.4866
Trade-rate	−0.0442		0.0393		−0.3076
	−0.0864		−0.1008		−0.2237
Gov-invest	−0.053		0.0521		−0.1498
	−0.0752		−0.0841		−0.1306
lnarea	−0.0131		−0.0383		0.0251
	−0.0291		−0.0401		−0.0528
_cons	1.2256***	0.9264***	1.5644***	1.0863***	0.7535
	−0.3605	−0.0463	−0.5066	−0.0547	−0.651
R^2	0.221	0.2009	0.2321	0.2404	0.2647
N	651	315	315	336	336

confidence level of human capital investment is significant at 5%, and the confidence level of industrial structure, science and technology, and economic development is significant at 10%. The results show that the degree of human capital investment is the most significant among the control variables, which is mainly due to the significant improvement of per capital production efficiency with the improvement of scientific and technological development levels and the increase of capital investment in natural forest protection projects, which directly promotes the improvement of the whole forestry production factors. On the other hand, the improvement of the level of economic development in forest areas has led to a rise in wage income and the increase in per capita labor cost, which has also prompted relevant enterprises and business entities to improve their management level and realize staff reduction and efficiency. At the same time, the improvement of industrial structure, science and technology, and economic development level offset the impact of the prohibition of commercial logging on the income of forestry enterprises to a certain extent, opened up new financial resources, and provided financial support, material basis and scientific and technological guarantee for improving forestry TFP. Compared with human capital, industrial structure, scientific and technological development level, and economic development level, the level of urbanization, the degree of opening to the outside world, government intervention, and natural disasters have no significant impact on the total factor production efficiency of forestry. From the viewpoint of the characteristics of regional economic structure, the implementation of natural forest protection projects has been accelerated, and the proportion of tertiary industry has increased. However, due to the limitations of forest climate, land, and other resources and the regulation of relevant laws and regulations such as the forest law, the proportion of primary industry has not been high in history, and the proportion of the agricultural population is relatively low. The execution of the NFPP has brought about a very limited space for the transformation of the agricultural population into the urban population, which is not enough to constitute a significant impact. Similarly, since the reform and development, China's imports of forest products such as timber have increased year by year, but the cross-border flow of production factors such as forestry-related funds, labor, and science and technology is not significant. The change of opening-up degree is mainly affected by the endogenous economic growth and external trade environment of forest areas and is not highly related to the TFP of forestry. Most of the areas where the natural forest protection project is implemented are state-owned forest areas, and the degree of government intervention has been relatively high, and the policy implementation has not significantly improved the level of government intervention. The execution of NFPP increases the government's investment in forest development, but a considerable proportion of the funds is used for consumption and guarantee expenditure, which is not significantly affected by the improvement of the forestry management level.

3.2. Grouping Verification Results and Differential Analysis. For the sake of further studying the efficiency of resource allocation and the action mechanism of influencing factors in the execution of NFPP, the variables are grouped again in this article. First, 31 provinces in China are ranked according

to the average annual forest coverage from 1997 to 2018, and then the top 15 provincial regions with forest coverage and natural forest protection projects, namely, Hainan, Yunnan, Heilongjiang, Jilin, Shaanxi, Hubei, Sichuan, and Chongqing, are divided into the experimental group. The average forest coverage rate in the past few years did not rank among the top 15 in China, and the provincial areas implementing the natural forest protection project, namely, Guizhou, Inner Mongolia, Henan, Shanxi, Tibet, Ningxia, Qinghai, Xinjiang, and Gansu, were used as the control group. The heterogeneity analysis was carried out for the top 15 provincial areas with forest coverage, i.e., the experimental group (see Table 4). The regression results show that the high forest resource coverage and natural forest protection project have a useful impact on the TFP of forestry in this area, and the impact of policy implementation is more significant.

$$\text{tfpch}_{it} = \beta_0 + \beta_1 \text{did}_{it} + \beta_2 \text{did}_{it} * \text{minor}_i + \beta_3 \text{minor}_t \\ + \beta_4 \text{control}_{it} + \eta_i + \gamma_t + \varepsilon_{it}. \tag{4}$$

In the formula, minor_i is a dummy variable. If i province ranks among the top 15 forest resources, $\text{minor}_i = 1 \text{minor}_i = 1$; otherwise, it is 0.

Forest coverage rate is an important reference index to reflect the richness of forest resources. The impact of NFPP on forestry TFP is significantly positively correlated with forest coverage rate, indicating that after the implementation of the policy, the forest volume, area, and coverage rate in the area are significantly improved, and the forest structure tends to be more reasonable and the forest quality is significantly improved. At the same time, the NFPP has invested huge funds to significantly strengthen the implementation of policies and the construction of provincial forest ecosystems, wetland ecosystems, desert ecosystems, and biodiversity protection and promoted the coordinated development of forest resources and forestry industry in the region.

4. Conclusions and Policy Implications

4.1. Conclusion. Taking the Malmquist index of forestry TFP in 31 provinces in China as the explanatory variable, based on dimensions of policy management and the environment of the execution of NFPP, this article regards the execution of NFPP as a policy impact and calculates and analyzes the provinces with and without policy execution through DID model. The results show that the execution of NFPP has a significant impact on forestry TFP as a whole. The reduction of human investment, the rationalization of industrial structure, the improvement of science and technology investment, and the level of economic development can effectively improve the allocation efficiency of factor resources among forestry production, while the improvements of urbanization level and opening-up, government intervention, and natural disasters have no significant impact on the efficiency of forestry total factor production. Similarly, in areas with high forest coverage, the impact of NFPP on the improvement of forestry total factor productivity is more significant.

4.2. Policy Implications

(1) Establish scientific natural forest protection and restoration system to protect natural forests in an all-around way. The government should increase the support for infrastructure construction in large forest areas. The construction of infrastructures such as power grid and drinking water safety and the housing of management and protection stations will be included in the construction planning and overall arrangement of the superior government, and the roads in state-owned forest areas will be included in the relevant highway network planning according to their attributes. Forestry management departments should actively fill the gap of forest tending funds, appropriately raise the standard of forest tending subsidies, gradually improve the quality of forest resources, and speed up the transformation of low-quality forest resources by expanding the scale and scope of forest tending subsidies.

(2) Actively cultivate and expand the forestry scientific research team and accelerate the transformation of forestry scientific and technological achievements. Build and cultivate a professional forestry technology application and promotion team, apply modern information technology and media channels, do a good job in business training and information exchange, and help grass-roots technicians master a variety of technologies and equipment. Scientifically formulate talent training plans, innovate talent use mechanisms, continue to carry out professional and technical training, and cultivate a group of high-quality forestry engineering managers, high-level scientific researchers, high-level technicians, and high skilled industrial workers, so as to ensure the universal application of forestry digital platform, the continuous improvement of scientific and technological innovation drive, constantly make the team of engineering managers better, and strengthen the talent guarantee for forestry development.

(3) The government should attach great importance to the ecological protection of forest resources and improve the regional forest coverage. First, comprehensively summarize the implementation experience of natural forest protection projects, appropriately expand the scope of project implementation, strengthen management, protection, and law enforcement, and take effective measures to protect natural forests. Second, strengthen the management of artificial forest closure, improve the canopy density of forest land, improve biodiversity, and strengthen the transformation of degraded forest stands. Third, strictly manage forest resources according to laws and regulations, bring the forest land managed by nonforestry departments into the statistical management of forest resources, and strengthen the supervision of forest land to ensure that the area of forest land only increases but not decreases. Focus on encouraging the development of forestry ecological products. Protect forestry ecological

diversity, carry out the overall development of "land-scape, forest, field, lake, and grass," enrich the supply form of forest ecological products, and improve the development and utilization efficiency of forest ecological products.

Data Availability

The data used to support the findings of this study are included within the article.

Conflicts of Interest

The authors declare that there are no conflicts of interest regarding the publication of this article.

Acknowledgments

References

[1] J. Wang, X. Wang, and J. Wan, *Environmental Strategy and Planning in China*, Springer Science and Business Media LLC, Berlin, Germany, 2022.

[2] X. Wang, "China's forest coverage 22.96%," *Green China*, no. 12, pp. 54–57, 2019.

[3] M. Wang, "Significance of wood inspection to "natural conservation project"," *Rural practical science and technology information*, no. 5, p. 33, 2013.

[4] G. Geng, "Natural Conservation Project: investment of 400 billion yuan in exchange for 275 million mu of public welfare forest," *Green China*, no. 8, pp. 31–34, 2019.

[5] L. Chen, Y. Cao, Z. Zhu, and L. Su, "Knowledge map analysis of natural forest protection engineering research in China," *Journal of Agriculture and Forestry Economics and Management*, vol. 14, no. 6, pp. 622–629, 2015.

[6] Y. Cao, X. Huang, and Z. Zhu, "Review on benefit evaluation of natural forest resources protection projects in China," *Ecological Economy*, vol. 34, no. 1, pp. 107–111, 2018.

[7] L. Qin and M. Zhang, "Empirical analysis on the implementation performance of phase II policy of natural gas protection project," *Forestry Economic Issues*, vol. 41, no. 5, pp. 455–463, 2021.

[8] F. Cui, L. Zhi, and Y. Xie, "Value evaluation of forest ecosystem service function of natural conservation project in Jingbian, Shaanxi," *Journal of Southwest Forestry University*, vol. 37, no. 4, pp. 58–66, 2017.

[9] L. Zang, "An empirical analysis of the impact of the western natural protection project on Farmers' income," *Journal of Agriculture and Forestry Economics and Management*, vol. 13, no. 2, pp. 201–209, 2014.

[10] X. Zhai, H. Wang, and H. Lin, "Study on the impact of natural conservation project on the change of forestry industrial structure in state-owned forest areas," *Forestry Economic Issues*, vol. 40, no. 6, pp. 609–617, 2020.

[11] Y. Wu, L. Chen, and B. Zhou, "Has the overall urban-rural reform improved the efficiency of total factor allocation in Chengdu and Chongqing—— double difference model based on DEA and did," *Resource Development and Market*, vol. 35, no. 6, pp. 769–775, 2019.

Research Article

Lecture Video Automatic Summarization System Based on DBNet and Kalman Filtering

Fan Sun [1,2,3] **and Xuedong Tian** [1,2,3]

¹School of Cyber Security and Computer, Hebei University, Baoding 071002, China
²Hebei Machine Vision Engineering Research Center, Hebei University, Baoding 071002, China
³Institute of Intelligent Image and Document Information Processing, Hebei University, Baoding 071002, China

Correspondence should be addressed to Xuedong Tian; xuedong_tian@126.com

Video summarization for educational scenarios aims to extract and locate the most meaningful frames from the original video based on the main contents of the lecture video. Aiming at the defect of existing computer vision-based lecture video summarization methods that tend to target specific scenes, a summarization method based on content detection and tracking is proposed. Firstly, DBNet is introduced to detect the contents such as text and mathematical formulas in the static frames of these videos, which is combined with the convolutional block attention module (CBAM) to improve the detection precision. Then, frame-by-frame data association of content instances is performed using Kalman filtering, the Hungarian algorithm, and appearance feature vectors to build a tracker. Finally, video segmentation and key frame location extraction are performed according to the content instance lifelines and content deletion events constructed by the tracker, and the extracted key frame groups are used as the final video summary result. Experimenting on a variety of scenarios of lecture video, the average precision of content detection is 89.1%; the average recall of summary results is 92.1%.

1. Introduction

The rapid development of computer technology and online education means video has become an important resource for students and educators. The impact of the spread of COVID-19 on traditional educational methods also makes online video education play an increasingly important role. In a large number of lecture videos, contents such as texts and mathematical expressions can often summarize and locate the videos. Automatically extracting and summarizing these contents can effectively utilize educational video resources and enable users to quickly browse the contents. The online education system can also conduct effective content management of video assets through the technology of lecture video summarization to achieve functions such as indexing, browsing, retrieval, and promotion. Based on these needs, the research on lecture video content summarization technology is extremely valuable.

For general video summarization, there are many methods that use a set of automatically extracted key frames to represent the main content of the video [1, 2]. These methods seek to find important scenes, objects, colors, and moving objects in videos and usually follow three steps, namely, video feature extraction, frame image clustering [3, 4] or classification, and key frame selection. However, these methods do not scale well to lecture videos. A semantically meaningful change, such as text popping up in a slideshow, usually results in a rather subtle appearance change in the video and is thus ignored by these methods. On the other hand, the lecturer's position movement can cause significant appearance changes, triggering extraneous key frames.

In these videos, lecturers usually use projection to demonstrate the learning content or use blackboard, whiteboard, paper, or electronic device screen for handwritten interpretation. Content extraction faces challenges such as complex backgrounds and occlusion. Also,

mathematical formulas have complex two-dimensional structures, and courses with a lot of math content are more inclined toward handwritten demonstrations. Therefore, the methods of automatic speech recognition technology are not fully applicable.

Traditional lecture video summarizations generally design algorithms based on teaching scene features. For academic videos based on slide presentations, Li et al. [5] proposed a fully automated system to extract the semantic structure of academic slide presentation videos, the system automatically locates and tracks the projection screen, tracks the sparse optical flow feature points in the screen region, detects the slide progression by analyzing the feature point trajectories, constructs a frame index with a large number of feature appearances or disappearances, and extracts for each slide a high quality, nonoccluded, geometrically compensated images to generate a representative set of image lists that reconstruct the main presentation structure of the slide, and experimental results show that for this specific type of video, the system is able to extract a more accurate representation structure than general video summarization methods. Davila and Zanibbi [6] first locate the whiteboard region, use the lag image between Otsu's binarization and random forest binarizer to generate binary images of whiteboard handwriting, generate spatio-temporal indices for handwriting, and detect and eliminate content. Conflicts between regions are time-segmented to extract key frames, and tests on the AccessMath dataset show that the summary method has a good compression ratio. Rahman et al. [7] proposed a new visual summarization method for lecture videos by dividing the video into multiple segments based on the inter-frame similarity of the content and defining the most representative images by estimating the importance of each image in the segment, calculating the distance matrix between images, and using a graph-based algorithm; the proposed algorithm is significantly better than random selection and cluster-based selection, and only slightly lower than manual selection.

With the development of computer vision and deep learning, much research is based on neural networks. Dutta et al. [8] investigated the effectiveness of state-of-the-art scene text detection networks for text detection in lecture video scenes and built LectureVideoDB, a static frame dataset of English lecture videos for this purpose; experimental results show that existing methods perform poorly on this dataset and need to be improved for application in educational scenes; in this work, the EAST scene text detection model [9] was used as a baseline to develop a system for detecting and recognizing instructional video text, but mathematical expressions and sketches as important elements were not annotated and evaluated. Since the lecturers will perform various actions with semantic information, such as writing and erasing, during the teaching process, Xu et al. [10] proposed a method based on speaker action classification, using the OpenPose pose estimator [11] to extract body and hand skeletal data to calculate action features and then using random forests and motion features to classify speaker actions, segmented the video based on

handwritten content erasing actions to extract key frames from lecture videos of handwritten whiteboard content as video summary, and the summary results with good compression. Davila et al. [12] proposed an FCN-LectureNet model based on a fully convolutional neural network (FCN) to extract English handwritten content from videos as binary images, further generate a time-space index of handwritten content, and create key frame-based handwritten content summaries based on the time periods that change when a large amount of content is deleted, and validation results showed that this method outperforms some existing handwritten lecture video summarization methods.

To sum up the above, most of the lecture video summarization methods based on visual content extraction are aimed at some specific scenes, such as slide teaching scenes and whiteboard handwriting teaching, and are mainly in English, which has a certain impact on the robustness and generalization performance of the system. To address the above difficulties, this paper improves the deep learning-based text detection algorithm and expands the Chinese teaching video dataset to detect text and mathematical formulas in a variety of teaching scenarios. Use the Kalman filtering and Hungarian algorithm to track content instances, construct content instance lifelines to segment lecture video based on the tracking result, and complete the positioning and summary of lecture video key frames. The main contributions of this paper are as follows:

(1) Combining DBNet [13], a scene text detection network with differentiable binarization method, with convolutional block attention module (CBAM) [14], which has spatial and channel attention mechanisms, adapts DBNet to the detection of text, mathematical formulas, and sketches in static frames of instructional videos to improve detection precision.

(2) A multi-target tracking method based on Kalman filtering and the Hungarian algorithm is introduced for content instance tracking, and adding content instance appearance vector matching before geometric position matching improves the tracking method and reduces the false tracking caused by simple geometric position matching.

(3) Lecture videos of advanced education lectures taught in Chinese in various scenarios are collected to build the dataset. On the video still frames, content such as text is annotated for content detection training; key frames are manually selected for comparison with the automatically extracted key frames.

The rest of the paper is structured as follows: the second part elaborates the lecture video summarization method of this paper; the third part analyzes and discusses the experimental results; the fourth part summarizes the paper.

2. Materials and Methods

The overall flowchart of the proposed lecture video summarization method is shown in Figure 1.
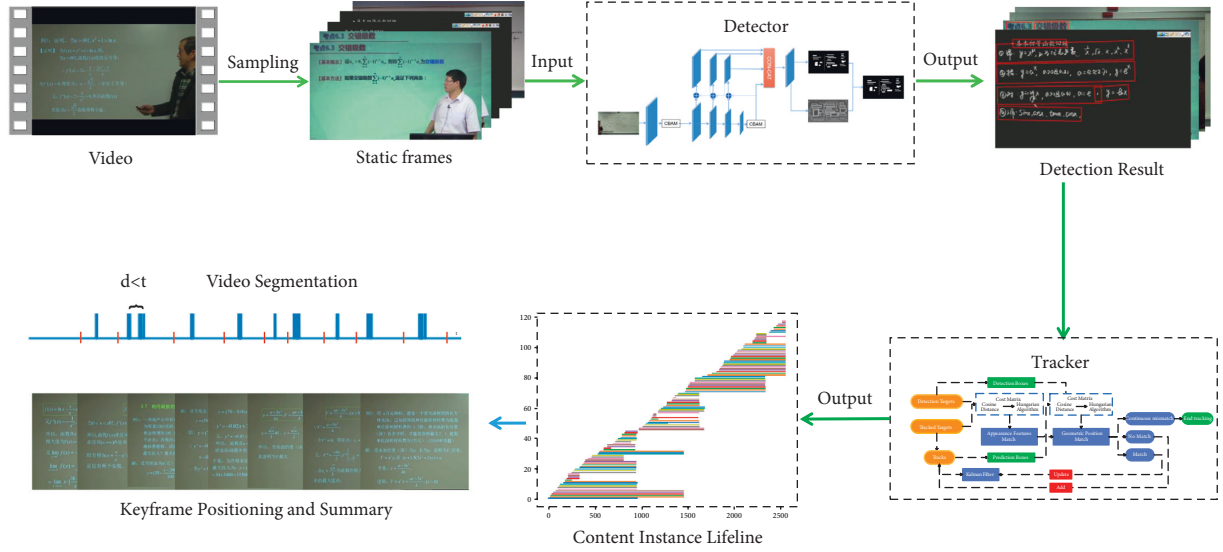
FIGURE 1: The flow of the method proposed in this paper.

2.1. CBAM-DBNet Content Detector.

The real-time text detection network DBNet with a differentiable binarization method is used as a lecture video content detector to detect the text and mathematical formulas in the lecture video. The DBNet backbone network adopts ResNet [15] and uses deformable convolution [16] in the conv3-conv5 layers for feature extraction. Deformable convolution can adaptively obtain the morphological features and scale information of the target. Deformable convolution can adaptively obtain morphological features and scale information of the target, which facilitates the detection of contents with extreme aspect ratios in still frames of lecture videos. The feature pyramid networks (FPNs) [17] are used to upsample the conv2-conv5 layers and perform feature fusion to deal with the multi-scale variation in detection; in the output part of the network, the approximate binarization map is calculated using the probability map P and the adaptive threshold map T predicted during the training process, and the detection bounding box is inferred from the approximate binarization map.

Due to the existence of complex background, image noise, and occlusion in teaching scenes, in order to increase the differentiation between content and noncontent regions, this paper adds the convolutional block attention module (CBAM) after the cov1 and cov5 layers of the backbone network of DBNet to construct the CBAM-DBNet content detector for spatial and channel attention to make the network pay more attention to target objects such as text and mathematical formulas in feature extraction of static frame images. CBAM is added to the first and last convolutional layers of ResNet in order to be able to use pretraining parameters without changing the network structure. The structure of the CBAM-DBNet detection network is shown in Figure 2.

The differentiable binarization method of DBNet and the convolutional block attention module (CABM) are introduced as follows.

2.1.1. Differentiable Binarization (DB).

In the DBNet algorithm, the binarization operation is inserted into the segmentation network for joint optimization in order to adaptively predict the threshold value at each position of the image in order to better distinguish the foreground and background regions. However, the traditional standard binarization function is not differentiable; a differentiable approximate binarization function, called differentiable binarization, is given in DBNet so that the binarization operation can be trained together with the segmentation network. The standard binarization and differentiable binarization are shown in

$$B_{i,j} = \begin{cases} 1, & P_{i,j} > = t, \\ 0, & \text{otherwise,} \end{cases} \tag{1}$$

$$\widehat{B}_{i,j} = \frac{1}{1 + e^{-k\left(P_{i,j} - T_{i,j}\right)}}. \tag{2}$$

2.1.2. Convolutional Block Attention Module.

The convolutional block attention module (CBAM) is a lightweight, general-purpose feedforward convolutional neural network attention module that contains the spatial attention module (SAM) and the channel attention module (CAM). The structure of CBAM is shown in Figure 3.

Given the feature map $F \in \mathbb{R}^{C \times H \times W}$ as input, CBAM inferred the 1D channel attention map $P_{ca} \in \mathbb{R}^{C \times 1 \times 1}$ and 2D spatial attention map $P_{sa} \in \mathbb{R}^{1 \times H \times W}$ in turn, and the overall attention process is shown in

$$F' = P_{ca}(F) \otimes F, \tag{3}$$

$$F'' = P_{sa}(F') \otimes F'. \tag{4}$$

The channel attention module, in order to calculate the importance of different feature channels more efficiently, compresses the input feature map F through the average pooling layer and the maximum pooling layer, respectively, and turns the feature map of size $C \times H \times W$ into two feature
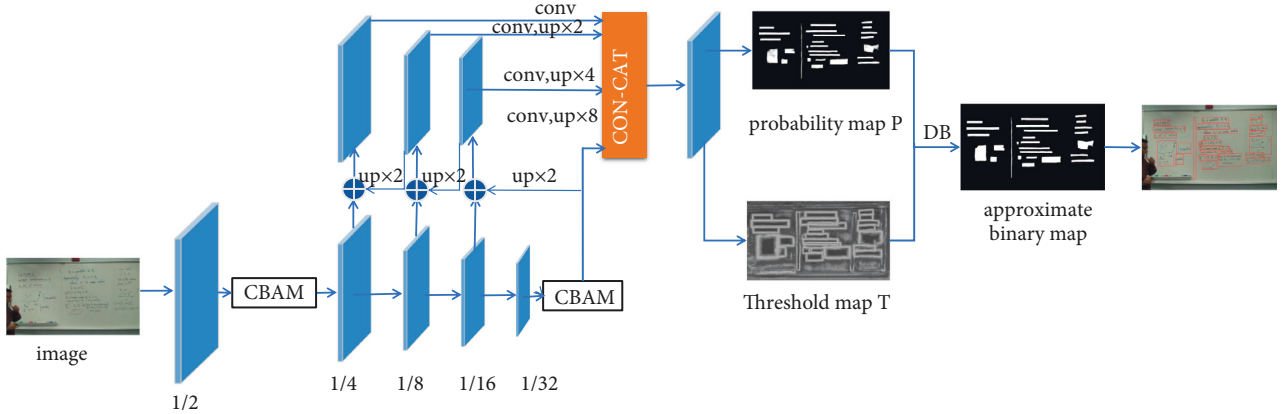
FIGURE 2: The structure of the improved content detection network.
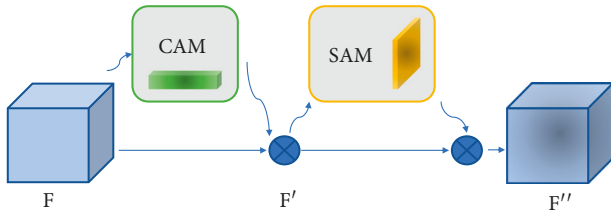
FIGURE 3: Convolutional block attention module structure.

maps of size $C \times 1 \times 1$. The compressed two feature maps are convolved by a shared multilayer perceptron (MLP) operation, and the output results are summed at the element level and activated by the sigmoid activation function to obtain the feature map $P_{ca}(F) \in \mathbb{R}^{C \times 1 \times 1}$ with channel attention weights. $P_{ca}(F)$ and the original feature map F are multiplied by channel to obtain the new feature map F' with channel attention weighting. To calculate spatial attention, the feature map F is first passed through maximum pooling operation and average pooling operation, respectively, to form two feature vectors of size $1 \times H \times W$, and the two features are connected together to form a feature map of size $2 \times H \times W$. Then, through a convolutional layer, the feature map dimension changes from $2 \times H \times W$ to $1 \times H \times W$. The $1 \times H \times W$ feature map characterizes the importance of each point on the feature map and is activated using the sigmoid function to generate a feature map $P_{sa} \in \mathbb{R}^{1 \times H \times W}$ with spatial attention weights. Then, P_{sa} is multiplied with F' to obtain the feature map F'' with channel attention and spatial attention weighting as the output of the CBAM.

2.2. Tracker for Content Instances. Introducing Kalman filtering and the Hungarian algorithm to deal with position prediction and inter-frame data association in content instance tracking, respectively, Kalman filtering and the Hungarian algorithm have played a significant role in the field of multi-target tracking [18–20]. In this paper, the appearance feature matching module is added to the Kalman filtering and Hungarian algorithm-based multi-target tracking algorithm [18] to integrate appearance features and geometric location features for content instance tracking

and reduce the false tracking caused by simple geometric location matching. The tracking process is shown in Figure 4.

The specific steps of content instance tracking are described as follows:

(1) The initial frame detection result is used as the tracked target of the tracker, and the Kalman filter is initialized. Kalman filtering propagates the tracked content instance target state to the subsequent frames, correlates the detection result of the current frame with the tracked target, and manages the tracked target. The state of the target is modeled as shown in

$$M = [h, v, a, r, \dot{h}, \dot{v}, \dot{a}, \dot{r}]^T, \tag{5}$$

h and v represent the pixel position of the center of the target bounding box; a and r represent the pixel size and aspect ratio of the target bounding box, respectively; $(\dot{h}, \dot{v}, \dot{a}, \dot{r})$ corresponds to the motion speed of the (h, v, a, r) components between the front and rear frames.

(2) After embedding the content instance representation information extracted by ResNet18 into a vector δ, the cosine distance is used to calculate the similarity between the representation vector stored in the track and the detection result representation vector of the current frame. The cosine distance measurement formula based on appearance features is shown in

$$d_{cha}(i, j) = 1 - \delta_j^T \delta_i, \tag{6}$$

i and j represent the i-th trajectory stored in the tracker and the j-th result detected by the detector, respectively. The cost matrix of the Hungarian algorithm is constructed with $d_{cha}(i, j)$ for appearance feature matching of content instances. The Hungarian algorithm is a data association algorithm that seeks the maximum match. It obtains the maximum matching pair within the matching threshold according to the cost matrix and the principle of minimum cost. The smaller the $d_{cha}(i, j)$ is, the more
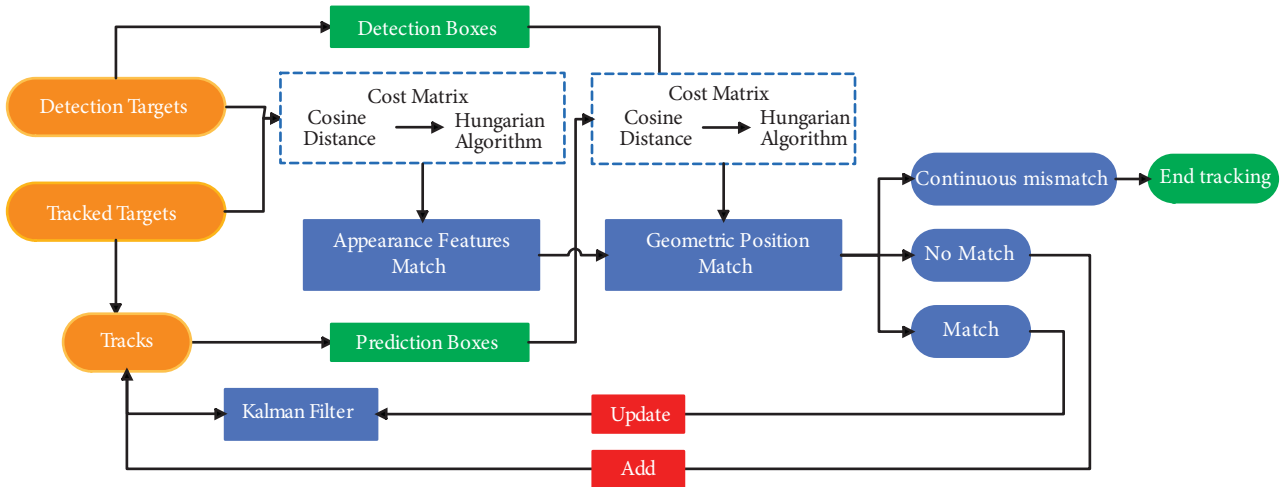
FIGURE 4: The flow of content instance tracking.

similar the two appear, and the more likely they are the same tracking target.

(3) The Kalman filtering uses the (h, v, a, r) of the tracking target as a variable to predict the target state of the current frame and uses the IOU (intersection and union ratio) between the predicted $bbox_{pre}$ set and the detector's detection result $bbox_{det}$ set to calculate the geometric similarity. Based on IOU, the geometrical position distance measurement formula is shown in

$$d_{\mathrm{geo}}(i, j) = 1 - \frac{\mathrm{area}\big(bbox_i \cap bbox_j\big)}{\mathrm{area}\big(bbox_i \cup bbox_j\big)}, \qquad (7)$$

$d_{\mathrm{geo}}(i, j)$ is used to construct the cost matrix of the Hungarian algorithm for geometric position matching of content instances.

(4) If the geometric position matching result is consistent with the appearance feature matching result, the matching is successful, and the status of the trajectory is updated. If the tracking target fails to match continuously on subsequent frames for more than Fmax frames, the tracking of the track is ended.

2.3. Video Segmentation and Summaries. According to the content instance tracking results, the trajectories of all tracked targets on the time axis in a complete teaching video are obtained, including interference such as character occlusion, as shown in Figures 5(a) and 5(b). The lifeline of the content instance on the video timeline is constructed based on the start and end times of the target trajectory, as shown in Figures 5(c) and 5(d).

In order to extract a static summary of an instructional video, that is, a set of key frames that best summarize the video content, it is first necessary to divide the video into time segments with semantic information. The semantic time segments of instructional videos are usually updated to a set of handwritten or projected instructional content. To start, end with the group of instructional content disappearing from the video. In this paper, inspired by Xu et al. based on identifying speaker action erasure events and the FCN-LectureNet method based on main content deletion events for video time segmentation, the end of the content instance lifeline is used as the signal, and the cumulative deletion events on the video timeline are the basis for video segmentation. On the video timeline, the visualization of the normalized content added, deleted, and total area size is shown in Figure 6.

After the video is divided into several time sub-segments, the static frames containing all the track objects of the current segment are extracted as key frames in each segment interval, as shown in Figure 7. A set of key frames extracted from a complete instructional video is used as the summary of the video.

3. Results and Discussion

3.1. Introduction to the Dataset. The dataset contains 5 Chinese online advanced mathematics lecture videos collected on the Internet, including a variety of scenes and content forms (projected and handwritten), some static frames of the 4 videos are marked with content instances such as text and mathematical formulas, and manual key frame selection is performed for each video. To complement the variety of lecture video scenarios, three English whiteboard handwritten lecture videos from the publicly available dataset AccessMath [21] were selected. The information for each video is shown in Table 1.

In the training phase of the detection network, 4648 images were randomly selected as the training set and 1510 images were used as the test set; during preprocessing, data enhancement was performed by randomly cropping the image size to 640×640 and randomly rotating ($-10°$, $10°$).

3.2. Content Detection Evaluation Index and Experimental Results. Using recall, precision, and F1-score as evaluation metrics for content detection network, the evaluation method uses the scene text detection evaluation method DetEval [22], which considers three types of rectangular box
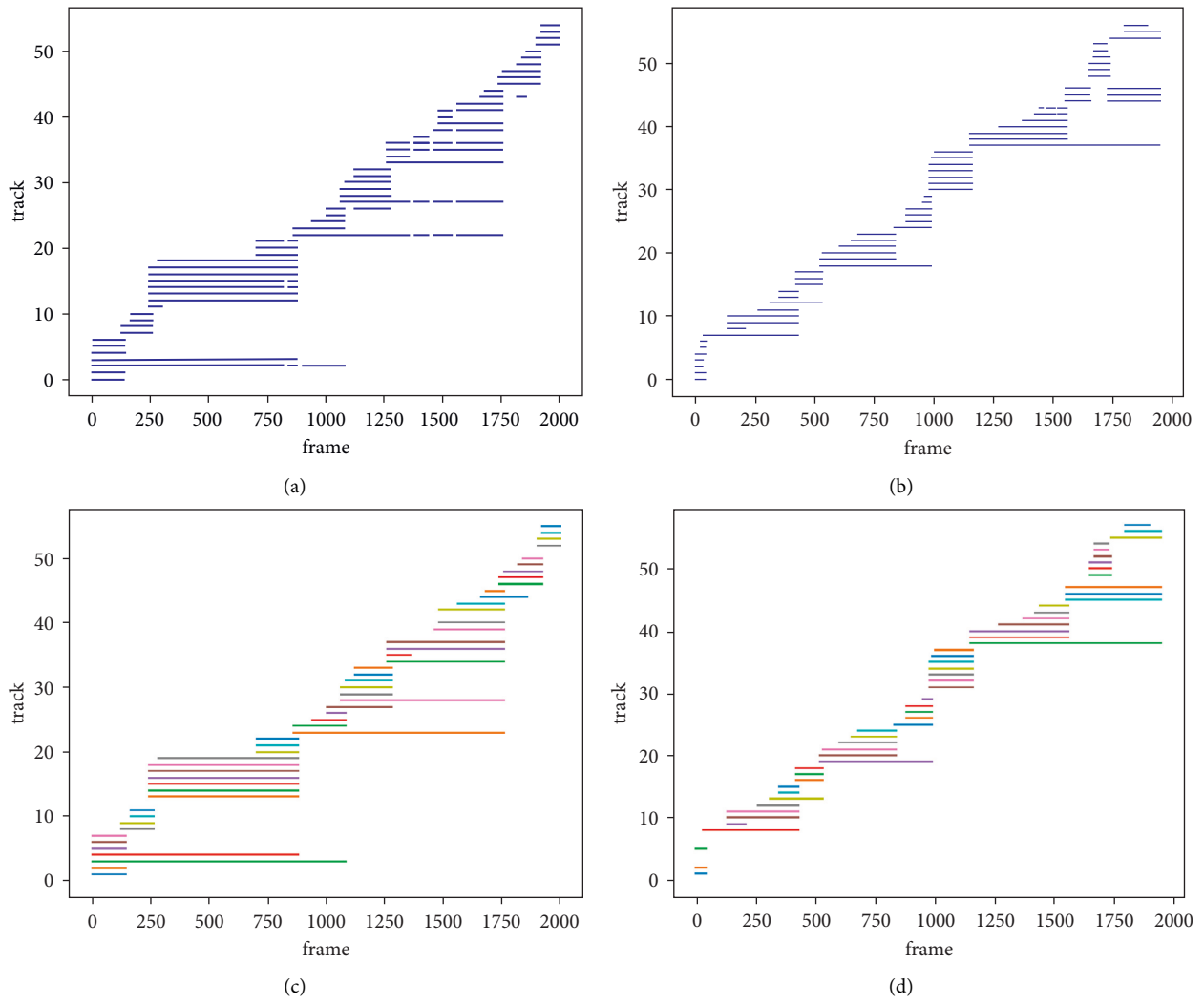
FIGURE 5: An example of tracking track and lifeline of content instance on a complete video timeline: (a and b) tracking trajectory; (c and d) lifeline.
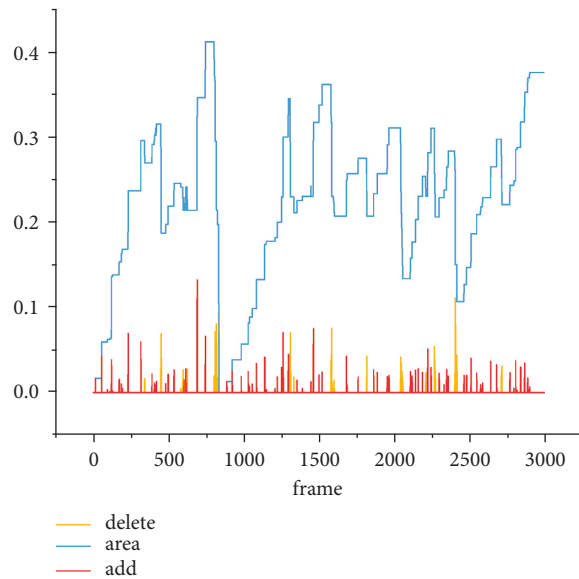
FIGURE 6: Normalized content addition and deletion events, as well as the size of the content area per frame.

FIGURE 7: Video segmentation and key frame extraction.

TABLE 1: The information of the lecture videos.

Video number	Video duration	The number of speakers	Scene	The number of key frames
CLV01	8 m17 s	1	Whiteboard projection	3
CLV02	25 m22 s	0	Blackboard handwriting	4
CLV03	32 m37 s	1	Blackboard projection	8
CLV04	33 m11 s	1	Blackboard projection	8
CLV05	35 m28 s	1	Whiteboard projection	9
AM_01	44 m25 s	1	Whiteboard handwriting	7
AM_06	47 m20 s	1	Whiteboard handwriting	11
AM_NM_03	41 m27 s	1	Whiteboard handwriting	13

matching, i.e., one-to-one, many-to-one, and one-to-many, and uses the matrix to store the matching situation between the annotation data G and the detection result D. As shown in equation (8), the two matrices of recall and precision are denoted by σ and τ, respectively. σ, τ are matrices of $|G| \times |D|$. The probability map, adaptive threshold map, and detected bounding boxes of static frame content detection are shown in Figure 8.

$$\sigma_{ij} = R(G_i, D_j),$$
$$\tau_{ij} = P(G_i, D_j), \quad (8)$$

$t_r, t_p \in [0, 1]$ are the matching judging thresholds of σ and τ, respectively, and Match() is the matching function of G and D. The rules of recall and precision calculation for a single image are shown in equation (9).

$$R_{OB}(G, D, t_r, t_p) = \frac{\sum_i \text{Match}_G(G_i, D, t_r, t_p)}{|G|},$$

$$P_{OB}(G, D, t_r, t_p) = \frac{\sum_j \text{Match}_D(D_i, G, t_r, t_p)}{|D|}. \quad (9)$$

The final recall and precision are calculated in a similar way as mAP, as shown in equations (10) and (11). The combined evaluation index F1-score is the summed average of both, as shown in equation (12).

$$\text{Recall} = \frac{1}{2T} \sum_{i=1}^{T} R_{OB}(\overline{G}, \overline{D}, i/T, t_p)$$
$$+ \frac{1}{2T} \sum_{i=1}^{T} R_{OB}(\overline{G}, \overline{D}, t_r, \frac{i}{T}), \quad (10)$$

$$\text{Precision} = \frac{1}{2T} \sum_{i=1}^{T} P_{OB}(\overline{G}, \overline{D}, \frac{i}{T}, t_p)$$
$$+ \frac{1}{2T} \sum_{i=1}^{T} P_{OB}(\overline{G}, \overline{D}, t_r, \frac{i}{T}), \quad (11)$$

$$F1 - \text{score} = 2 \frac{\text{Recall} \cdot \text{Precision}}{\text{Recall} + \text{Precision}}. \quad (12)$$

For content detection of static frames of lecture videos, the detection performance is improved when both deformable convolution and CBAM attention modules are added to the backbone network ResNet50. The precision is improved by 2.4%, the recall is improved by 4.5%, the overall index is improved by 3.5%, and the results of the ablation experiments are shown in Figure 9.

In Table 2, the content detection experiments of this paper's model are compared with the advanced text detection models PixelLink [23] and TextSnake [24], and better results are obtained by this paper's method.

3.3. Video Summary Evaluation Indexes and Experimental Results.
The predicted key frames are compared with the annotated data; i.e., the summary results are matched with elements occupying the same space in approximately the same time period as the annotated data. Recall, precision, and F1-score are calculated as follows:

$$\text{Recall} = \frac{\text{TP}}{\text{TP} + \text{FN}},$$

$$\text{Precision} = \frac{\text{TP}}{\text{TP} + \text{FP}}, \quad (13)$$

$$F1 - \text{score} = 2 \frac{\text{Recall} \cdot \text{Precision}}{\text{Recall} + \text{Precision}},$$

where true-positive instances (TP) represent correctly predicted summary contents, and false-positive instances (FP) and false-negative instances (FN) represent incorrectly predicted (includes repeated predictions) and missing predicted contents, respectively.
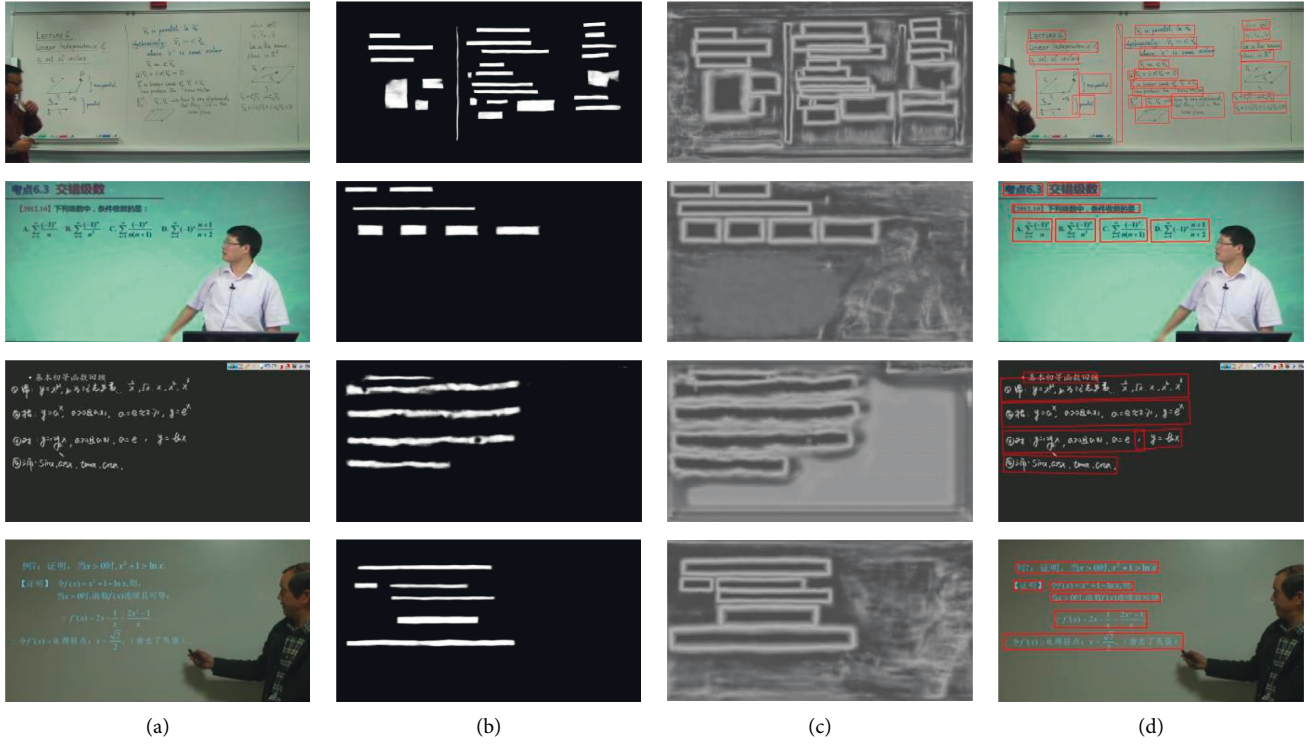
FIGURE 8: Visualization of content detection: (a) video static frames; (b) probability map; (c) adaptive threshold map; (d) detected bounding box results.
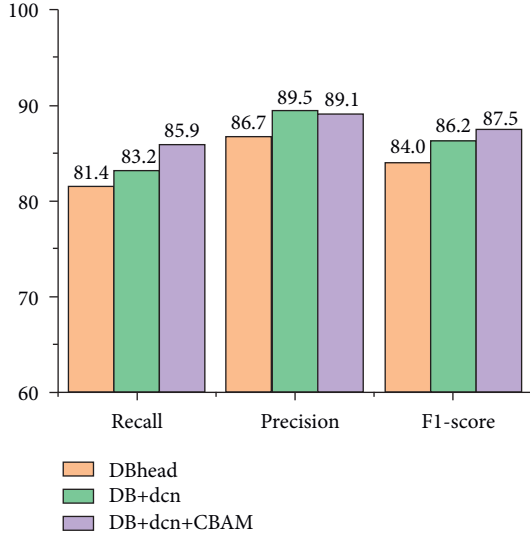
FIGURE 9: Results of ablation experiments.

TABLE 2: Comparison of different text detection models.

Models	Recall	Precision	F1-score
PixelLink	74.8	84.2	79.2
TextSnake	76.9	86.7	81.5
CBAM-DBNet	85.9	89.1	87.5

In addition, the standard deviation (SD, $\sqrt{\sum_{i=1}^{n}(K_p - K_m)^2/n}$) between the predicted key frame

TABLE 3: Performance of summary results on lecture videos.

Video number	The number of key frames	Recall	Precision	F1-score
CLV01	3	100	100	100
CLV02	5	84.2	72.7	78.1
CLV03	9	100	94.1	97.0
CLV04	9	87.0	87.0	87.0
CLV05	7	89.3	100	94.3
AM01	7	92.6	100	96.2
AM06	10	97.9	89.2	93.0
AM_NM_03	10	89.8	89.8	89.8
Average	1.46 (SD)	92.1	90.8	91.3

number K_p and the manually marked key frame number K_m is calculated to represent the compression ratio of the summary results.

As shown in Table 3, the summary results of the method in this paper on lecture videos in various scenarios have achieved good results. The average values of precision and recall were 90.8% and 92.1%, respectively; the average composite evaluation index F1-score was 91.3%.

Among the obtained summarization experimental results, the average recall, precision, and F1-score of handwritten presentation video summarization results are 91.1%, 87.9%, and 89.3%, respectively, while the average recall, precision, and F1-score of projected presentation video summarization results are 94.1%, 95.3%, and 94.6%, respectively. The average summary performance of the method in this paper for lecture videos with handwritten presentation is lower than that of instructional videos using

projected presentation, due to the fact that handwritten content instances in lecture videos with handwritten presentation are usually irregular and the content instance detector cannot segment these tightly connected text or scribbled mathematical formulas as precisely as ground truth annotations and projected content.

Since neither the geometric position nor the appearance feature vector can distinguish the content instance with slight changes, such as the change of individual numbers in a mathematical formula, the method in this paper cannot regard the content instance with slight changes as a new content instance, which will reduce the recall rate of summary results. The method based on speaker action classification may be able to better capture these details through the speaker's action, but it is only applicable to the video of the speaker's handwriting demonstration in the whole process.

4. Conclusions

Aiming at the fact that the current detection and summarization methods based on the main visual content of educational lecture videos are often based on specific scenarios, a lecture video summarization system based on improved DBNet text detection network, Kalman filtering, and the Hungarian algorithm is proposed. The detection and summarization cover Chinese and English, handwriting, screen projection, and black and whiteboard scenes, and the summary results achieve good recall.

However, there are some shortcomings in the methodology of this paper, which will be improved in the future by the following points:

(i) Improvements will be made to the detection network to unify detection and tracking in one framework, make better use of the timing information of the video, improve detection system performance, and experiment with lightweight network structures.

(ii) Collect and label more data for more comprehensive training and analysis to further improve the robustness of the system.

(iii) The extraction and representation of the appearance features of content instances will be improved so that the improved representation can better distinguish content instances with subtle changes and improve the recall of summaries.

Data Availability

The data that support the findings of this study can be obtained from the corresponding author upon request.

Conflicts of Interest

The authors declare no conflicts of interest.

Acknowledgments

References

[1] L. Leiting, W. Guangli, and G. Zhouzheng, "Video summarization generation based on self-attention mechanism and random forest regression," *Computer Engineering and Applications*, vol. 58, no. 4, pp. 198–205, 2022.

[2] W. Hao and P. Li, "Video summarization algorithm based on improved fully convolutional network," *Laser & Optoelectronics Progress*, vol. 58, no. 22, pp. 415–423, 2021.

[3] H. Gharbi, S. Bahroun, and M. Massaoudi, "Key frames extraction using graph modularity clustering for efficient video summarization," in *Proceedings of the 2017 IEEE International Conference on Acoustics, Speech and Signal Processing*, New Orleans, USA, March 2017.

[4] J. Wu, S. h. Zhong, J. Jiang, and Y. Yang, "A novel clustering method for static video summarization," *Multimedia Tools and Applications*, vol. 76, no. 7, pp. 9625–9641, 2017.

[5] K. Li, J. Wang, H. Wang, and Q. Dai, "Structuring lecture videos by automatic projection screen localization and analysis," *IEEE Transactions on Pattern Analysis and Machine Intelligence*, vol. 37, no. 6, pp. 1233–1246, 2015.

[6] K. Davila and R. Zanibbi, "Whiteboard video summarization via spatio-temporal conflict minimization," in *Proceedings of the 14th IAPR International Conference on Document Analysis and Recognition (ICDAR)*, Kyoto, Japan, November 2017.

[7] M. R. Rahman, S. Shah, and J. Subhlok, "Visual summarization of lecture video segments for enhanced navigation," in *Proceedings of the 2020 IEEE International Symposium on Multimedia*, Naples, Italy, December 2020.

[8] K. Dutta, M. Mathew, and P. Krishnan, "Localizing and recognizing text in lecture videos," in *Proceedings of the 16th International Conference on Frontiers in Handwriting Recognition (ICFHR)*, Niagara Falls, NY, USA, August 2018.

[9] X. Zhou, C. Yao, and H. Wen, "East: an efficient and accurate scene text detector," in *Proceedings of the 2017 IEEE Conference on Computer Vision and Pattern Recognition*, Honolulu, HI, USA, July 2017.

[10] F. Xu, K. Davila, and S. Setlur, "Content extraction from lecture video via speaker action classification based on pose information," in *Proceedings of the 2019 International Conference on Document Analysis and Recognition (ICDAR)*, Sydney, Australia, September 2019.

[11] Z. Cao, G. Hidalgo, T. O. P. Simon, S. E. Wei, and Y. Sheikh, "OpenPose: realtime multi-person 2D pose estimation using Part Affinity fields," *IEEE Transactions on Pattern Analysis and Machine Intelligence*, vol. 43, no. 1, pp. 172–186, 2021.

[12] K. Davila, F. Xu, S. Setlur, and V. Govindaraju, "FCN-LectureNet: extractive summarization of whiteboard and chalkboard lecture videos," *IEEE Access*, vol. 9, Article ID 104469, 2021.

[13] M. Liao, Z. Wan, and C. Yao, "Real-time scene text detection with differentiable binarization," in *Proceedings of the Thirty-Fourth AAAI Conference on Artificial Intelligence*, New York, NY, USA, February 2020.

[14] S. Woo, J. Park, and J. Y. Lee, "Cbam: convolutional block attention module," in *Proceedings of the 15th European Conference on Computer Vision (ECCV)*, Munich, Germany, September 2018.

[15] K. He, X. Zhang, and S. Ren, "Deep residual learning for image recognition," in *Proceedings of the 2016 IEEE Conference on Computer Vision and Pattern Recognition*, Las Vegas, NV, USA, June 2016.

[16] J. Dai, H. Qi, and Y. Xiong, "Deformable convolutional networks," in *Proceedings of the IEEE International Conference on Computer Vision*, Venice, Italy, October 2017.

[17] T. Y. Lin, P. Dollar, and R. Girshick, "Feature pyramid networks for object detection," in *Proceedings of the IEEE Conference on Computer Vision and Pattern Recognition*, Honolulu, HI, USA, July 2017.

[18] A. Bewley, Z. Ge, and L. Ott, "Simple online and realtime tracking," in *Proceedings of the 2016 IEEE International Conference on Image Processing (ICIP)*, Phoenix, Arizona,USA, September 2016.

[19] W. Minghu, H. Yongxi, and W. Juan, "Pedestrian detection and tracking method on street based on improved YOLOv3," *Science Technology and Engineering*, vol. 21, no. 17, pp. 7230–7236, 2021.

[20] R. Jiamin, G. Ningsheng, and H. Zhenyang, "Multi-traget tracking algorithm based on YOLOV3 and kalman filter," *Computer Applications and Software*, vol. 37, no. 5, pp. 169–176, 2020.

[21] B. U. Kota, K. Davila, and A. Stone, "Automated detection of handwritten whiteboard content in lecture videos for summarization," in *Proceedings of the 16th International Conference on Frontiers in Handwriting Recognition (ICFHR)*, Niagara Falls, NY, USA, August 2018.

[22] C. Wolf and J. M. Jolion, "Object count/area graphs for the evaluation of object detection and segmentation algorithms," *International Journal on Document Analysis and Recognition*, vol. 8, no. 4, pp. 280–296, 2006.

[23] D. Deng, H. Liu, and X. P. Li, "Detecting scene text via instance segmentation," in *Proceedings of the Thirty-Second AAAI Conference on Artificial Intelligence*, San Francisco, CA, USA, February 2018.

[24] S. Long, J. Ruan, and W. T. Zhang, "A flexible representation for detecting text of arbitrary shapes," in *Proceedings of the 15th European Conference on Computer Vision (ECCV)*, Munich, Germany, September 2018.

Research Article

A Federated Learning-Based Fault Detection Algorithm for Power Terminals

Shuai Hou [ID], Jizhe Lu, Enguo Zhu, Hailong Zhang, and Aliaosha Ye

China Electric Power Research Institute, Haidian District, Beijing 100192, China

Correspondence should be addressed to Shuai Hou; houshuai@epri.sgcc.com.cn

Power terminal is an important part of the power grid, and fault detection of power terminals is essential for the safety of the power grid. Existing fault detection of power terminals is usually based on artificial intelligent or deep learning models in the cloud or edge servers to achieve high accuracy and low latency. However, these methods cannot protect the privacy of the terminals and update the detection model incrementally. A terminal-edge-server collaborative fault detection model based on federated learning is proposed in this study to improve the accuracy of fault detection, reduce the data transmission and protect the privacy of the terminals. The fault detection model is initially trained in the server using historical data and updated using the parameters of local models from edge servers according to different updating strategies, then the parameters will be sent to each edge server and further to all terminals. Each edge server updates the local model via the compressed system log from terminals in its coverage region, and each terminal uses the model to detect fault according to the system behavior in the log. Experiment results show that this fault detection algorithm has high accuracy and low latency, and the accuracy increases with more model updating.

1. Introduction

With the development of the power grid and the applications of information and communication technologies, the smart grid has been widely deployed in most countries, and an automated and distributed advanced energy delivery network has also been constructed. Nowadays, the power terminals, such as smart energy meter, concentrator, special transformer, and energy controller, have become more and more intelligent and important in the smart grid, and the reliability, security, and stability of the power terminals have been challenges for the smart grid. Once the power terminal fails, it will lead to inaccurate power data, confused power scheduling, and damage of power equipment and even part of the power grid. Hence, the fault detection of power terminals with high accuracy is needed to find the faults quickly to avoid the damage to the power grid.

Fault detection is the foundation of the security of power grid. At present, there are many fault detection methods for power terminals, most of which use artificial intelligent or deep learning models to improve the accuracy of fault detection. In these methods, the detection operation is executed on the servers and the state data generated on the terminal of collected by extra devices are transmitted to the server. For example, drone and auto-tracking camera were used to detect the defects in power lines in reference [1]. Bouazza et al. [2] proposed artificial intelligence-based methods to detect faults of the power switches in the wind energy conversion system. Shi et al. [3] proposed a fault detection method based on the LSTM model to predict the faults of DC-DC power supply. Nguyen [4] used a microphone to detect the overload of large power transformer by sound analysis. Hong et al. [5] detected the open conductor fault in power distribution networks using multiple measurement factors of feeder RTUs with DGs. Visible images, infrared images, and ultraviolet images of power equipment were fused to train a deep learning-based fault detection model [6] in a power system. Improved random forest was used to detect the power outage accident of the power terminal in reference [7], and continuous wavelet transform and convolution neural network were adopted to detect faults for power electronic converters in reference [8].

The above fault detection methods can achieve high accuracy mainly by the complex model and massive data. But the complex model will lead to high requirements of computing and storage resource, and massive data may result in congestion and delay of network transmission. Therefore, the fault detection should be at the terminal and the model training should be in the cloud to make full use of the advantages of cloud computing resources and local data to take the accuracy, efficiency, and privacy of fault detection into consideration.

Edge computing is a new framework to provide service at the edge of the network [9, 10]. It has been used in many applications, especially for fault detection of IoT (Internet of Things) devices. An IoT fault detection based on edge computing and blockchain was proposed in reference [11], in which weighted random forest was adopted. Huong et al. developed LocKedge [12] framework to detect low complexity cyberattack in IoT edge computing. Mishra et al. [13] proposed data anomalies detection method at the edge of pervasive IoT systems. A device-edge split architecture for intrusion detection for IoT devices was proposed in reference [14] to reduce the overhead of the IoT devices. The architecture of the power grid is similar to the framework of edge computing, hence researchers have attempted to apply edge computing in the power grid for fault detection. Huo et al. [15] proposed a fault detection based on edge computing for distributed power distribution, and a method based on edge computing architecture was proposed to judge unsafe actions of electric power operations in time in reference [16]. Yang et al. [17] proposed a semisupervised cloud edge collaborative unsafe actions detection framework, and Zhang et al. [18] combined cloud edge fusion framework and deep learning techniques for abnormal object detection in the power grid. These studies overcome the accuracy requirement of fault detection in the power grid by splitting the fault detection to edge server or cloud to reduce the overhead of the power terminals; however, the data privacy of the terminals and the data transmission in the network are not well considered.

Federated learning [19], which is first proposed in 2016, is a machine learning method that takes into account model accuracy and data privacy. It has been used in the power grid to protect the privacy of the data of consumers or terminals. A privacy-preserving federated learning framework Fed-Detect [20] is developed for energy theft detection in smart grid, and a federated learning-based method was proposed for privacy-preserving household characteristic identification in reference [21]. Su et al. [22] proposed a secure and efficient federated-learning-enabled AIoT scheme for private energy data sharing in smart grids with edge-cloud collaboration. Wang et al. [23] developed a distributed electricity consumer characteristics identification method based on federated learning to preserve the privacy of retailers. Liu et al. [24] used an asynchronous decentralized federated learning model for collaborative fault diagnosis of PV stations. These methods protect the privacy of the power terminals but cannot be applied to fault detection because of requirements of the high accuracy, low latency, data privacy, and incremental updating.

To overcome the above problems, we propose a three-tier fault detection model based on federal learning for power terminals and three different model updating strategies in this study. The fault detection model training, updating, and testing are split into edge servers, cloud, and terminals respectively in the power grid. The cloud is responsible for the construction of the initial fault detection model and subsequent model updating to improve the accuracy of fault detection; the edge server is responsible for training the local model to ensure the data privacy of the terminal, and the terminal that only uses the trained model for fault detection to improve the efficiency of fault detection can compress the raw system log to reduce the data transmission. In the data interaction between terminal, edge server, and cloud, the amount of data transmission and system delay is reduced by means of log compression and parameter transmission. The experimental results show that our algorithm can reduce the amount of data transmission and achieve higher accuracy than traditional fault detection methods.

2. Edge-Cloud Collaboration Fault Detection Framework

2.1. Data Model of Power Terminal. The functions and manufacturers of power terminals are different in the power grid, and the configurations of hardware resources are also different. The configuration of some typical power terminals is listed in Table 1. The complex fault detection model cannot be trained on power terminals, but fault detection using the trained model can be performed on most terminals.

The faults of the power terminals involve various functional modules of the embedded operating system, such as hardware driver, system security, file system, system application, and memory management. When a system fault occurs, the system log will record the fault-related information, including the fault occurrence time and system abnormal behaviors. Therefore, the fault detection can be realized through the analysis of the operating system log. Though log formats and the description of system behaviors of different embedded operations are different, the system log usually includes system time, system components, and behavior description. Figure 1 shows the log format of an embedded operating system designed independently, and the record of the system log is in the form of time, device, and detail, where time and device represent the system time and the system component of this system behavior respectively, and detail is the operation description of the system behavior. As shown in the first line in Figure 1, "3.567604" is the relative time after system startup, "USB usb3" is the system component, and "Manufacture: Linux 3.10.108 ohci_hcd" is the system description.

The system fault detection of power terminal needs to find the fault and judge the type of fault as soon as possible after it happens, so that the users can quickly deal with the fault to avoid serious accidents, such as terminal hardware damage, data loss, and network intrusion. When the system fails, the *device* and *detail* attributes of the system log record

TABLE 1: Configurations of typical power terminals.

	Smart meter	Special transformer	Fusion terminal	Energy controller
Frequency	≥120 MHz	≥300 MHz	≥1 GHz	≥1.2 GHz
RAM	≥512 KB	≥512 MB	≥2G B	≥2 GB
Flash (code)	≥512 KB	≥128 MB	≥8 GB	≥4 GB
Flash (storage)	≥8 MB			
Memory protection	MPU (memory protection unit)	MMU (memory management unit)	MMU (memory management unit)	MMU (memory management unit)
Architecture	Arm Cortex-M4	ARM 920T™	ARM Cortex™-A7	ARM Cortex™-A7

[3.567604] usb usb3: Manufacturer: Linux 3.10.108 ohci_hcd

[3.573805] usb usb3: SerialNumber: sunxi-ohci

[3.579445] hub 3-0:1.0: USB hub found

[3.583635] hub 3-0:1.0: 1 port detected

[3.588858] usbcore: registered new interface driver usb-storage

[3.595695] usbcore: registered new interface driver ums-alauda

[3.602414] usbcore: registered new interface driver ums-cypress

[3.609211] usbcore: registered new interface driver ums-datafab

FIGURE 1: Example of system log of power terminals.
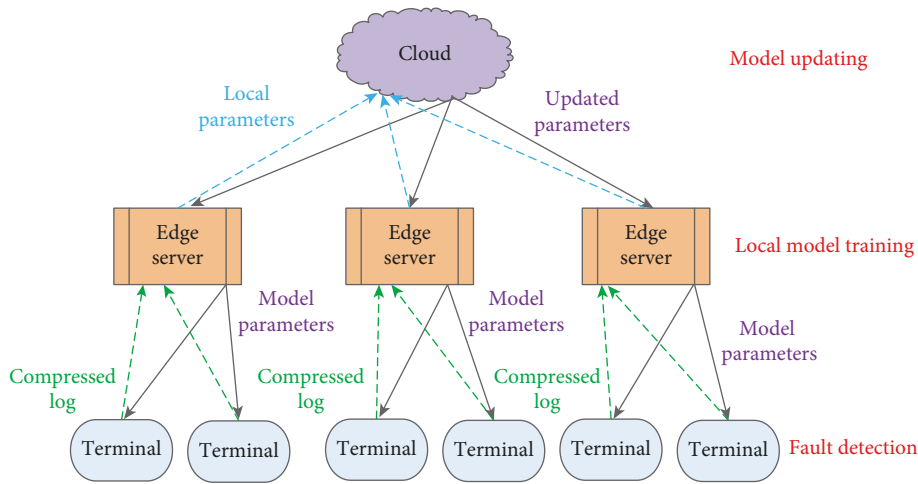
FIGURE 2: Three-tier fault detection architecture.

the abnormal behavior or operations of the system devices. Some common system faults can be found through the keywords in the *detail* attribute of the system log, and the system log usually contains some fault-sensitive words such as failed, error, and warning, as listed in Table 2. However, some system faults caused by hidden bugs or premeditated external attacks may not contain these fault-sensitive words, and the specific type of the system fault is difficult to determine by keywords. Therefore, it is necessary to analyze the system log using natural language processing methods to accurately identify and classify the faults.

Though the system log records the system behaviors and operations when the system failure occurs, the content of the system log is generally simplified in the embedded operating system. Therefore, it is necessary to take the language characteristics of the system log into consideration when using natural language processing methods:

(1) *Short Sentence*: Each record of the system log has less content, the fault location is usually a specific word or number of the system component, and the fault description is usually a short sentence, which contains only a few words. The syntax structure of the sentence is simple.

(2) *Less Vocabulary*. There are less vocabularies in the whole system log. The frequencies of most words in the system log are high, while some words with lower frequency are usually related to the identification of the terminal and have nothing to do with the type of the fault, such as specific IP addresses.

TABLE 2: Examples of sensitive words.

ID	Detail of the system log
1	Warning: get ephy clock is failed
2	Warning: mountpoint for pids not found
3	Console-setup.service: failed with result "exit-code"
4	Failed to start: set console font and keymap
5	Sunxi-ahci: Probe of sata failed with error −1
6	Error while tracing: no such file or directory

(3) *High Redundancy.* The system log generated by each terminal contains a large number of repeated records, and the system logs generated by similar terminals also have a large amount of redundancy. The redundant records are typically representing normal operations.

Therefore, in order to improve the efficiency of fault detection by natural language processing, the redundant records in the system log should be removed to reduce the number of records to be processed. In the process of recognition, the characteristics of short sentences and less vocabulary should be taken into consideration to reduce the complexity of the detection model.

2.2. Fault Detection Framework. Considering the data model and hardware configuration of power terminals, the requirements of fault detection accuracy and delay, as well as the network architecture of power grid, a three-tier fault detection architecture, namely, end-edge-cloud, for power terminals is proposed in this study, as shown in Figure 2. The fault detection model is trained initially and updated in the cloud, and the terminals detect the fault using the detection model. Each edge server is used to train the local model using data from the terminals in its coverage region to protect the privacy of the terminals and generate the parameters of the updated model for the cloud.

(1) *Power Terminals.* They are deployed to perform measuring, monitoring, controlling, and other functions in the power grid, such as energy controllers, fusion terminals, intelligent meters, and special transformer terminals. The power terminals are designed, manufactured, and used by different companies or end users, and they typically have low hardware configuration, and perform different tasks by running different application software. The faults of the power terminal and the abnormal behaviors resulted by the faults are recorded in the system log, hence the fault detection should be performed on the power terminal to detect the fault as soon as possible. Power terminals are the main participants of fault detection and are responsible for the collection and preprocessing detect system log and the detection of the faults.

(2) *Edge Servers.* They can be either the dedicated servers or powerful terminals, which have a large number of computing and storage resources and can perform

the collection and processing of large datasets. Each edge server is responsible for the collection of system logs and the training of local fault detection model for multiple terminals in a distinct region. The edge server acts as the role of connector of the terminals and the cloud in the fault detection architecture, and they interact with the cloud for the parameters of fault detection model, terminals for the updated parameters of the fault model, and the compressed system logs.

(3) *Cloud.* With powerful computing power and storage resources, it is deployed and maintained by the power grid company and is responsible for the initialization and update of the global fault detection model. In practice, one or several large data centers are constructed as the cloud of the power grid, and they are the control and decision centers of the power grid.

The end-edge-cloud three-tier architecture is the common architecture of the practical power grid, hence the three-tier fault detection model can be easily deployed and completed without extra hardware support. Due to the limited network transmission capacity of the terminals, the bandwidth constraints of the edge server, the long transmission distance between the edge server and the cloud, and the data size and delay of data transmission between the cloud, edge server, and terminals greatly affect the training and detection performance of the fault detection model. Therefore, the amount of data transmission between terminals, edge server, and the cloud should be minimized to improve fault detection performance.

From the perspective of model training, the cloud performs the training of the initial fault detection model and the updating of model. The edge server is responsible for collecting the compressed system log of the terminals and training the local fault detection model. The terminal uses the trained model to detect the system fault. The powerful computing resource of the cloud can quickly complete the model training and updating. The local model training can also be quickly accomplished with the small dataset on the edge server. The fault detection on the terminals only has a little demand for computing resources.

From the perspective of data transmission, the system log generated by the terminal will be compressed and transmitted to the adjacent edge server, which greatly reduces the amount of data and occupies less network bandwidth. The edge server transmits the parameters of the local model to the cloud and the parameters of updated model to terminals. Although the distance between the edge server and cloud is long, the transmission delay is very small because the parameters of the model is far less than the raw system logs.

3. Federated Learning-Based Fault Detection Algorithm

The spirit of federated learning is used in the three-tier fault detection framework to reduce the data transmission between the cloud and edge servers and protect the privacy of power terminals. The fault detection algorithm consists of

three steps: pretraining, local training, and model updating. The pretraining step is processed in the cloud, the local training is completed on the edge server, and the model updating is finished in the cloud.

3.1. Pretraining.

The cloud uses historical system logs to train the initial fault detection model, and the system logs are marked and provided by the manufacturers and managers. Each record in the system log is in the form of device, time, detail, and result, where device is the type of the terminal; time, device, and detail are the system time, system component, and system behavior of the fault respectively; *result* is a nonnegative integer and represents the type of the fault. The natural language processing method is adopted to recognize the fault from the system behavior in the system log. The description of the system behavior is recorded in the system log in the form of detail $= (w1, w2, w3, \ldots, wm)$, where m is the number of words and w_i is the ith word, $1 \leq i \leq m$.

The LSTM (long short-term memory) network model is used in our fault detection model to improve the accuracy of fault detection. LSTM is an improvement of RNN (recurrent neural network), and it uses an input gate, forget gate, and output gate to selectively retain part of the previous cell state and transfer it to the next cell to overcome the problem of long-term dependence in RNN. Each cell state in LSTM is consisted of one forget gate, one input gate, and one output gate, and each gate is composed of a sigmoid neural network layer and a pointwise operation, as shown in Figure 3.

The forget gate is used to forget part of the information of the previous cell state C_{t-1}, and only $f_t * C_{t-1}$ is remained in the current cell state, where f_t is the output coefficient of a sigmoid layer:

$$f_t = \text{sigmoid}\left(w_f\left[h_{t-1}, x_t\right] + b_f\right). \tag{1}$$

The input gate is used to determine which new information will be keep in the current cell state, and the new information is defined as $i_t * \widetilde{C}_t$, where i_t is the output of sigmoid layer and $\widetilde{C}_t$ is the output of a tanh layer:

$$\begin{aligned} i_t &= \text{sigmoid}\left(w_i\left[h_{t-1}, x_t\right] + b_i\right), \\ \widetilde{C}_t &= \tanh\left(w_c\left[h_{t-1}, x_t\right] + b_c\right). \end{aligned} \tag{2}$$

The current cell state C_t can be obtained after the forget gate and input gate:

$$C_t = f_t * C_{t-1} + i_t * \widetilde{C}_t. \tag{3}$$

The output gate is used to generate the output h_t of current cell state C_t. The output coefficient o_t and tanh will be computed to get the output h_t:

$$\begin{aligned} o_t &= \text{sigmoid}\left(w_0\left[h_{t-1}, x_t\right] + b_0\right), \\ h_t &= o_t \tanh\left(C_t\right). \end{aligned} \tag{4}$$

3.2. Local Training.

After completing the LSTM model training, the cloud sends the parameters of the fault detection model to each edge server, which then sends the parameters to all terminals in its corresponding region. During the execution of the terminal, the system log will be preprocessed and input into the fault detection model to obtain the fault detection results, and finally, the terminal carries out corresponding response, such as restart, shutdown, and alarm. Because only fault detection is performed on the terminal, and the model training and updating are performed on the edge server and cloud, the terminal can quickly detect and respond the fault.

Due to the high reliability and security requirements of power grid, the failure probability of each terminal is very low, most records in the system log are normal operations, and only a few records are abnormal system behavior in a long time. Hence, the system log on each terminal contains a lot of redundant information, and it should be compressed before being transmitted to the edge server to reduce the amount of data transmission. Log compression is mainly divided into three steps:

① *Variable Replacement.* Some variables in the system log represent the identification of the device or network and do not contain the semantics of the fault. These variables are usually long words or strings and can be replaced with the category of these variables, such as IP address and web page address, and device name can be replaced with IP, URL, and local, so as to reduce the differences between records in the system log and reduce the data transmission between the terminal and edge server.

② *Similarity Computing.* Each record of the system log contains the system component and the system behavior of the fault, and the records with high similarity will be compressed into one record to reduce the data transmission. Hence, the similarity of two records consists of the similarity of the system component S_{device} and that of the system behavior S_{detail}. The similarity of two system components depends on the locations of the components in the fault tree:

$$\begin{aligned} &S_{\text{device}}\left(\text{device}_1, \text{device}_2\right) \\ &= \begin{cases} 1, & \text{device}_1 = \text{device}_2 \\ \dfrac{1}{\text{max length}}, & \text{device}_1 \neq \text{device}_2 \end{cases}, \\ &\text{maxlength} = \max\{P\left(\text{Root}, \text{device}_1\right), P\left(\text{Root}, \text{device}_2\right)\}, \end{aligned} \tag{5}$$

where Root is the nearest common ancestor node of device_1 and device_2 in the fault tree; $p\left(\text{Root}, \text{device}_1\right)$ and $p\left(\text{Root}, \text{device}_2\right)$ are the number of nodes on the path from Root to device_1 and device_2, respectively.

If the detail of the record in the system log contains one or more of words in the set of sensitive words Keywords, then the record is marked as a sensitive record, and the similarity of this record will not be computed because any sensitive record cannot be compressed to ensure the accuracy of the fault
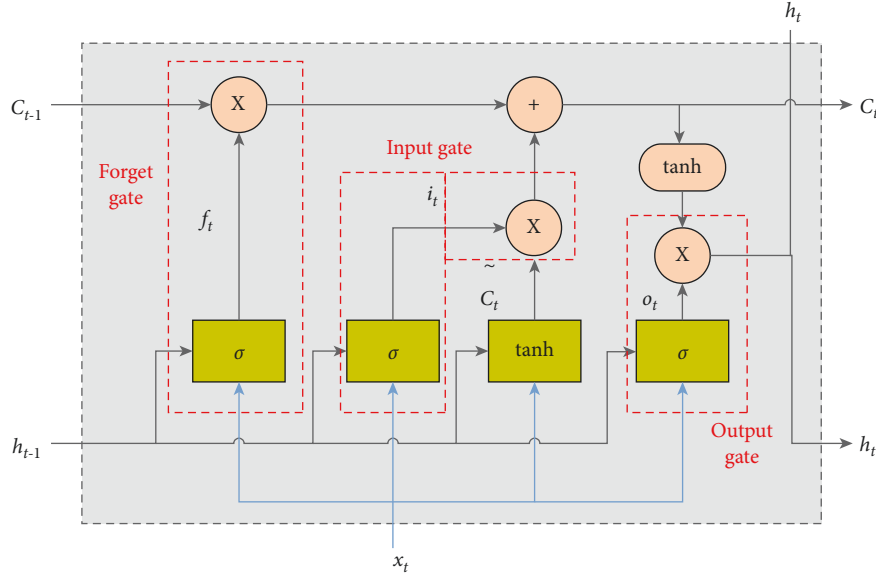
Figure 3: Structure of cell state in LSTM.

detection. For the nonsensitive records, the similarity of the system behavior is related to the words in detail. Given $\text{details}_1 (w_1, w_2, \ldots, w_m)$ and $\text{details}_2 (w'_1, w'_2, \ldots, w'_n)$, the similarity of details_1 and device_2 can be obtained:

$$S_{\text{detail}} (\text{detail}_1, \text{detail}_2) = \frac{\left| \text{detail}_1 \cap \text{detail}_2 \right|}{\left| \text{detail}_1 \cup \text{detail}_2 \right|}, \quad (6)$$

where m and n are the number of words in detail_1 and detail_2 respectively, $\text{details}_1 \cap \text{details}_2$ is the number of words in the intersection of detail_1 and detail_2, and $\text{details}_1 \cup \text{details}_2$ are the number of words in the union of detail_1 and detail_2.

The similarity of two records $r_1 = (\text{time}_1, \text{device}_1, \text{details}_1)$ and $r_2 = (\text{time}_2, \text{device}_2, \text{details}_2)$ in the system log $S(r_1, r_2)$ is the weighted sum of the similarity of S_{device} and S_{details}:

$$\begin{aligned} S(r_1, r_2) = {}& \alpha \cdot S_{\text{device}} (\text{device}_1, \text{device}_2) \\ & + \beta \cdot S_{\text{detail}} (\text{detail}_1, \text{detail}_2), \end{aligned} \quad (7)$$

where α and β are the coefficients of S_{device} and S_{details} respectively and can be set by the domain experts, such as system designers, maintainers, and testers.

③ *Redundancy Filtering.* Log records with high similarity generated in a short time are called redundant records. The redundant logs should be discarded on the terminal, and only the remaining log records will be transmitted to the edge server to reduce the data transmission. The filtering process is as follows: first, all the sensitive log records should be retained, that is, the record $r_i = (\text{time}_i, \text{device}_i, \text{details}_i)$ with $\text{details}_i = (w_1, w_2, \ldots, w_m)$ will be transmitted to the edge

server if $w_j \in \text{detail}_j$ and $w_j \in \text{Keywords}_j$. If r_j is not a sensitive record, then its similarity with any non-sensitive record r_j, $S(r_i, r_j)$, is calculated in the subsequent short time interval. The log record r_j with $S(r_i, r_j) \geq S_{th}$ will be marked as redundant record and discarded on the terminal, where S_{th} is the similarity threshold set by the system manager or other experts.

After receiving the compressed system logs from terminals in its region, the edge server performs the local training of the fault detection model using the data received. Then, the parameters of the updated local model are transmitted to the cloud to update the global fault detection model. Due to the low probability of system failure of each terminal, the local training should not be performed frequently. For example, a manufacturer of power terminal found that the system failure of each terminal occurs once every two months during on-site use, according to a pilot testing of energy controller since April 2021. If the fault detection model is trained frequently using the dataset without fault records, then it may lead to overfitting of the fault detection model. In order to ensure the detection accuracy of fault detection model, three strategies of local training are proposed in this study.

① *Periodic Update (PUpdate).* Each edge server trains its local model within a specified period. The parameter period is set according to the reliability of the terminals in the coverage region of the edge server, and it is set to be the average failure time of the terminals by default. Given the edge server server_i and the set of terminals in its coverage region $P_i = (p_{i,1}, p_{1,2}, \ldots p_{i,k})$, the failure time of the terminal $p_{i,j}$ is ft_j, and we can obtain the update period of edge server server_i as follows:

$$\text{period}_i = \frac{1}{k} \sum_{j=1}^{k} ft_i, \quad (8)$$

where k is the number of terminals. The update period of different edge servers may also be different and can be adjusted when the terminals in the region are removed or newly deployed.

② *Incremental Update (AUpdate)*. Each edge server starts the local training when the number of abnormal log records is no less than the threshold. Since training the local model using normal records may lead to over fitting, the training dataset should contain some abnormal records. Suppose is the training dataset on edge server server$_i$, Dth is the threshold of the abnormal records, the server$_i$ will perform local training if $|ADataset_i| \geq Dt\ h$, where NDataseti is the set of normal records in Dataseti, and ADataseti is the set of abnormal records in Dataseti. The threshold $Dt\ h = 1$ is generally set as a linear function of the number of terminals in the coverage region of the edge server, and the threshold on each edge server may be different.

③ *Triggered Update (TUpdate)*. The edge server performs the local training when receiving abnormal log records from any terminal in its coverage region. The local fault detection model may be updated as soon as possible in this strategy, and the updated parameters will be sent to the cloud. It may lead to a large amount of data transmission between the edge servers and the cloud when there are many terminals in the power grid. This strategy can be seen as a special case of AUpdate with threshold $Dt\ h = 1$.

The above three strategies should be used in different situations; PUpdate and AUpdate can reduce the data transmission between edge servers and the cloud, while TUpdate can quickly update the fault detection model. We can choose different strategies according to the practical applications, and the strategies can be adopted on different edge servers simultaneously. The main difference of the three updating strategies is the updating frequency of the fault detection model; TUpdate may lead to high and unpredictable updating frequency, while the updating frequency of PUpdate and AUpdate can be controlled by changing parameters period and $Dt\ h$.

3.3. Model Updating.

After receiving the parameters of local models from edge servers, the cloud will aggregate the parameters to update the global detection model and then send the updated parameters to all edge servers. Each edge server will further send the updated parameters to all terminals in its coverage region. Suppose the parameters of local models from k edge servers are the set $V = \{v_1, v_2, \ldots, v_k\}$, and the parameters of each local model are a vector $V_i = \langle v_1^i, v_2^i, \ldots, v_p^i \rangle$, where $1 \leq i \leq k$ and p is the number of parameters of the fault detection model. The set of parameters V is aggregated in the cloud, and we can get the new parameter vector $V_u = \langle v_1^u, v_2^u, \ldots, v_p^u \rangle$, in which each parameter is updated according to the following rules:

$$v_i^u = \eta.v_i^{'u} + (1 - \eta)\sum_{j=1}^{k} v_i^j, \qquad (9)$$

where $v_i^{'u}$ is the original value of the ith global parameter, and η is the weighted coefficient and can be obtained by the cloud in the step of pretraining.

The accuracy of the fault detection model on the terminals depends on the frequency of model updating in the cloud, if the architecture of the grid power and the method to process the system log are given. The parameters of local models from the edge servers will be less when the cloud updates the global model frequently, which will increase the data transmission to send the updated parameters to all the edge servers and terminals. If the frequency of model updating is low, then some edge servers, on which the frequency of local training is high, will send their local parameters several times to the cloud, and only the latest version of the local parameters will be aggregated to update the global model, so that the influences of some faults will be ignored and the accuracy of the fault detection model will be affected.

Therefore, in order to improve the accuracy of the fault detection model, the cloud can adopt different strategies to update the model, such as PUpdate, AUpdate, and TUpdate. These update strategies in the cloud for model updating are similar to that on the edge server for local training, and the only difference is the measurement of the thresholds in each strategy. The update period of PUpdate in the cloud is typically set as the shortest time of local training on all edge servers. The threshold of AUpdate in the cloud will be set according to the number of edge servers, which have been finished the local training, that is, the number of parameter vectors received by the cloud. The cloud will update the model when receiving parameters of local model from any edge server when TUpdate is used in the cloud. The update strategy in the cloud is determined by the experts according to the requirements and configurations of the power grid and the strategies adopted on the edge servers.

3.4. Fault Detection Algorithm.

Suppose there are one cloud Cloud and k edge servers $\{\text{Server}_1, \text{Server}_2, \ldots, \text{Server}_k\}$ in the power grid, and the terminals in the coverage region of edge server Server$_i$ are $\{de\ v_{i_1}, de\ v_{i_2}, \ldots, de\ v_{i_n}\}$, then the fault detection process is as follows:

Step 1. The historical system logs Records are used to pretrain the initial fault detection model using LSTM in Cloud. Then, Cloud sends the parameter vector V_{init} to all edge servers $\{\text{Server}_1, \text{Server}_2, \ldots, \text{Server}_k\}$, and each edge server Server$_i$ further sends V_{init} to the h terminals $\{de\ v_{i_1}, de\ v_{i_2}, \ldots, de\ v_{i_n}\}$ in its coverage region.

Step 2. When a log record r_i is generated on a terminal $de\ v_{i_j}$, it should be firstly preprocessed by variable replacement and input into the fault detection model to check whether a fault occurs and determine the type of the

fault on dev_{i_j}. Then, the log records within a time period will be compressed and sent to the edge server Server_i.

Step 3. Each edge server Server_i collects the compressed system logs $R_i = \left\{R_{i_1}, R_{i_2}, \ldots, R_{i_h}\right\}$ from terminals $\left\{de\ v_{i_1}, de\ v_{i_2}, \ldots, de\ v_{i_n}\right\}$ in its coverage region and trains the local LSTM model using dataset R_i according to the updating strategy, such as PUpdate, AUpdate, or TUpdate. Once completing the local training, Server_i transmits the parameters V_i of local model to Cloud.

Step 4. After receiving the parameters $V = \{V_1, V_2, \ldots, V_k\}$ from edge servers $\{\text{Server}_1, \text{Server}_2, \ldots, \text{Server}_k\}$, Cloud aggregates V to generate the new parameters $V_{\text{update}} = \langle v_1^u, v_2^u, \ldots, v_p^u \rangle$ using PUpdate, AUpdate, or TUpdate strategy. Then, V_{update} will be transmitted to each edge server Server_i, and finally to all terminals $\left\{de\ v_{i_1}, de\ v_{i_2}, \ldots, de\ v_{i_n}\right\}$, and steps 2–4 will continue until the fault detection is interrupted.

In the above algorithm, each terminal continuously generates a large amount of system log, and each record in the system log is input into the fault detection model to find as many faults as possible. The system log will be compressed before transmitting to the edge server, and only the parameters of local model are sent to the cloud to reduce the transmission delay. Meanwhile, the fault detection on the terminal, the local model training on edge server, and the model updating in the cloud can fully utilize the computing resources of different hardware. Therefore, high accuracy, low latency, less data transmission, and privacy protection are taken into consideration in this federated learning-based fault detection algorithm.

4. Performance Evaluation

The fault detection algorithm proposed in this study is evaluated in a simulated power grid with a cloud, 10 edge servers, and a number of terminals. The terminal is configured as a brand of energy controller, the system log is collected in practical application, and the summary of the system log is listed in Table 3. The time of model updating, the amount of data transmission of each terminal, and the fault detection accuracy are tested to evaluate our fault detection algorithm. The weights in the similarity of records are set as $\alpha = \beta = 0.5$.

The average update time of the model using different update strategies when the number of terminals in the coverage region of the edge server changes is shown in Figure 4. It can be seen that the update time of PUpdate strategy keeps stable if the update period is fixed, while the update time of AUpdate and TUpdate strategies decreases with the increase of terminals. The reason is that the increase terminals lead to high frequency of the edge server receiving abnormal log records, and the local update will be performed more frequently if the other conditions is fixed. Since the threshold D_{th} in AUpdate is set to be 10, and the TUpdate can be seen as a special case of AUpdate with $D_{\text{th}} = 1$, the average update time of TUpdate is significantly lower than that of AUpdate strategy for the same number of terminals.

Table 3: Summary of system log generated by an energy controller within an hour.

No.	Information	Value
1	Number of log records	1019
2	Average number of words per record	9.25
3	Maximum frequency of the words	880
4	Minimum frequency of the words	1
5	Size of raw system log	70 KB
6	Size of compressed system log	18 KB
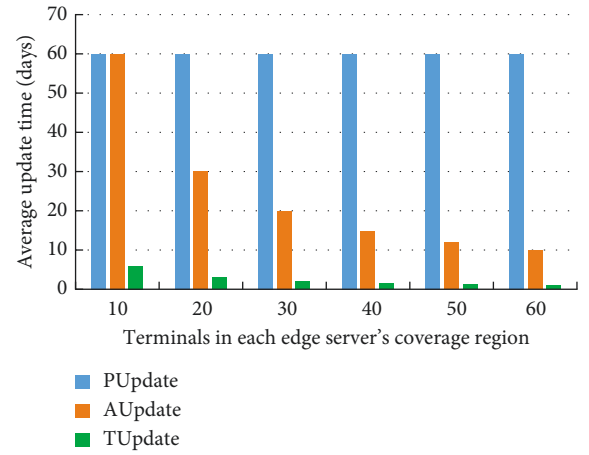
Figure 4: Average update time of the fault detection model.
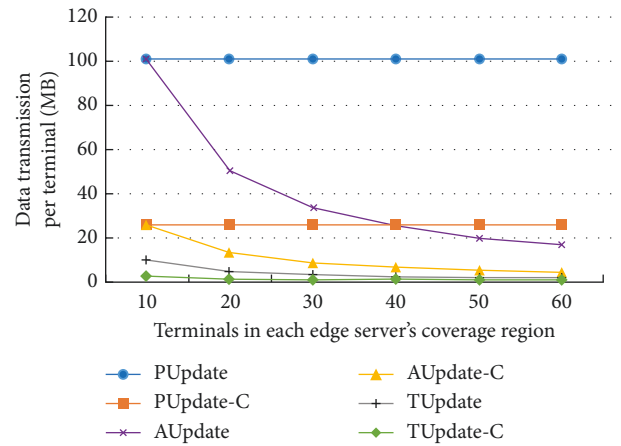
Figure 5: Average data transmission of a power terminal in the fault detection model.

The average data transmission of each terminal for the local training on edge server with different update strategies is shown in Figure 5. The legends "X" and "X-C" represent the two cases when the terminal transmits raw system log and compressed system log to edge server with update strategy X respectively. It can be seen from Figure 5 that log compression can significantly reduce the data transmission in all update strategies, and PUpdate generates the largest data transmission, followed by AUpdate, and data transmission in TUpdate is the smallest. The main reason is that PUpdate takes the longest period for each local training, while the average time of local training in TUpdate is the
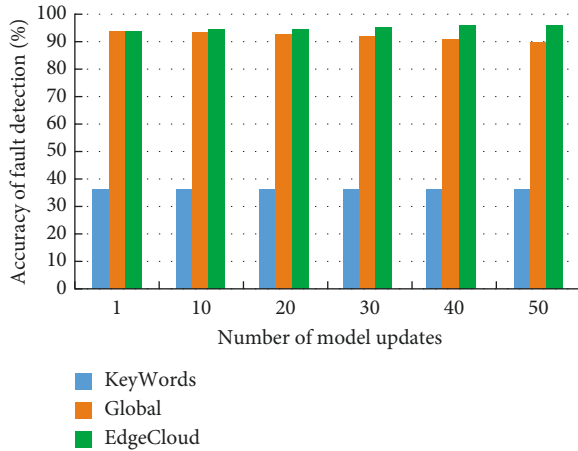
Figure 6: Accuracy of the fault detection results.

shortest. Meanwhile, when the number of terminal devices increases, the model update time of AUpdate and TUpdate gradually approaches. In the case of log compression, the data transmission of AUpdate and TUpdate approximates to be equal.

From the above results, it can be seen that the PUpdate strategy has the longest update period and the largest amount of data transmission for each local training. The TUpdate has the shortest update period and the least data transmission for each local training. The update period and data transmission in AUpdate are less than that of PUdate and more than that of TUpdate. In practical applications, TUpdate is suitable for newly deployed terminals and terminals with high security requirements, so as to quickly collect the abnormal system records of the terminal and train a more accurate fault detection model. Terminals with limited network bandwidth can also avoid network congestion and packet loss caused by a large amount of data transmission using TUpdate strategy. PUpdate is applicable to terminals with stable operation, less strict security requirements, and large network bandwidth, and the update period can be set according to the actual application and is usually initialized as the average failure time of the terminal. Strategy AUpdate has the maximum flexibility, the update period can be changed easily by modify the threshold D_{th}, and the update period grows as D_{th} become larger.

The accuracy of fault detection using different fault detection methods is shown in Figure 6. The legends "KeyWords" is the keyword matching-based method, "Global" is the global LSTM model, that is, the fault detection model is trained in the cloud and cannot be updated, and "EdgeCloud" is our LSTM model with edge and cloud cooperation. The results show that the accuracy of Keywords method is very low since the abnormal behavior of some faults does not contain the keywords. The accuracy of both Global and EdgeCloud methods is obviously higher than KeyWords because the faults are recognized by the natural language processing method LSTM. With the accumulation of the system log, the Global method does not update the fault detection model, which leads to decreasing of the accuracy of fault detection. The new system log is used to

train the local model and further update the global fault detection model to increase the accuracy of the fault detection model. With the increase of the number of model updates in the cloud in EdgeCloud, its accuracy becomes higher than that of Global method.

5. Conclusions

In this study, we analyze the characteristics of power terminal fault detection in the power grid and propose a three-tier fault detection model based on federated learning. The accuracy of fault identification and the privacy protection of terminal are both taken into consideration in this model, then the model training, model updating, and fault detection are performed at different levels. Log compression and transmission of parameters of the model are used to reduce data transmission and protect the privacy, the LSTM model is used to improve fault detection accuracy, and three different model update strategies are used to further improve the accuracy of fault detection. The experimental results show that the log compression method can effectively reduce the amount of data transmission. The three model strategies are suitable for different application scenarios and terminals, and the detection accuracy of our proposed fault detection model is higher than that of the traditional keyword-based models and the global models based on historical data. In the future work, it is planned to integrate our proposed fault detection model into various embedded operating systems and deploy it on different devices.

Data Availability

The data used to support the findings of this study are included within the article.

Conflicts of Interest

The authors declare that they have no conflicts of interest.

Acknowledgments

References

[1] J. Park, S. Kim, J. Lee, J. Ham, and K. Oh, "Automatic inspection drone with deep learning-based auto-tracking camera gimbal to detect defects in power lines," in *Proceedings of the International Conference on Vision, Image and Signal Processing*, pp. 1–46, Vancouver, Canada, August 2019.

[2] H. Bouazza, M. L. Bendaas, T. Allaoui, and M. Denai, "Application of artificial intelligence to wind power generation: modelling, control and fault detection," *International Journal of Intelligent Systems Technologies and Applications*, vol. 19, no. 3, pp. 280–305, 2020.

[3] L. Shi, P. Yu, Z. Zhou et al., "DC-DC power supply fault prediction and analysis based on monitoring parameter simulation and LSTM network model," in *Proceedings of the*

International Conference on Algorithms, Computing and Artificial Intelligence, pp. 1–8, Sanya, China, December 2021.

[4] N. C. Phuong, "Large power transformer overload detection using sound analysis," in *Proceedings of the International Conference on Signal Processing and Machine Learning*, pp. 135–141, Beijing China, August 2021.

[5] J. S. Hong, S. Y. Hyun, Y. W. Lee, J. H. Choi, S. J. Ahn, and S. Y. Yun, "Detection of open conductor fault using multiple measurement factors of feeder RTUs in power distribution networks with DGs," *IEEE Access*, vol. 9, no. 9, pp. 143564–143579, 2021.

[6] Y. Li, F. Yu, Q. Cai et al., "Image fusion of fault detection in power system based on deep learning," *Cluster Computing*, vol. 22, no. 4, pp. 9435–9443, 2019.

[7] T. Yu, M. Xie, X. Li, Y. Ling, D. Bin, and C. Yang, "Network attack detection method for power system terminal based on improved random forest," in *Proceedings of the International Conference on Artificial Intelligence and Information Systems*, vol. 85, pp. 1–85, Chongqing, China, May 2021.

[8] Q. Sun, X. Yu, H. Li, F. Peng, and G. Sun, "Fault detection for power electronic converters based on continuous wavelet transform and convolution neural network," *Journal of Intelligent and Fuzzy Systems*, vol. 42, no. 4, pp. 3537–3549, 2022.

[9] W. Shi, J. Cao, Q. Zhang, Y. Li, and L. Xu, "Edge computing: vision and challenges," *IEEE Internet of Things Journal*, vol. 3, no. 5, pp. 637–646, 2016.

[10] S. Weisong, S. Hui, C. Jie, Z. Quan, and L. Wei, "Edge computing: a new computing model in the era of everything," *Journal of Computer Research and Development*, vol. 54, no. 5, pp. 907–924, 2017.

[11] W. Zhang, J. Wang, G. Han, S. Huang, Y. Feng, and L. Shu, "A data set accuracy weighted random forest algorithm for IoT fault detection based on edge computing and blockchain," *IEEE Internet of Things Journal*, vol. 8, no. 4, pp. 2354–2363, 2021.

[12] T. T. Huong, P. B. Bac, D. M. Long et al., "LocKedge: low-complexity cyberattack detection in IoT edge computing," *IEEE Access*, vol. 9, no. 9, pp. 29696–29710, 2021.

[13] A. Mishra, A. Cohen, T. Reichherzer, and N. Wilde, "Detection of data anomalies at the edge of pervasive IoT systems," *Computing*, vol. 103, no. 8, pp. 1657–1675, 2021.

[14] A. Mudgerikar, P. Sharma, and E. Bertino, "Edge-based intrusion detection for IoT devices," *ACM Transactions on Management Information Systems*, vol. 11, no. 4, pp. 1–18, 2020.

[15] W. Huo, F. Liu, L. Wang, Y. Jin, and L. Wang, "Research on distributed power distribution fault detection based on edge computing," *IEEE Access*, vol. 8, no. 8, pp. 24643–24652, 2020.

[16] Y. Yin, J. Lin, N. Sun et al., "Method for detection of unsafe actions in power field based on edge computing architecture," *Journal of Cloud Computing*, vol. 10, no. 1, pp. 1–17, 2021.

[17] Y. Yang, J. Mao, Y. Chen, H. Zhong, Z. Huang, and Y. Wang, "Semi-supervised cloud edge collaborative power transmission line insulator anomaly detection framework," *Lecture Notes in Computer Science*, in *Proceedings of the International Conference on Image and Graphics*, pp. 210–221, Haikou, China, August 2021.

[18] S. Zhang, J. Wang, J. Tong, J. Zhang, and M. Zhang, "Cloud-edge fusion based abnormal object detection of power transmission lines using incremental learning," *IEEE Access*, vol. 8, no. 8, pp. 218694–218701, 2020.

[19] B. McMahan, E. Moore, D. Ramage, S. Hampson, and B. A. Arcas, "Communication-efficient learning of deep networks from decentralized data," in *Proceedings of the International Conference on Artificial Intelligence and Statistics*, pp. 1273–1282, Florida, FL, USA, April 2017.

[20] M. Wen, R. Xie, K. Lu, L. Wang, and K. Zhang, "FedDetect: a novel privacy-preserving federated learning framework for energy theft detection in smart grid," *IEEE Internet of Things Journal*, vol. 9, no. 8, pp. 6069–6080, 2022.

[21] J. Lin, J. Ma, and J. Zhu, "Privacy-preserving household characteristic identification with federated learning method," *IEEE Transactions on Smart Grid*, vol. 13, no. 2, pp. 1088–1099, 2022.

[22] Z. Su, Y. Wang, T. H. Luan et al., "Secure and efficient federated learning for smart grid with edge-cloud collaboration," *IEEE Transactions on Industrial Informatics*, vol. 18, no. 2, pp. 1333–1344, 2022.

[23] Y. Wang, I. L. Bennani, X. Liu, M. Sun, and Y. Zhou, "Electricity consumer characteristics identification: a federated learning approach," *IEEE Transactions on Smart Grid*, vol. 12, no. 4, pp. 3637–3647, 2021.

[24] Q. Liu, B. Yang, Z. Wang et al., "Asynchronous decentralized federated learning for collaborative fault diagnosis of PV stations," *IEEE Transactions on Network Science and Engineering*, vol. 9, no. 3, pp. 1680–1696, 2022.

Hindawi

Research Article

Research on Image Texture Feature Extraction Based on Digital Twin

Juan Li [ID] [1,2]

[1]*School of Computer Engineering, Jinling Institute of Technology, Nanjing, Jiangsu 211169, China*
[2]*Jiangsu Provincial Key Laboratory of Data Science and Intelligent Software, Nanjing, Jiangsu 211169, China*

Correspondence should be addressed to Juan Li; iamlj6@jit.edu.cn

The purpose of image smoothing is to improve the visual effect of the image and improve the clarity of the image, so as to make the image more conducive to computer processing and various feature analysis. Because the current technology fails to smooth the preprocessed image, it leads to the extraction of image texture features. The anti-interference performance is weak. For this reason, an image texture feature extraction technology based on the digital twin is proposed. Similarity analysis is carried out through the internal structure of the image, and the image is smoothed by the semisupervised learning method. On the basis of optimizing the denoised image through digital twinning, detect target feature points in the original image, then remove the abnormal and split feature points, assign the direction of image texture feature points, and build a fuzzy back propagation neural network model. Image texture feature extraction technology is implemented. The experimental results show that, compared with the traditional method, the proposed technique has a strong identification of original image features, and has a strong consistency with original data, and has a strong ability to resist the influence of abnormal data, noise, or redundant feature points.

1. Introduction

As an important carrier of information transmission, the effective study of images is the key to information data processing [1, 2]. Image texture feature extraction, as a key technology in information data processing, often becomes a hot and difficult point in image information research. For image feature extraction [3], it greatly increases the complexity of image processing. Effective extraction of various features in the image, in which the quality of feature points, the base of the number, the location, and distribution of the feature points will directly affect whether the subsequent imaging and matching work can be carried out smoothly [4]. Therefore, before carrying out specific imaging work, it is essential to perform different texture feature extraction work for different types of images, and it is also the basis and premise for the effective implementation of all technical means, which is of great significance to imaging work [5].

How to accurately extract image texture features has become the focus of current research on image information.

Tarsitano et al. [6] utilize automatic machine learning methods for image feature extraction and classification. The possibility of applying machine learning methods designed for one-dimensional problems to the task of galaxy image classification is explored. Algorithms for image classification typically rely on multiple costly steps to extract features from galaxy images by analyzing the light distribution of elliptical isoilluminance maps and gather information sequentially. Sequences obtained with this method exhibit well-defined characteristics. Sequences are then trained and classified using machine learning algorithms designed by the Modulos AutoML platform, and how they optimize the classification task. However, this method is not optimized by the digital twin, and the image edge retention ability is poor, resulting in a slow running speed of image texture feature extraction. Kumar et al. [7] proposed the application of tetrolet-based adaptive color and texture feature extraction in content-based image retrieval, and designed a content-based image retrieval system that utilizes all these original image features to achieve an efficient content-based image retrieval system.

Natural images contain fully overlapping information, so in this approach, relevant image features are evaluated from their respective components. The YCbCr color space is used for the feature extraction process because the overlap of the Y, Cb, and Cr color planes is minimal. However, this method is not optimized by digital twinning, and the filtering effect of image detail information is weak, resulting in a low image texture recognition rate. In order to solve the problems of the above methods, an image texture feature extraction technology based on the digital twin is proposed. Based on the above denoising of the image and the optimization of the denoised image through digital twinning, to realize the image texture feature extraction technology, it is necessary to detect the target feature points in the original image, and then eliminate the abnormal and split feature points, so as to improve the extraction efficiency, reduce the error rate, and facilitate the effective implementation of the subsequent process. Compared with the angular and gradient features of the original image, the image extreme value feature based on Gaussian function is more stable, which can ensure the simplicity and accuracy of image texture feature extraction. Detecting all features of the original image in the GSS scale space can effectively remove abnormal feature points. The innovation of this technology is to analyze the intrinsic structural similarity of the image and smooth the image. On the basis of optimizing the denoised image through digital twinning, target feature points in the original image are detected, and then abnormal and split feature points are eliminated, and the direction of image texture feature points is assigned to realize the research of image texture feature extraction technology based on digital twinning. The research shows that the designed technology has better performance.

2. Image Texture Feature Extraction Technology

There is no clear and unified definition of image texture features. It is generally understood as the spatial change and repetition of the image gray level, or repeated local patterns (texture primitives) and their arrangement rules in the image. Texture feature extraction refers to the process of extracting texture features through certain image processing technology, so as to obtain the quantitative or qualitative description of the texture. Therefore, texture feature extraction should include two aspects: image preprocessing and image digital twin optimization.

2.1. Image Preprocessing. In terms of image preprocessing, the existing feature extraction technology has been widely used in image denoising and has achieved a good denoising effect. However, for the threshold denoising method, although the obtained estimated wavelet coefficient has good continuity, when the wavelet coefficient is greater than the threshold, there will be a constant deviation between the wavelet coefficient and the estimated wavelet coefficient. It will affect the proximity between the reconstructed image signal and the actual signal, and the error of the

reconstructed signal will increase [8]. Therefore, for the above problems, the wavelet threshold denoising method is optimized to obtain an improved wavelet threshold denoising method. The specific steps are described as follows:

Formula (1) is a new threshold function.

$$Q_I = \begin{cases} Q_i + \dfrac{2\alpha \times \lambda}{1 + \exp(x)}, & |Q_i| \geq \alpha, \\ \\ 0, & |Q_i| < \alpha. \end{cases} \tag{1}$$

In formula (1), Q_i represents the wavelet coefficient, $\exp(x)$ represents the threshold function, and α represents the wavelet reconstruction value, $\lambda = 0.5$. Wavelet reconstruction is carried out through the new threshold function to obtain the estimated signal, that is, the signal after past noise.

$$F(k) = \alpha + \dfrac{2\alpha \times \lambda}{1 + \exp(x)} \times Q_I. \tag{2}$$

In the process of image preprocessing, the data containing labels are often very scarce, and they also need to be processed manually. Generally, unlabeled data account for a large proportion. The image is smoothed and preprocessed mainly through digital twins. In the process of preprocessing, the target classification function needs to be optimized in time [9]. We analyze the association relationship of each datum x_i and y_j in the dataset and establish the association matrix a_s. When $i \neq j$, the following definition need to be set.

$$W_j = E_{XP}\left(\dfrac{(x_i - y_j)^2}{2 \times F(k)} - a_s\right). \tag{3}$$

In formula (3), E_{XP} represents a diagonal matrix. An iterative function is established to solve the optimal label set E. The specific expression is as follows:

$$E(t) = W_j + (1 - \alpha) \times \beta. \tag{4}$$

In formula (4), β represents the regularization parameter. The main purpose of establishing a tag set E is to complete the transmission of different tags, that is, the data with tags are transmitted to the data without tags. In the process of transmission, it is necessary to make regularization judgments under set constraints and to give new labels to the data to ensure the smooth transmission of labels under the condition of ensuring that the original data will not be lost.

The main reason for image smoothing preprocessing is to eliminate the noise in the image [10], and to further improve the image quality. At the same time, the image quality is further improved. For a given content image X, both images are images in RGB color space [11], which not only contain the same content features but at the same time, the spatial structure is also very similar. In order to obtain a more ideal feature extraction effect, it is necessary to convert the image into a gray image X_g. First, the gray image X_g is

subjected to mean filtering [12], and all pixel values in the gray image are converted to obtain X_{result}. Then the calculation formula of pixel value conversion is

$$X_r = Int\left(\frac{X_g}{\theta \times X_f}\right). \tag{5}$$

In formula (5), Int represents the gray content image of smooth preprocessing for semi-supervised learning, X_g represents the gray image corresponding to the content image, X_f represents the filtered image of X_g, and θ represents the weight coefficient of X_f.

In the semi-supervised learning method, the association matrix is established through X_r, and the semi-supervised learning method is used to smooth and preprocess the image. Finally, the preprocessed image is obtained as follows:

$$Y_r = (I - S_i)^{-1} \times X_g. \tag{6}$$

In formula (6), S_i represents the weight coefficient of label data smoothing.

2.2. Digital Twin Optimization of Images. After the preprocessed image is obtained, the image to be optimized is assumed and defined as R. The purpose of optimization through digital twinning is to make the obtained output image similar to the input image R [13]; the edge and texture should be the same as the denoised image Q, and the optimized image should be output, defined as P. The digital twin technology is used to perceive the full element and full state digital information of image texture features [14], to optimize the full element and full state features of actual images, and to construct the digital twin image texture feature model in combination with the three-tier architecture design to realize the image texture feature information management [15]. The overall structure of the image texture feature model based on the digital twin is obtained, as shown in Figure 1.

In Figure 1, O represents the central origin, $A_1 (x_1, y_1)$, $B_1 (x_1, y_1)$, and $C_1 (x_1, y_1)$ represent the origin position of the change interval of the image feature threshold, while D_1, D_2, and D_3 represent intersections. According to the digital twin image texture feature model shown in Figure 1, data are extracted through threshold judgment analysis [16, 17]. We realize the functions of digital twin control, equipment monitoring, abnormal alarm, and life prediction, and determine the image texture feature model.

The image is assumed through digital twinning, and the local linear model is established by using the existing relationship between the denoised image Q_i and the filtered output image P_i, that is,

$$P_i = R \times P + a_k Q_i + b_k P_i. \tag{7}$$

In formula (7), a_k and b_k, respectively, represent windows centered on the pixel value k. The same gradient information exists between the denoised image Q and the output image P. The edge information of the denoised image can be effectively retained, which lays a foundation for image
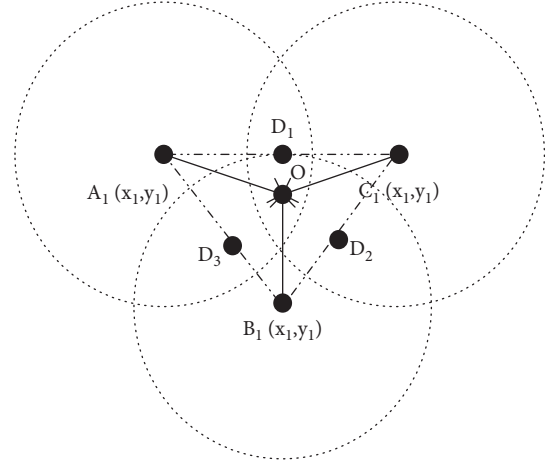
Figure 1: Image texture feature model based on the digital twin.

optimization and promotes basic morphological recognition in the image [18, 19]. The formula enables the output image P to retain the fuzzy information in the original image R to the greatest extent, which needs to be calculated by minimizing the cost function, that is,

$$M(a_k, b_k) = \sum_{i = w_k} (a_k Q_i + b_k - P_i). \tag{8}$$

In order to prevent overfitting, regularization parameters are set. If the value of a_k is too large, overfitting will occur, which will increase overall cost function, which can be expressed as $M(a_k, b_k)$. At this time, evaluating minimum cost function can effectively avoid overfitting. It can be seen from equation (8) that when the change of the fuzzy area is small, the value of a_k is close to 0. The filtering at this time is equivalent to a block filter, and the image is relatively smooth. When the fuzzy area changes greatly, the value of a_k is close to 1, which is more favorable for maintaining the edge information of the guide image. The effect of image optimization is mainly as follows: for the image optimized by the digital twin, the original depth of field value in the non-edge area is smooth, while the edge part is consistent with edge information.

3. Realize the Image Texture Feature Extraction Method Based on Digital Twins

The image texture feature structure and segmentation method assume that the texture is composed of precisely defined texture primitives. Because many textures violate this assumption, the application of this method is limited to a great extent. The specific contents of different stages of the method are shown in Figure 2.

It can be seen from Figure 2 that the different stage framework of the image texture feature extraction method is mainly completed by three steps. Step 1 and step 2 belong to the model training process, and step 3 is the recommendation process and visualization. In step 1, the input of the model needs to be determined first. This paper takes the characteristics of the image as the input, so as to build the
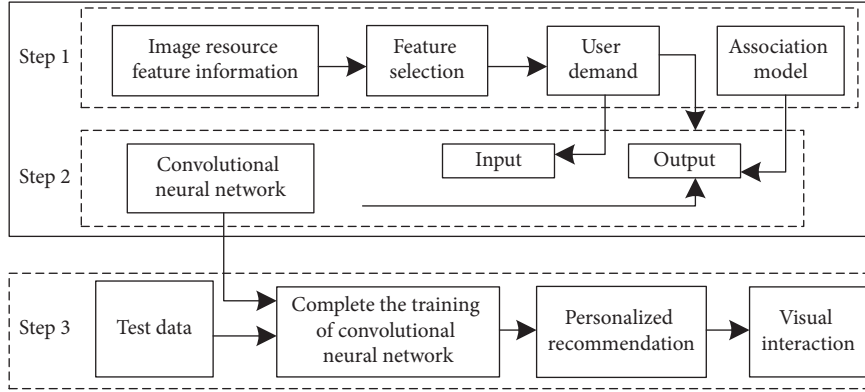
FIGURE 2: Structure diagram of different stages of the image texture feature extraction method.

correlation model between the user and the image, determine whether the image meets the needs of the user, and judge whether the image is recommended; Step 2 is to construct a convolutional neural network model according to the association between the user and the image, and complete the model training; Step 3 is to input the training data into the trained model to complete image texture feature extraction. Image texture feature point detection is to realize the algorithm design and obtain image features; the direction assignment process of image texture feature points is to realize the visualization of the results of image texture feature extraction technology based on the training process.

3.1. Image Texture Feature Point Detection. In the real image texture feature extraction space, the specific position of feature points can be captured reasonably and accurately through interpolation operation. Therefore, it is essential to perform subpixel interpolation on the GSS scale space. The interpolation method based on any function $f(x)$ is as follows:

$$f(x) = M(a_k, b_k) + \frac{\partial f^T}{\partial x}. \tag{9}$$

In formula (9), ∂f^T represents pixel interpolation, and ∂x represents the position vector of the extreme point offset. So far, the feature offset position value of the original image can be obtained. If the value is less than the established threshold, it can be determined that the feature point at this position is unstable and there is abnormal data, which will not be retained as the target feature point. In addition, because feature points at the edge of the image have too many influencing factors and are difficult to extract, it is necessary to set a threshold range first, retain the extreme points of these feature points at the edge within this range, and eliminate these feature points beyond the range to reduce the judgment error.

3.2. Image Texture Feature Point Direction Allocation. According to the above process, after the specific position recognition and detection of feature points, it is necessary to determine the distribution direction of feature points in advance to ensure that there will be no rotation or that it will

not exceed the established range, so as not to affect the subsequent extraction of feature points at edges and inflection points.

When the feature point is at the center of the image, it is necessary to calculate the gradient distribution value of all feature points in all adjacent areas around it, and to take these target points in horizontal and vertical directions to calculate other feature positions in the same direction.

$$M_m(x_i, y_i) = \sqrt{[(x_i, y_i + 1) - (x_i, y_i - 1)]^2}. \tag{10}$$

In formula (10), x_i represents the position of the target feature point in horizontal direction and y_i represents the position of the target feature point in vertical direction. After a wide range of normalization processing, the specific description of the target feature point H can be obtained as follows:

$$H_m = \frac{h_m}{\sqrt{h_n^2}} + M_m(x_i, y_i). \tag{11}$$

In formula (11), h_m represents the size value of image features, and h_n^2 represents the similarity coefficient of image features. Based on this, the positional relationship between edge points and corner points is shown in Figure 3.

Based on the positional relationship in Figure 3, when the image is smoothed and preprocessed, the style attributes of the image are mined to obtain the similarity features of different image styles. The style similarity rules of various types of images are given below, namely,

3.2.1. Consistency Rules. In the same image, the image style is consistent, and there will be no two different image texture features.

3.2.2. Existence Rules. There is a certain similarity between the style of the image H_1 and the image, which can be converted into a similarity coefficient. They belong to the same or different texture features. There is a certain similarity between the styles of the image H_1 and the image H_2, which can be converted into a similarity coefficient. They belong to the same or different texture features. The value of
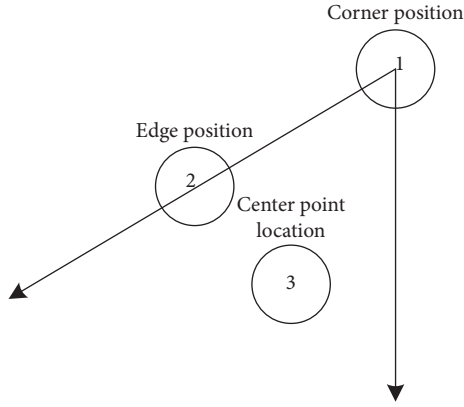
FIGURE 3: Distribution of center point, edge point, and corner point.

FIGURE 4: Fuzzy BP neural network model.

the similarity coefficient is in the $[0, 1]$ interval, where 0 represents no similarity and 1 stands for complete similarity. The setting symbol $R_{\text{simlirity}}$ represents the similarity of two images, namely,

$$K_\alpha = R_{\text{simlirity}}(H_1, H_2). \tag{12}$$

3.2.3. Comparable Rules. The image similarity coefficient of the same category style should be higher than the similarity coefficient. The following measures the characteristic distance function. The specific judgment basis is as follows:

$$\Rightarrow \begin{cases} \begin{cases} L_{\text{label}}(H_1) = L_{\text{label}}(H_2) \\ L_{\text{label}}(H_1) \neq L_{\text{label}}(H_2) \end{cases} \\ \begin{cases} R_{\text{simlirity}}(H_1, H_2) > R_{\text{simlirity}}(H_1, H_3), \\ \Updownarrow, \\ V_{\text{distance}}(H_1, H_2) < V_{\text{distance}}(H_1, H_3). \end{cases} \end{cases} \tag{13}$$

The similarity between the matrix vector and the matrix vector group is calculated by a formula, which is a very common concept. The distance function is mainly used to measure the similarity between matrix vectors and to count the similarity relationship between matrix vectors. The main purpose of image style recognition is to calculate the distance between the vector and the point group. When the distance between them is smaller, it indicates that each matrix vector has high similarity [20]. Through the above rules, assuming that the distance between matrix vectors is lower than any threshold, the vector can be divided into the nearest point group, that is, a category.

3.3. Implementation of Image Texture Feature Extraction Technology. The texture feature extraction of the image is realized, and the fuzzy BP neural network model is established, as shown in Figure 4.

According to the fuzzy BP neural network model shown in Figure 4, the type of input data is analyzed. Because the input data is an image type, the image information is not easy to quantify, and most of it is fuzzy data, so it is necessary to introduce fuzzy sets to process the data, mainly through the analysis and calculation of image data through membership functions, which can divide image information. It is divided into three levels: high, medium, and low, which are used as the three nodes of the input layer. Image information is input through the input layer of the neural network, and the corresponding training and extraction are carried out. When calculating the image information, the fuzzy set is introduced. As the input data of the input layer, each input point needs to be given a corresponding weighting operator, and the value range is within $[0, 1]$. The fuzzy weighting operator is composed of a fuzzy feature membership degree and a feature matrix, which is defined as B, and the composition of the fuzzy weighting operator is specifically defined as $B = \{b_1, b_2, b_3\}$,
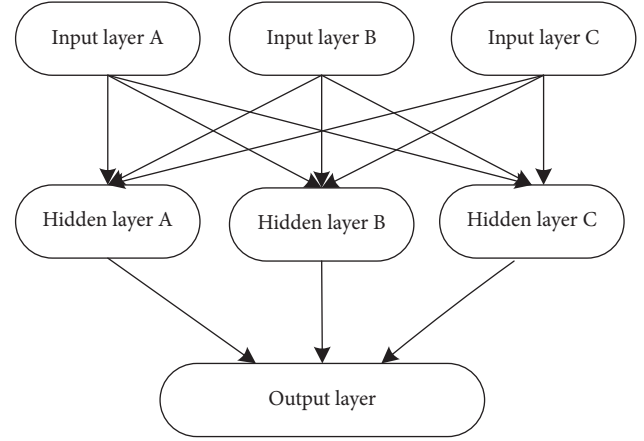
$$B_1 = \frac{b_1}{b_1 + b_2 + b_3} \times A_1, \tag{14}$$

$$B_2 = \frac{b_2}{b_1 + b_2 + b_3} \times A_2, \tag{15}$$

$$B_3 = \frac{b_3}{b_1 + b_2 + b_3} \times A_3. \tag{16}$$

In formulas (14)–(16), the normalized fuzzy feature membership of the image is expressed as B_1, B_2, and B_3, and the corresponding feature matrix is expressed as A_1, A_2, and A_3. The image texture feature membership is calculated, the membership degree of image texture features is calculated, and the feature matrix corresponding to the image is judged through the feature discriminant. When the matrix meets the conditions, it is proved that the matrix has this feature, and the judgment and recording are carried out successively until all of the image texture features are extracted. Finally, the recorded values of features are expressed as b_1, b_2, and b_3.

The main function of the hidden layer is to combine the three results corresponding to the above three nodes, because only one result is needed in the final output layer. In order to solve this problem, the concept of correlation between points is used for combination.

We set the final obtained vector as K, and the corresponding vectors of the three nodes relative to the hidden

TABLE 1: Description of scale interval division.

Name	Source	Data quantity/Piece	Feature category
Characteristic point 1	Scale interval 1	1000	10
Characteristic point 2	Scale interval 2	1000	10
Characteristic point 3	Scale interval 3	1000	10
Characteristic point 4	Scale interval 4	1000	10
Characteristic point 5	Scale interval 5	1000	10
. . .	. . .	—	—
Characteristic point n	Scale interval n	—	—

TABLE 2: Experimental equipment and parameters.

Entry name	Specific parameters
Computer version and model	ASUSx550
Image NetDataset version	3.0.3
CPU	Intel i7-9700K
Memory	516 GB
Operating system	Windows10
Hard disk capacity	120 GB
Data sampling frequency	Collect data every 3 seconds
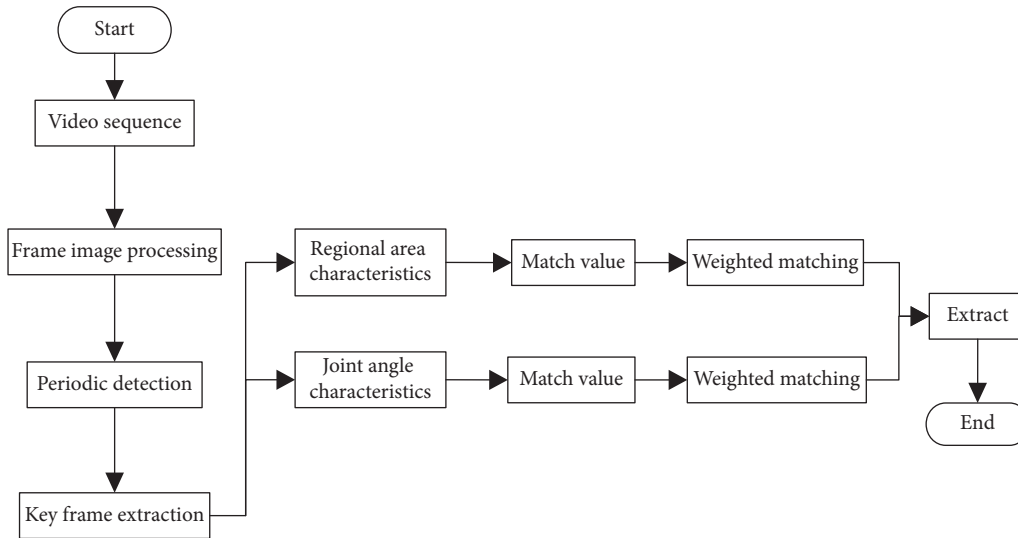
FIGURE 5: Flow chart of image texture feature extraction.

layer are expressed as C_1, C_2, and C_3. The corresponding mean square deviation calculation formula is

$$C^2 = (C - C_1)^2 + (C - C_2)^2 + (C - C_3)^2. \qquad (17)$$

c_1, c_2, and c_3 obtained through formula (17) will be normalized. The three results are normalized to obtain an output result, that is, the extraction result of the feature matrix, so as to complete the research on image texture feature extraction technology based on digital twins.

4. Experimental Analysis

4.1. Experimental Environment. In order to analyze the feasibility of image texture feature extraction technology based on digital twins, experiments were designed to verify it. The experiment adopts the quick bird feature database

with the widest coverage and most types at present. The archived data increase rapidly and have a strong inclusion rate. It is one of the important references of image processing technology at this stage. The selected dataset is from one million audio cover images, the original tree image in the quick bird feature database is used as the test sample for texture feature extraction. The size of the original tree image is 512×512 pixels. In order to ensure the rationality and authenticity of the experiment, methods in reference [6] and reference [7] are compared with methods in this paper. The texture distribution of the image after feature extraction is analyzed, the stability and accuracy of feature extraction are determined, and the excellence of the final experimental effect is obtained. The experiment was divided into two different groups. One group accurately analyzed the extraction of tree texture features, and the other group

FIGURE 6: Original tree image.
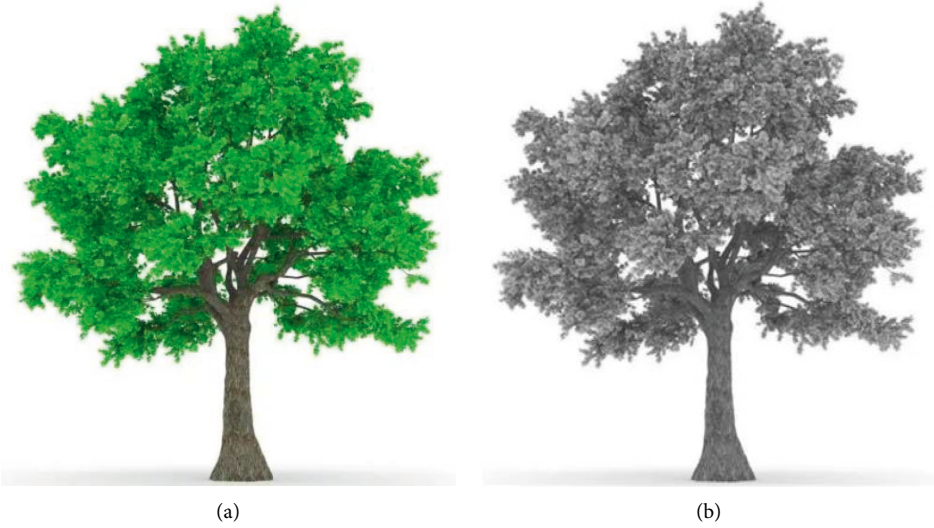
(a)

(b)

(c)

FIGURE 7: Tree texture feature extraction effects. (a) Paper method. (b) Reference [6] method. (c) Reference [7] method.
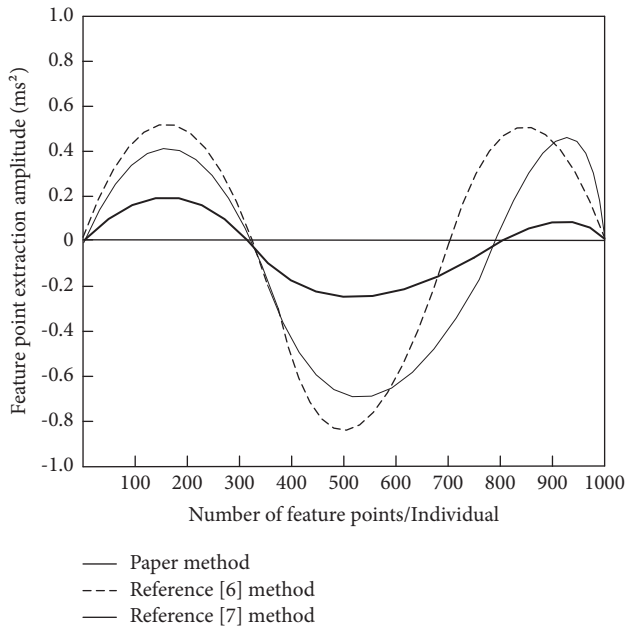
FIGURE 8: Amplitude change results of texture feature extraction of the three methods.

determined the specific loss time of each method through the extraction amplitude of feature points to ensure the comparability of experimental results. Using this method, the experimental data were divided into five different scale intervals to facilitate the feature extraction process. The division of scale intervals is shown in Table 1.

According to the description of scale interval division in Table 1, we set the experimental equipment and detailed parameters. The specific contents are shown in Table 2.

Based on scale interval division description in Table 1 and the experimental equipment and parameters in Table 2, the texture features of the original image were extracted. The specific extraction process is shown in Figure 5.

According to the extraction process in Figure 4, the texture features of the original tree image were extracted. In fact, the original image is shown in Figure 6.

By comparing the texture feature extraction effects of reference [6], reference [7], and this method on the original tree image, an effective conclusion was drawn. The results are shown in Figure 7.

As can be seen from Figure 7, the tree texture feature extraction effect of reference [6] and reference [7] is poor for this method, with low image saturation, blurred overall picture, and a weak sense of boundary. The main reason for this phenomenon is that the abnormal data of the original image were not processed accurately before the feature extraction process, which led to frequent noise in subsequent texture features and affected the experimental results. The overall flatness of the tree texture feature extraction image of our method is high, the capture effect of the tree texture details is good, the tree image is clear, saturation is high, the feature consistency with the original tree image is high, the global tone of the image is mild, and the visual viewing is the best, which shows that the experimental effect of the feature

extraction method in this paper is excellent. It can effectively capture and extract the feature trend without noise or color distortion, and the overall performance is excellent.

By comparing the amplitude and time changes of feature point extraction, the experimental effects of different methods can be accurately analyzed. The variation results of texture feature extraction amplitude of the three methods are shown in Figure 8.

It can be seen from Figure 8 that the amplitude curve extracted from image texture feature points under the methods of reference [6] and reference [7] has been in a state of significant change, and the overall trend is unstable and has strong differences. In contrast, the amplitude curve extracted by this method for image texture feature points has been in a small amplitude fluctuation state, the difference between values is small and the stability is strong, the enhancement range between corresponding nodes is basically the same, and there is no turning point or inflection point, indicating that the feature extraction process of this method has a strong ability to slow down abnormal data. It can effectively remove abnormal data, accurately locate the correct data, and efficiently complete the extraction of target feature points.

To sum up, the image texture feature extraction technology based on the digital twin has a good extraction effect and superior performance.

5. Conclusion and Prospects

The digital twin-based image texture feature extraction technology filters and extracts image feature points. Its innovation is to analyze the intrinsic structural similarity of the image and smooth the image. Based on the optimization of the denoised image through digital twinning, target feature points in the original image are detected, abnormal and split feature points are then eliminated, and the direction of image texture feature points is assigned. It not only solves the problem of unclear feature extraction boundaries caused by noise and abnormal data, but also improves the difficult detection of feature points at edge positions. The experimental results are as follows:

(1) This method has an excellent effect on the surface texture feature extraction of the experimental sample tree.

(2) The designed image texture feature extraction technology based on the digital twin has clear image saturation and stable processing amplitude, which can realize efficient image feature extraction.

(3) Using the designed technology, image texture feature extraction is studied, and some results are obtained.

For texture images in some specific cases, there are still some deficiencies and areas that need to be improved and optimized, mainly as follows:

(1) The existing texture feature extraction methods cannot meet the requirements of practical application, and the classification accuracy is low, which can be further studied in the future.

(2) Most of texture images obtained in practical engineering are wrinkled and distorted textures, rather than having flat regularity, which makes the extraction of texture feature indexes a difficult problem; this can be discussed in depth in the following research.

Data Availability

Data used to support the findings of this study are available from the corresponding author upon request.

Conflicts of Interest

The authors declare that they have no conflicts of interest.

Acknowledgments

References

[1] M. D. B. Abu Hasan, Z. A. B. Ahmad, M. S. Leong, and L. M. Hee, "Automated harmonic signal removal technique using stochastic subspace-based image feature extraction," *Journal of Imaging*, vol. 6, no. 3, 2020.

[2] E. Saad and K. Hirakawa, "Improved photometric acceptance testing in image feature extraction tasks," *Journal of Electronic Imaging*, vol. 29, no. 4, 2020.

[3] N. Wei, "Research on the algorithm of painting image style feature extraction based on intelligent vision," *Future Generation Computer Systems*, vol. 123, no. 24, pp. 196–200, 2021.

[4] A. Chavez-Badiola, A. Flores-Saiffe Farias, G. Mendizabal-Ruiz, R. Garcia-Sanchez, A. J. Drakeley, and J. P. Garcia-Sandoval, "Predicting pregnancy test results after embryo transfer by image feature extraction and analysis using machine learning," *Scientific Reports*, vol. 10, no. 1, 2020.

[5] B. Sugiarto, E. A. Gojali, H. Herlan, and P. Lestari, "A smartphone-based of wood identification using image feature extraction," *Journal of Computer Science and Informatics Engineering (J-Cosine)*, vol. 4, no. 1, pp. 9–15, 2020.

[6] F. Tarsitano, C. Bruderer, K. Schawinski, and W. G. Hartley, "Image feature extraction and galaxy classification: a novel and efficient approach with automated machine learning," *Astrophysics of Galaxies*, vol. 3, no. 5, pp. 1–9, 2021.

[7] S. Kumar, J. Pradhan, and A. K. Pal, "Adaptive tetrolet based color, texture and shape feature extraction for content-based image retrieval application," *Multimedia Tools and Applications*, vol. 80, no. 19, Article ID 29017, 2021.

[8] S. Hamad Khaleefah, S. A Mostafa, A. Mustapha, and M. Faidzul Nasrudin, "Review of local binary pattern operators in image feature extraction," *Indonesian Journal of Electrical Engineering and Computer Science*, vol. 19, no. 1, 2020.

[9] R. Sun, J. Qian, R. H. Jose et al., "A flexible and efficient real-time orb-based full-hd image feature extraction accelerator," *IEEE Transactions on Very Large Scale Integration Systems*, vol. 28, no. 2, pp. 565–575, 2020.

[10] R. Tamilkodi and G. R. Nesakumari, "Image retrieval system based on multi feature extraction and its performance assessment," *International Journal of Information Technology*, vol. 14, no. 2, pp. 1161–1173, 2021.

[11] X. Zheng, Y. Tao, R. Zhang, W. Yang, and Q. Liao, "TimNet: a text-image matching network integrating multi-stage feature extraction with multi-scale metrics," *Neurocomputing*, vol. 465, no. 20, pp. 540–548, 2021.

[12] C. Tyab, C. Jma, B. Yma et al., "Privacy-preserving Krawtchouk moment feature extraction over encrypted image data," *Information Sciences*, sciencedirect, vol. 536, no. 10, pp. 244–262, 2020.

[13] C. Hernández-Aguayo, F. Prada, C. M. Baugh, and A. Klypin, "Building a digital twin of a luminous red galaxy spectroscopic survey: galaxy properties and clustering covariance," *Monthly Notices of the Royal Astronomical Society*, vol. 503, no. 2, pp. 2318–2339, 2021.

[14] V. H. Nguyen, Q. T. Tran, T. Tran-Quoc, T. L. Nguyen, and M. Jung, "Digital twin integrated power-hardware-in-the-loop for the assessment of distributed renewable energy resources," *Electrical Engineering*, vol. 104, no. 2, pp. 377–388, 2021.

[15] F. Jiang, Y. Ding, Y. Song, F. Geng, and Z. Wang, "Digital twin-driven framework for fatigue life prediction of steel bridges using a probabilistic multiscale model: application to segmental orthotropic steel deck specimen," *Engineering Structures*, vol. 241, no. 15, Article ID 112461, 2021.

[16] J. Vrana, "The core of the fourth revolutions: industrial internet of things, digital twin, and cyber-physical loops," *Journal of Nondestructive Evaluation*, vol. 40, no. 2, 2021.

[17] T. I. Zohdi, "A digital-twin and machine-learning framework for the design of multiobjective agrophotovoltaic solar farms," *Computational Mechanics*, vol. 68, no. 2, pp. 357–370, 2021.

[18] L. M. Yan, Y. Y. Ge, and L. Shi, "Simulation of image encryption algorithm based on chaotic map and stream cipher," *Computer Simulation*, vol. 37, no. 3, pp. 264–269, 2020.

[19] P. Zheng, D. Qin, B. Han, L. Ma, and T. M. Berhane, "Research on feature extraction method of indoor visual positioning image based on area division of foreground and background," *ISPRS International Journal of Geo-Information*, vol. 10, no. 6, 2021.

[20] K. Saeed, S. Datta, and N. Chaki, "A granular level feature extraction approach to construct hr image for forensic biometrics using small training dataset," *IEEE Access*, vol. 8, no. 6, Article ID 123556, 2020.

Research Article

Integrated Design of College English Teaching Based on Internet and Information Technology

Hongtao Zhang (ID),[1] **Cheng Zhu** (ID),[2] **and Na He**[3]

[1]*School of Foreign Studies, Henan Polytechnic University, Jiaozuo, Henan 454000, China*
[2]*College of Architectural Engineeing, Jiaxing Nanhu University, Jiaxing, Zhejiang 314001, China*
[3]*GongQing Institute of Science and Technology, Gongqingchengshi, Jiangxi 332020, China*

Correspondence should be addressed to Cheng Zhu; 10460150130@hpu.edu.cn

The rapid development of information technology has brought society into the Internet + era. To break the current teaching dilemma, English teaching in colleges and universities needs to keep pace with the times. Based on the characteristics of the Internet + era, we need to strengthen the awareness of the Internet + era and reconstruct the resource advantages and technological advantages of the Internet + era. The English teaching mode in colleges and universities rejuvenates college English teaching, establishes a mode suitable for English teaching in the new era, and comprehensively improves the effectiveness of college English teaching. This research optimizes the teaching design under the guidance of the Internet and information technology and the concept of curriculum integration and applies it to the teaching practice of a college English listening and speaking course. Design-based research is used as the main research method. Under the guidance of the concept of information technology and curriculum integration, first of all, we measure and evaluate the TPACK level informatization teaching ability of English teachers in colleges and universities. Secondly, we design and optimize the whole process of teaching, especially the design and adjustment of teaching procedures. Finally, the research conclusions are obtained through statistical analysis of the data. It is found that the teaching optimization design under the guidance of the concept of information technology and curriculum integration can improve the English listening and speaking ability of college students to a certain extent.

1. Introduction

"Internet +" is a new model under the social background that vigorously advocates innovation. This model focuses on using the characteristics of the Internet to optimize and integrate the economic production process, allocate production factors more benignly, and use the innovation factors of the Internet to drive the traditional economy [1–3]. Industrial innovation promotes the continuous progress of the social economy and enhances the productivity and creativity of my country's real economy. The Internet is used as an excellent platform to complete industrial upgrading. Under the current educational model of colleges and universities, classroom teaching is still dominated by teachers. Most of the time, teachers impart course

knowledge to students through presentations and dictation on the podium. This teaching method is extremely closed, and the content is limited to the scope of the textbook, lacking novelty, and attractiveness [4–6]. The professor's knowledge is very boring, and the students are not willing to accept it, resulting in unsatisfactory teaching quality. In classroom teaching, it is sometimes difficult for teachers to take into account students with uneven foundations. For students with a good foundation, this kind of classroom teaching cannot meet the learning needs of such students, and students are prone to feeling bored; for students with a poor foundation, they do not understand the content of the teacher's teaching, and they are also unfamiliar with the teaching generating resistance [7]. In addition, students in the classroom carry smartphones with them, and they just

bow their heads and indulge in the entertainment of mobile phones in class, which reduces the efficiency of classroom teaching. Outside of classroom teaching, students do not have the atmosphere and environment to learn English, and they cannot carry out effective self-study. At present, English teaching lacks a good English learning environment, and the English teaching mode in colleges and universities is also behind the times and students' needs. Therefore, it is necessary to explore a new teaching mode to change this situation [8–10].

Based on the domestic and foreign research trends and paths based on the concept of information technology and curriculum integration, exploring the integration of information technology and specific subject content and guiding and optimizing teaching design has formed a certain research trend, and has a certain role and impact on teaching [11–13]. Because teaching design is the core link of teaching, it is also the premise and foundation for teachers to teach effectively. Therefore, teachers should improve teaching based on teaching design, cultivate and develop their own knowledge creation and design capabilities; that is, teachers can be proficient, creative, and design integrated courses tailored to local conditions according to the actual teaching situation. At present, the research trend and path of the concept of information technology and curriculum integration turn to the micro to solve the practical problems of teaching. However, there are still some problems and limitations in domestic research [14–16]. For example, relevant domestic research focuses on pre-service, primary, and secondary school teaching, while research on college teaching has not been widely popularized and deepened. In actual teaching, the integration of information technology and specific subject content is not ideal, and there is a lack of teaching practice with deep integration. Relevant research shows that teachers should plan and design courses that integrate technology, that is, to apply the concept of information technology and course integration to optimize teaching design to improve teaching effects and promote student learning.

Under the guidance of the integration of information technology and curriculum, this research aims to improve the English language listening and speaking ability of college students through the teaching optimization design of the English listening and speaking course in a college [17–19]. In terms of theory, this research draws on the advantages of the teaching design of English listening and speaking courses in the college, removes shortcomings, optimizes teaching by applying the concept of information technology and curriculum integration, and follows the teacher-led-student-subject teaching and learning theory and Butler's theory. The transcendental teaching theory and teaching procedure provide new ideas and directions for the teaching design of English listening and speaking courses in the college.

2. Methods

First of all, in the early stage of the research, we observed the teaching dimension of a college English listening and speaking course. The observation period is four sections of English courses in colleges and universities, and each section is 45 minutes in total for two weeks. Then, an interview survey is conducted with the main teachers of English listening and speaking courses in colleges and universities. Finally, we design and optimize the English listening and speaking courses in colleges and universities, and carry out research and design from the main dimensions of teaching objectives, learning situation analysis, teaching media and course materials, teaching content, teaching procedures, and teaching evaluation. Finally, we focus on the detailed design and analysis of the program of English listening and speaking courses in colleges and universities.

2.1. Observation Method. We obtain a large number of direct perceptual research materials with field observation research methods. We mainly observe the teaching design dimensions of English listening and speaking courses in the college, the application of technical tools, and the integration of technology and course content. We record, organize, and analyze the acquired teaching research materials.

2.2. Interview Method. In this study, the systematic interview method is used to investigate and analyze the English teachers in colleges and universities to obtain the TPACK level, the ability of informatization teaching, the overall situation of the teaching design of English listening and speaking courses, and the actual situation of teaching and learning situation of students.

2.3. Questionnaire Survey Method. We use the form of questionnaire to investigate and analyze the actual situation of English listening and speaking courses in the college and students' learning situation. The questionnaire is designed to analyze the basic situation and characteristics of the students. The research object is a total of 50 freshmen who majored in management in 2021. Among them, there are 27 boys and 23 girls. Through the results of the previous questionnaire survey, it is found that the students' English foundation is weak. Although the public English audio-visual course does not require high English professional level of the students, there are still some difficulties and problems in the practical English section. Among them, students feel unfamiliar with the learning of the English language and culture dimensions, which exceeds the cognitive load of some freshmen. The likert five-point scale is used as a survey and evaluation tool to analyze and evaluate the English listening and speaking ability of college students. The questionnaire design includes five options: strongly agree, agree, moderate, disagree, and strongly disagree. There are 60 items of research questions, including 30 items for English language listening comprehension ability and 30 items for English language oral expression ability. A total of 50 students participate and respond. Through preliminary screening, the data of these responses are screened, and the data fed back are true and reliable.

2.4. Integrated Design Scheme

2.4.1. Set the Context.
English teaching topics and related concepts are introduced through video or PPT technology tools. Among them, the setting methods of situations are flexible and diverse, and the setting methods of teaching situations mainly include the following five methods:

(1) The popular English original music pieces are introduced into the course by video not only to reveal the multielement cultural characteristics of the course but also deepen the students' perceptual understanding.

(2) We bring it into the course in the form of a mind map, and students make a simple overview of the knowledge chain according to the mind map in the PPT. Through different ways of understanding the mind map of PPT, we can do a small oral presentation in English and infer the main content and cultural factors of the course. The mind map in PPT is an abbreviated impression of the course, which allows students to use their imagination and bring them into the specific situation of the course.

(3) We introduce language and cultural phenomena in the course content by video. After watching, we can arouse students' curiosity and interest, inspire students to brainstorm, and analyze and discuss language and cultural phenomena in small groups. If the learning atmosphere is good, there will be debates between groups, which will lead to students' in-depth thinking and heuristic teaching.

(4) We introduce famous sayings and aphorisms of course, culture or viewpoint topics with culture shock through PPT courseware to trigger students to think. And give students 5 minutes to prepare a small speech to make a supporting or arguing statement on the topic. This kind of situational setting method can help to develop students' ability to summarize ideas in English learning and to cultivate the English language and culture.

(5) The main content of the course is divided into role imitation and acting. Through PPT video playback, students can take the initiative to perform and imitate their favorite roles under the condition of preparation in advance. Group performance can stimulate a good teaching atmosphere, mobilize the enthusiasm of students in English learning, and enhance students' interest in learning.

2.4.2. Excite the Engine.
Through technical tools and heuristic teaching methods, questions related to the teaching theme of English courses are raised to trigger students' learning and thinking. The way to stimulate students' motivation and interest in learning is to use technology tools as a guide and to combine teaching methods familiar to teachers. There are mainly two teaching strategies and methods involved:

(1) After the teaching situation is introduced, the teacher will use PPT to ask the students about the actual problems encountered in the actual life or social practice of the students, and the students will think or imagine this unknown or preset problem. Because the questions included in the course are closely related to the students' study and life, it stimulates students' active learning and positive thinking to a large extent, and they are interested and curious about the course. Teachers' preset questions can be structured or semistructured to evoke positive responses and full thinking in students' learning.

(2) The media equipment is used to play the English original sound film clip for 3–5 minutes. The original sound film clip is closely related to the course and can arouse students' motivation and interest in learning. After playing, students will be inspired to ask questions about the theme and content of the English film and inform them of this. The content of English movies is closely related to the curriculum, arousing students' motivation, interest, and awareness of learning.

2.4.3. Teaching New Knowledge.
The teaching method is applied to the teaching of the main English knowledge, and questions and corrections are made in a timely manner. Teachers use concise and incisive methods to teach the main knowledge of the course in a short time, deepen new knowledge with video and PPT, and ask students to get feedback in a timely manner. Then, heuristic teaching is carried out. The voice system is used to ask the main questions of knowledge and inspire students' wisdom and interest. The speed and accuracy of knowledge feedback are mainly measured by means of knowledge competition. This link can highlight the leading role of teachers in teaching. At the same time, the subject view of students has also received attention. The application of the teacher's teaching method makes the students' teaching knowledge more systematic and complete, instead of being separated from the fragmented and fragmented state.

2.4.4. Apply New Knowledge.
The teachers encourage students to apply their new English knowledge to complete the set learning tasks in the class. In teaching, there are three main types of strategies for using new knowledge:

(1) The teachers play the relevant videos of the course materials, and students will state and dub the specific learning content played by the courseware. During the presentation or dubbing, the microvideo is muted and only framed in images. Students tell the story of the courseware based on what they have learned, narrate the predetermined content of the courseware, and explain the learning and social life phenomena reflected in the video.

(2) The teachers play relevant audio of the course material. The types of audio files are English soundtrack movies, classic plays, songs, and other art forms. The

frequency of playback is 3–5 times, and students dictate vocabulary and paragraphs according to the information contained in the audio. After completing the learning task, the students share it with peers or group members, and the teacher will give instant evaluation.

(3) The teachers can apply the new knowledge by applying role-play according to the course materials. Students can prepare in less than 5 minutes in a collaborative manner with peers or group members. Then, in the form of a random check group, they go to the podium to role-play and simulate the content of the course materials. Finally, the teacher evaluates and summarizes.

3. Results and Discussion

In this study, a comparative experiment is adopted, and a total of 50 students are selected as the research sample. Among them, 27 are boys and 23 are girls. In order to ensure the scientificity and accuracy of the research experiments, a scientific front-side questionnaire was conducted before the implementation of this study. 50 questionnaires are distributed and 50 questionnaires are returned. The response rate of the questionnaire is 100%, and the effective rate is 100%. The front-side questionnaire includes a total of 60 items. Among them, there are 30 items for the English oral expression test and 30 items for the English listening comprehension test.

After the research and implementation, the Chinese English Language Listening and Speaking Ability Revised Scale is used as a measuring tool to evaluate the English listening and speaking ability of college students in the early stage, and the research data are obtained through sample analysis. Among them, there are three stages of data collection, which last for three months, namely initial data in the early stage, experimental data in the middle stage, and experimental data in the later stage. The changes in the three sets of experimental data are compared to obtain the research results. Using the data software SPSS22.0 as data statistics and analysis tool, we measure and evaluate whether the English listening and speaking ability of the college students has been improved in the early, middle, and late stage.

First of all, this study uses descriptive statistical analysis and then conducts paired T-test on the research papers. Based on the results of data statistics and analysis, it is used to verify whether the English listening and speaking ability of the college students has been improved in the early, middle, and late stages of the study.

According to the results of descriptive statistical analysis on the research data of the college students, as shown in Table 1, the average value of the early stage is $M = 2.8698$. Among them, the maximum value is 3.1265, and the minimum value is 2.6416. On the whole, the English listening and speaking ability of the students in this college is slightly worse, which is lower than the critical value of 3.0 and needs to be improved.

After a month of research and implementation of English listening and speaking courses in the colleges, a teaching questionnaire survey is conducted on the college students in the middle stage of the study. Through the design, distribution and recovery of student questionnaires in the middle stage of the study and the middle stage data statistics and analysis on the English listening and speaking ability of S college students are carried out. Then, we obtain the overall evaluation and feedback on the teaching activity design by the students of the college and make teaching adjustments in a timely manner.

First, in the middle stage of the study, a total of 50 research papers are distributed and recovered, with a recovery rate and an effective rate of 100%. A descriptive statistical analysis is carried out on the interim research data of the college students. As shown in Table 2, the mean value of the sample M is 2.961, among them, the maximum value is 3.2495, and the minimum value is 2.7896. On the whole, after the implementation of the research, the English listening and speaking ability of college students has not been significantly improved, and it is still lower than the critical value of 3.0, which shows that the research has problems in the teaching procedures in the process of designing teaching activities.

Secondly, by doing research on the students of S colleges and through the statistics and analysis of the questionnaires, it is found that in the process of teaching activities, the students' preferences and acceptance of the teaching forms set in the teaching situation are not the same. Finally, the teaching adjustment in the middle of the research is carried out. According to the students' learning needs and interests, video dubbing and role-playing are used as the main situation setting methods, which improve students' enthusiasm and initiative in learning. The teaching adjustment in the middle of the study is in line with the students' learning needs and interests.

In the late stage of the study, descriptive statistical analysis and paired research T-test are carried out on the back side of college students. A total of 50 questionnaires are distributed. Among them, the recovery rate and the effective rate are 100%. As shown in Table 3, the sample mean M is 3.2456, the maximum value is 3.5965, and the minimum value is 2.9255. On the whole, after the research and practice, the English listening and speaking ability of the college students has been improved to a certain extent, which is slightly higher than the critical value of 3.0. This shows that the research has achieved research results.

The English listening and speaking ability of the college students have a tendency to improve. From the early stage, middle stage to late stage, there is a certain degree of improvement in the maximum value (maximum value, minimum value). From the point of view of the mean value, the scores of listening and speaking ability of college students in the early, middle, and late stages of the study range from 2.8698 to 3.2456, and the standard deviation and variance are within a reasonable range. It shows that the students' English listening and speaking ability has been improved.

In the end, the research obtained data results through data statistics and analysis in the early, middle, and late stages (Figures 1, 2).

Table 1: Descriptive statistical analysis of the English listening and speaking ability of students in a college in the early stage.

	N	Minimum	Maximum	Average	Standard deviation
English listening and speaking ability of college students in the early stage	50	2.6416	3.1265	2.8698	0.029
Valid N	50				

Table 2: Descriptive statistical analysis of English listening and speaking ability of middle stage college students.

	N	Minimum	Maximum	Average	Standard deviation
English listening and speaking ability of college students in the middle stage	50	2.7896	3.2495	2.9610	0.038
Valid N	50				

Table 3: Descriptive statistical analysis of English listening and speaking ability of students in late stage.

	N	Minimum	Maximum	Average	Standard deviation
English listening and speaking ability of college students in the late stage	50	2.9255	3.5865	3.2456	0.054
Valid N	50				
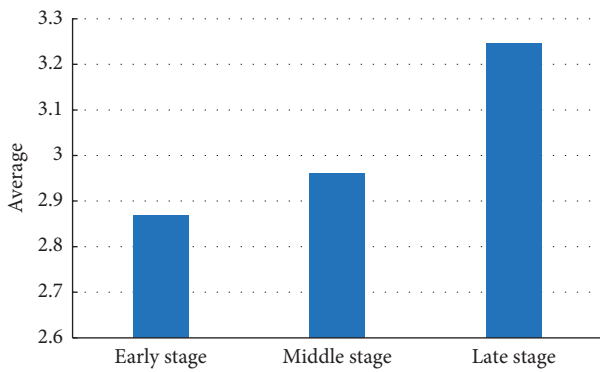
Figure 1: Paired sample statistics.
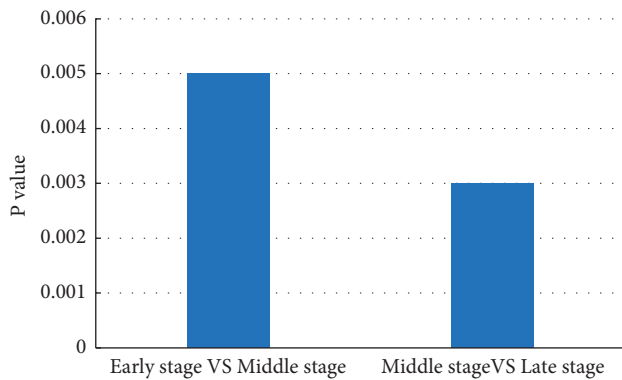
Figure 2: Sample correlation analysis.

It can be seen that the accompanying probability of the F test is that the Sig value is less than a significant 0.05. It is proved that there are significant differences in the variance of students' English listening and speaking ability in the early stage and the middle stage, and the middle stage and the later stage; that is, the variance is uneven. The significance probability P of the two-sided test is less than 0.05, and the null hypothesis is rejected, indicating that there are significant differences in the level of English language listening and speaking ability in the early stage and the middle stage, and the middle stage and the later stage. The English language listening and speaking ability level in the late stage is better than that in the early stage.

4. Conclusion

(1) The teaching practice under the guidance of the concept of information technology and curriculum integration has optimized and improved the English teaching in colleges in the early stage, produced good teaching effects and improved the English listening and speaking ability of college students. At the same time, it provides an important reference for the design and practice of English listening and speaking courses in colleges in the future.

(2) The results show that the curriculum design of college English teaching from the perspective of technology and curriculum integration can effectively improve college students' English listening and speaking ability. The longer the learning time, the better the effect.

(3) After a month of research and implementation of English listening and speaking courses in the colleges, a teaching questionnaire survey is conducted on the college students in the middle stage of the study. Through the design, distribution and recovery of student questionnaires in the middle stage of the study, and the middle stage data statistics and analysis on the English listening and speaking ability of S college students are carried out. Then, we obtain the overall evaluation and feedback on the teaching activity design by the students of the college and make teaching adjustments in a timely manner.

Data Availability

The figures and tables used to support the findings of this study are included in the article.

Conflicts of Interest

The authors declare that they have no conflicts of interest.

Acknowledgments

References

[1] P. DiMaggio, E. Hargittai, W. R. Neuman, and J. P. Robinson, "Social implications of the internet," *Annual Review of Sociology*, vol. 27, no. 1, pp. 307–336, 2001.

[2] K. A. Marrs and G. Novak, "Just-in-time teaching in biology: creating an active learner classroom using the internet," *Cell Biology Education*, vol. 3, no. 1, pp. 49–61, 2004.

[3] R. M. Wallace, "A framework for understanding teaching with the Internet," *American Educational Research Journal*, vol. 41, no. 2, pp. 447–488, 2004.

[4] Y. Sun and F. Gao, "An investigation of the influence of intrinsic motivation on students' intention to use mobile devices in language learning," *Educational Technology Research & Development*, vol. 68, no. 3, pp. 1181–1198, 2020.

[5] J. Zhang, "College English curriculum group: the construction based on needs analysis," *English Language Teaching*, vol. 11, no. 6, pp. 80–85, 2018.

[6] G. S. Alaghbary, "Integrating technology with Bloom's revised taxonomy: web 2.0-enabled learning designs for online learning," *Asian EFL Journal*, vol. 28, no. 1, pp. 10–37, 2021.

[7] S. C. Yang and Y.-F. Huang, "A study of high school English teachers' behavior, concerns and beliefs in integrating information technology into English instruction," *Computers in Human Behavior*, vol. 24, no. 3, pp. 1085–1103, 2008.

[8] M. M. Elaish, L. Shuib, N. A. Ghani, and E. Yadegaridehkordi, "Mobile English language learning (MELL): a literature review," *Educational Review*, vol. 71, no. 2, pp. 257–276, 2019.

[9] N. D. Linh and S. Suppasetseree, "The development of an instructional design model on facebook based collaborative learning to enhance EFL students' writing skills," *IAFOR Journal of Language Learning*, vol. 2, no. 1, pp. 48–66, 2016.

[10] O. Hassanein, "E-learning instructional design and the mismatch between e-learners and e-educators learning styles," *International Journal on E-Learning*, vol. 14, no. 1, pp. 5–28, 2015.

[11] K. Rao and A. Tanners, "Curb cuts in cyberspace: universal instructional design for online courses," *Journal of Postsecondary Education and Disability*, vol. 24, no. 3, pp. 211–229, 2011.

[12] S. Ismail, "An analysis on learning condition in developing of listening comprehension model by using social media for English students," *J-SHMIC: Journal of English for Academic*, vol. 7, no. 1, pp. 33–42, 2020.

[13] M. Alavi and D. E. Leidner, "Research commentary: technology-mediated learning-A call for greater depth and breadth of research," *Information Systems Research*, vol. 12, no. 1, pp. 1–10, 2001.

[14] G.-Z. Liu, G.-J. Hwang, Y.-L. Kuo, and C.-Y. Lee, "Designing dynamic English: a creative reading system in a context-aware fitness centre using a smart phone and QR codes," *Digital Creativity*, vol. 25, no. 2, pp. 169–186, 2014.

[15] H.-T. Hung, "Flipping the classroom for English language learners to foster active learning," *Computer Assisted Language Learning*, vol. 28, no. 1, pp. 81–96, 2015.

[16] Y. Zhang, "Project-based learning in Chinese college English listening and speaking course: from theory to practice," *Canadian Social Science*, vol. 11, no. 9, pp. 40–44, 2015.

[17] A. Kukulska-Hulme, "Will mobile learning change language learning?" *ReCALL*, vol. 21, no. 2, pp. 157–165, 2009.

[18] F. Rosell-Aguilar, "Top of the pods-in search of a podcasting "p" for language learning," *Computer Assisted Language Learning*, vol. 20, no. 5, pp. 471–492, 2007.

[19] W. L. Shang, "Application of machine learning and internet of things techniques in evaluation of English teaching effect in colleges," *Computational Intelligence and Neuroscience*, vol. 2022, Article ID 7643006, 9 pages, 2022.

Research Article

Vibration and Constitutive Relations of Viscoelastic Cantilever Beam of HTPB Propellant

Bo Gao [ID] and Zhuo Li

College of Science, Inner Mongolia University of Technology, Hohhot 010051, China

Correspondence should be addressed to Bo Gao; 20181000007@imut.edu.cn

A cantilever beam test specimen of a viscoelastic material, which is sourced from the hydroxy-terminated polybutadiene (HTPB) propellant, has been made. The traditional experimental modal analysis (EMA) is performed using the SIEMENS TESTLAB software to obtain the first six orders of modal frequencies based on the Poly MAX method, thereby determining the frequency range associated with the frequency domain analysis. The relaxation modulus of this viscoelastic material is first measured using a thermo-viscoelasticity analyzer (DMA); subsequently, the relaxation modulus is adopted to fit the 19-parameter Prony series of conformational models that characterize this viscoelastic material. Sinusoidal frequency sweep is then conducted on the SIEMENS TESTLAB platform, and the corresponding measured signals are obtained. Using the finite element method, a transient analysis simulation of the experimental conditions is performed. The dynamic response of this viscoelastic material under sinusoidal frequency sweep is evaluated by comparing it with the experimental data. It is observed that the overall acceleration peak error and the finite element simulation result are less than 3%. This study verifies that the obtained static constitutive equation (19-parameter Prony series) can describe the dynamic responses at low frequencies (<80 Hz).

1. Introduction

The propellant grain of a solid rocket motor is regarded as a typical viscoelastic material. When viscoelastic materials are subjected to simple loading conditions, the subsequent deformation process changes with time and the recovery process after unloading is delayed. Therefore, the stress in such a material is not only related to the strain at that time but also to the entire change history of strain. During the recovery process, the one-to-one correspondence between stress and strain no longer exists, and the material undergoes creep and relaxation. Therefore, elucidating the creep or relaxation function of a viscoelastic material has become an important tool to describe its model parameters [1], which is also software friendly. Hui et al. studied the fitting of the shear relaxation modulus function of viscoelastic materials, while exploring the relaxation modulus of a viscoelastic prototype based on Maxwell model [2]. Xu et al. put forward a data fitting method according to a Prony series based on

the static tension relaxation experiment and linear viscoelasticity; subsequently, they implemented isokinetic stretching and the relaxation experiment to assess their method [3]. This method also works very well in finite elements. Miller et al. used the conventional method of testing the propellant under uniaxial tension, and the double cantilever beam mode was used to test the propellant in a thermo-viscoelasticity analyzer (DMA); they proved that when the results of the two methods were similar, DMA required less materials, exhibited lower variability, and showed insensitivity to the applied strain [4, 5]. He used the finite element method to simulate and analyze the two-dimensional axial deformation of viscoelastic components, the influence of the viscoelasticity of the material on the model, and viscoelastic behaviors under cyclic loading [6, 7]. A finite element model of asphalt pavements consisting of the Burgers model is presented, where the HTPB propellant was modeled as a viscoelastic material in finite element simulations [8]. Wang adopted the finite element method to study

the viscoelastic responses of buried pipe-type conductive asphalt pavements under moving loads; they implemented a method to convert the constitutive model of viscoelasticity of asphalt mixtures into a Prony series [9, 10]. Zhao et al. calculated the unit response equations associated with three kinds of responses of typical asphalt pavement structures; subsequently, they analyzed the viscoelastic responses of the pavement structure under a semisinusoidal pulse load by using Boltzmann superposition principle [11]. The influence of driving speed on three kinds of viscoelastic responses was also determined. The study indicated that the unit response equation could be accurately expressed by a Prony series, and its parameters could be determined using a configuration method. Wang and Zhang derived the viscoelastic integral-type incremental constitutive equation and its recursive formula (expressed by Kirchhoff stress and Green strain) using a Prony series, thereby proposing a finite element incremental superposition method for calculating the dynamic response to a 3D viscoelastic deformation [12]. Yuan and Sun derived the viscoelasticity constitutive equation of resin (expressed by a Prony series) and set the component material parameters of the model [13]. Shi et al. established the viscoelasticity constitutive model of a Kelvin-like body, which was compared with the classical Prony series model [14, 15].

In service, hydroxy-terminated polybutadiene (HTPB) is subjected to dynamic loading caused by flight and transportation vibrations as well as other environments [16]. It is quite important to determine the short-term and long-term adverse effects of these vibrations on the propellant. Baqersad et al. analyzed the characteristics of vibration response under random excitation [17]. The neural network was adopted to predict the displacement response, and the interval modeling technique was used to construct the damage index. The damage time was determined, and the cantilever beam model was simulated [18]. Zhu and Deng conducted the dynamic response analysis of the cantilever beam with cracks by using the finite element method, and the life of the structure was analyzed [19]. In addition, many scholars have also done a lot of research on solid pellets of HTPB [20–23].

The previous research only studied mechanical properties under static or dynamic conditions, and there were relatively few research studies on the combination of static and dynamic. In the past, the dynamic model of HTPB propellant was very dependent on frequency (including high and low frequencies), so it was difficult to obtain an accurate dynamic model. The fundamental frequency of a solid rocket motor plays a very important role in all vibration frequencies. The fundamental frequency of a solid rocket motor is generally around 80 Hz, so it is very meaningful to study the vibration at low frequencies. This study focuses on the application of the static model of HTPB propellant to the dynamic response at low frequencies, combined with the accuracy of the dynamic model, and avoids the cumbersome acquisition of the dynamic model. The study starts from the basic theory of viscoelasticity and expresses the relaxation modulus as a Prony series to determine the constitutive equation of this viscoelastic material. Then, a sine sweep
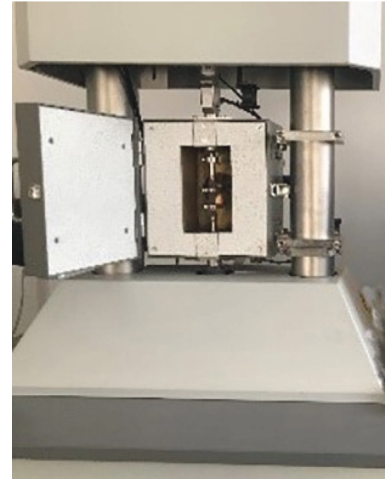
Figure 1: Advanced dynamic thermomechanical analyzer (DMA).

frequency excitation was conducted to verify that this constitutive equation can be applied in the low-frequency dynamic response.

2. Constitutive Equation

2.1. Equipment for the Relaxation Experiment. An advanced dynamic thermomechanical analyzer (EPLEXOR8) developed by German GABO has been used in this study, as shown in Figure 1. The instrument is equipped with two upper and lower driving systems, and the static and dynamic forces are provided by two independent systems. The instrument exhibits a good driving control ability and accuracy, while the test data demonstrate satisfactory repeatability.

2.2. Sample Preparation and Experimental Method. The viscoelastic material is sourced from the HTPB propellant (butyl propellant), which is composed of 68% ammonium perchlorate (AP), 11.3% hydroxy-terminated butadiene (HTPB), 17% aluminum powder (Al), and small amounts of curing agent, plasticizer, and process additive; AP, HTPB, and Al function as an oxidizer, an adhesive, and a metal combustion agent, respectively. The HTPB propellant is one of the commonly used solid propellants in rocket weapons.

This paper obtained the HTPB propellant from China Aerospace Science and Industry Group Sixth Research Institute, as shown in Figure 2. More than eighteen specimens with dimensions of $1.5 \, mm \times 3.5 \, mm \times 7.5 \, mm$ are obtained using a special cutter. Three specimens for each temperature. According to the Aerospace Industry Standard of the Ministry of Aeronautics and Astronautics of the People's Republic of China QJ2487-93 [24], the tensile experiments at rate of 500 mm/min and the relaxation modulus are calculated using a DMA since the DMA calculated the relaxation modulus using the measured data, as shown in equation (1). Accordingly, the constitutive model of viscoelasticity, which is characterized by the relaxation modulus, has been established. This study adopts the constitutive equation acquisition method according to the Aerospace
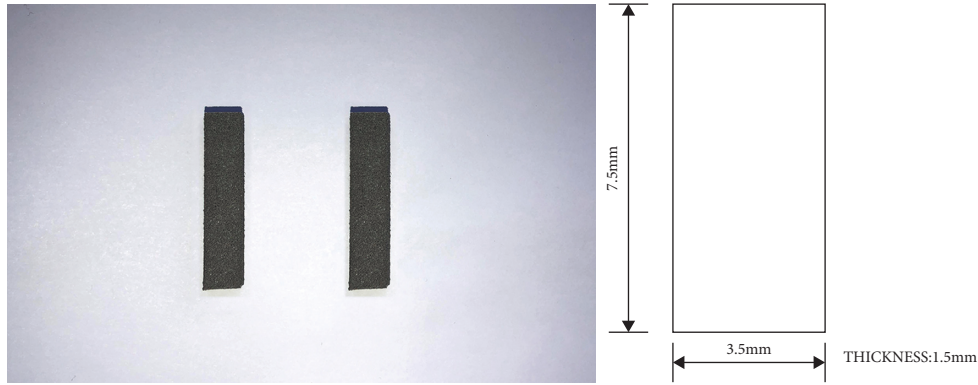
FIGURE 2: Experiment specimens.

TABLE 1: Relaxation modulus test conditions.

Temperature (°C)	Stretching speed (mm/min)	Initial constant strain (%)	Preload (N)	Relaxation sampling time (s)
−40, −20, 0, 20, 40, 70	500	5	2	2, 4, 8, 20, 40, 80, 120, 200, 400, 600, 1000

Industry Standard of the Ministry of Aeronautics and Astronautics of the People's Republic of China QJ2487-93. Under the working conditions of solid engine transportation and storage, the temperature range it is subjected to is about −40 to 70°C [25, 26]. Therefore, in case of any discrepancy, the experimental conditions can be considered accountable.where $E(t)$ is the stress relaxation modulus at moment (t) (MPa), $F(t)$ is the relaxation force at moment t (N), ε_0 is the initial constant strain (%), and A_0 is the specimen initial cross-sectional area (mm^2).

After the experiment is carried out according to Table 1 and calculations are performed using equation (1), the results are obtained and represented in Table 2.

$$E(t) = \frac{F(t)(1 + \varepsilon_0)}{A_0 \varepsilon_0}, \tag{1}$$

The changes in the structural relaxation of viscoelastic materials are dependent on the variations in production temperature and the life of their structures. If the change in temperature is extremely significant, it tends to alter the mechanical properties of the material. To ensure that the testing time does not become significantly long or short with temperature, it is necessary to obtain the logarithm of the temperature offset coefficient. Meanwhile, T_s is the reference temperature taken as 20°C, and isotherm curve of $\log(E(t)T_s/T)$ vs. $\log a_T$ corresponding to each test temperature T is shown in Figure 3. Translate each isothermal curve along the abscissa to 20°C of isothermal abscissa displacement value which is $\log a_T$. The specific method used can be found in the abovementioned standard [27]. In this way, the time-domain range of the equivalent relaxation modulus can be far more than 2–1800 s.

2.3. Fitting of Constitutive Equation. After fitting the above isothermal curve family, the relaxation modulus curve is obtained by using the temperature offset.

TABLE 2: Relaxation modulus at various temperatures.

T (°C)/t (s)	−40	−20	0	20	40	70
2	16.01	7.50	5.67	4.12	3.94	3.30
5	13.51	6.38	4.87	3.63	3.49	2.92
8	12.39	5.88	4.51	3.41	3.28	2.74
10	11.89	5.65	4.34	3.31	3.19	2.66
15	11.03	5.26	4.06	3.13	3.02	2.52
25	10.03	4.81	3.73	2.92	2.82	2.35
50	8.82	4.26	3.33	2.66	2.58	2.14
80	8.09	3.92	3.08	2.49	2.42	2.01
100	7.76	3.77	2.97	2.42	2.35	1.95
200	6.83	3.34	2.65	2.20	2.15	1.78
250	6.55	3.21	2.55	2.13	2.08	1.73
500	5.76	2.84	2.28	1.94	1.90	1.57
800	5.28	2.61	2.11	1.82	1.79	1.48
1000	5.07	2.51	2.03	1.77	1.73	1.43
1500	4.70	2.34	1.90	1.67	1.64	1.36
1800	4.55	2.27	1.84	1.63	1.61	1.33

The formula [28–33] used for Prony series fitting (as shown in Figure 4) of the relaxation modulus is as follows:

$$E(t) = E_0 + \sum E_i \exp\left(\frac{-X}{t_i}\right), \quad (i = 1 \sim 9), \tag{2}$$

where E_i is the transient modulus of the material and t_i is the Prony lag time constant. All the 19 parameters are shown in Table 3.

In this way, the constitutive equation of this viscoelastic material is developed.

3. Sinusoidal Frequency Sweep

The sinusoidal vibration test is divided into fixed frequency test and sweep frequency test, and the sweep frequency test is divided into linear and logarithmic frequency sweep modes. During the test, the frequency is always constant, that is, the constant frequency test.
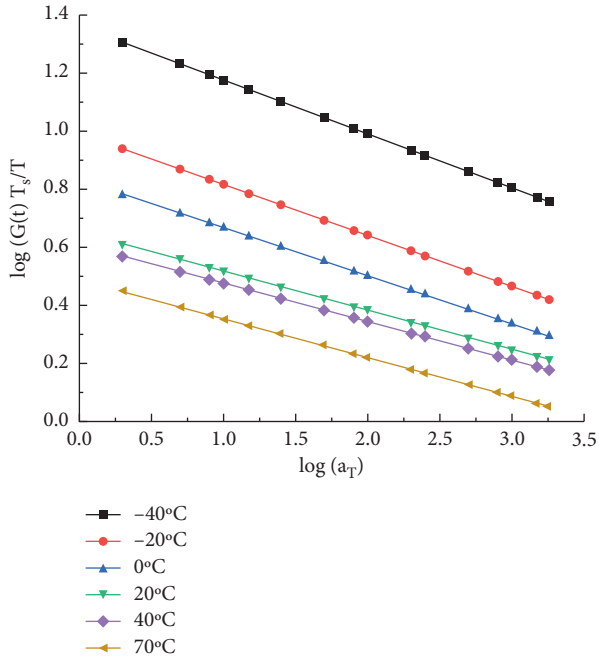
FIGURE 3: Isotherm family diagram.
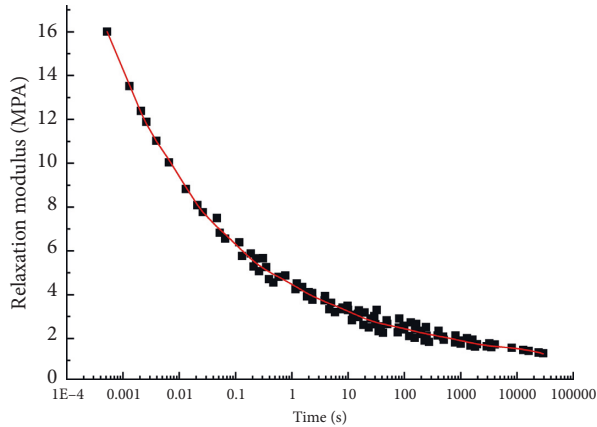
FIGURE 4: Master curve of relaxation modulus based on Prony series.

During the test, the frequency that changes with time is the frequency sweep test, and the vibration level in the frequency sweep test is a function of the frequency. The frequency sweep test is divided into linear frequency sweep and logarithmic frequency sweep according to the type of frequency change. Linear sweep frequency change is linear; log sweep frequency change is logarithmic.

3.1. Sinusoidal Frequency Sweep Set-Up.
The sinusoidal sweep vibration test excites the test piece by continuously changing the vibration frequency in a certain frequency range, according to the prescribed vibration magnitude. The rate of change of the vibration frequency is called the scanning rate.

The relationship between the excitation frequency (f), testing time (t), and scanning rate (β) is expressed in the linear frequency sweep as follows:

$$\frac{\mathrm{d}f}{\mathrm{d}t} = \beta \, (\text{constant}). \tag{3}$$

In logarithmic sweep, it is expressed as follows:

$$\frac{\mathrm{d}(\inf)}{\mathrm{d}t} = \beta \, (\text{constant}). \tag{4}$$

The starting frequency of the vibration test is recorded as f_0, and the starting time is recorded as t_0. Using equation (4), the relationship between the real-time frequency and t of the logarithmic sweep test is

$$f = f_0 \times e^{\beta(t-t_0)}. \tag{5}$$

A relatively simple functional relationship is observed between f and t during the linear frequency sweep test and the logarithmic frequency sweep test. Herein, the frequency scanning mechanism in sinusoidal frequency sweep test is known, and the starting time t_0 is defined by the data collector. Furthermore, the excitation frequency at any time can be calculated according to the frequency scanning mechanism by using t_0 only.

The yellow bench on the left is a self-made test bench (as shown in Figure 5), which is rigidly connected to the ground with bolts. A vibration exciter is placed on the test bench. The SIEMENS TESTLAB host is on the left, behind the exciter; a domestic amplifier is observed on the right, which controls the amplitude of signal amplification.

The figure on the right shows the clamping state of the viscoelastic cantilever beam. The size of the cantilever beam is $150\,\mathrm{mm} * 40\,\mathrm{mm} * 1\,\mathrm{mm}$. For the sinusoidal vibration test, in view of the large operation error caused by the cutting of the specimen and the position of the sensor, only one specimen was made. From left to right, five sensors from the PCB Company are observed, of which No. 1, 2, 3, and 4 are accelerometers and No. 5 functions as a force sensor as well as an accelerometer (distributed upper and lower). The force sensor model is PCB-208C01, and the measurement range is 0 to 0.4448 KN. The accelerometer model is PCB-356A15, and the measurement range is 0 to 490 m/s². The force sensor is located at the source of the exciting vibration; therefore, the data it records can be considered a standard of the input exciting force. The clamping device is rigidly connected to the viscoelastic cantilever beam specimen, the test bench, and the ground.

3.2. Analysis of Experimental Modal.
Select the 6 S-point marks that are relatively stable in the steady-state diagram, where the S-point mark indicates that the mode appears at this position, and then use the PloyMAX method to modal identification of the 6 S-points to obtain the corresponding sixth-order modal as shown in Figure 6.

After the test and calculation in SIEMENS TESTLAB itself, sixth-order modal frequencies are obtained [34–38] (Table 4).

TABLE 3: Parameters of Prony series fitting.

i	0	1	2	3	4	5	6	7	8	9
E_i (MPa)	0.301	6.512	4.291	2.572	1.455	1.203	0.550	0.604	0.054	1.348
t_i (s)		$10-3$	$10-2$	$10-1$	100	101	102	103	104	105
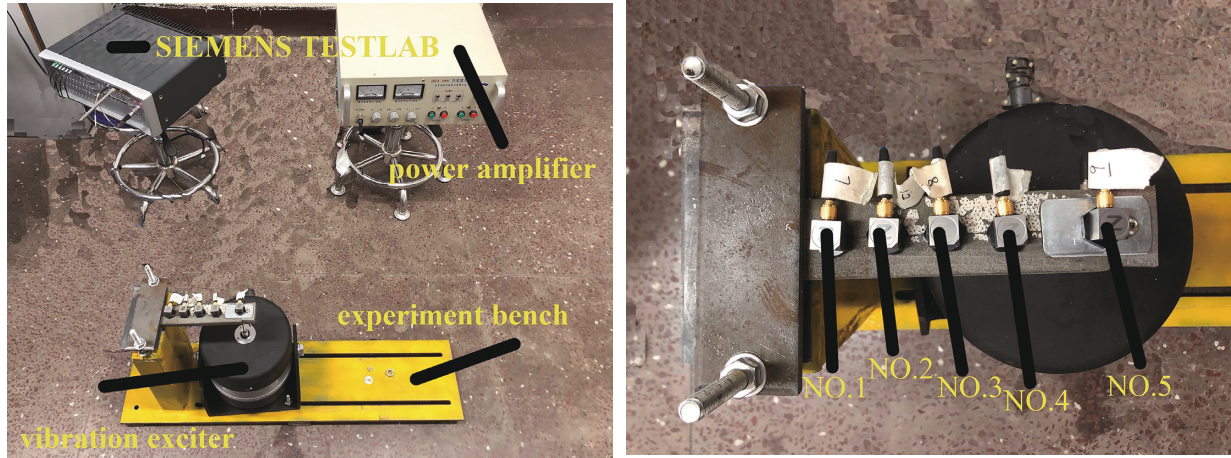
FIGURE 5: Vibration test bench.
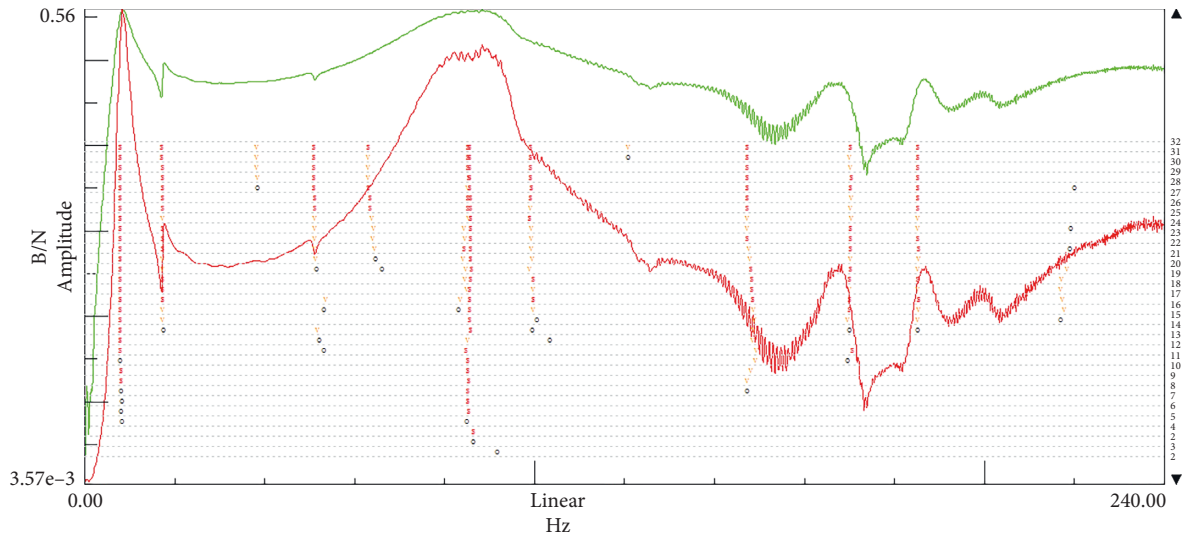
FIGURE 6: Steady-state graph based on Polymax.

TABLE 4: Sixth-order modal and frequency table.

Order	Frequency (Hz)	Damping ratio (%)	Participatory method
1	8.08	3.35	PolyMAX
2	17.30	3.75	PolyMAX
3	85.31	2.98	PolyMAX
4	148.04	4.22	PolyMAX
5	169.60	4.55	PolyMAX
6	238.06	3.97	PolyMAX

Although the continuum theoretically has an infinite number of natural frequencies, in many cases, we only care about low-order natural frequencies or specific-order natural frequencies. This is because the lower the natural frequency, the easier it is to be stimulated by the outside world. In addition, combined with the transportation and storage conditions of the propellant, the maximum frequency of the sinusoidal frequency sweep experiment is set at 80 Hz.

3.3. Sinusoidal Frequency Sweep Test. In the SIEMENS TESTLAB, the maximum frequency is set at 80 Hz, while the bandwidth, spectral line, resolution, capture time, and number of cycles are 80 Hz, 1024, 0.0781250 Hz, 10 s, and 30, respectively. Subsequently, the sinusoidal frequency sweep experiment is carried out. Since No. 5 acts as an
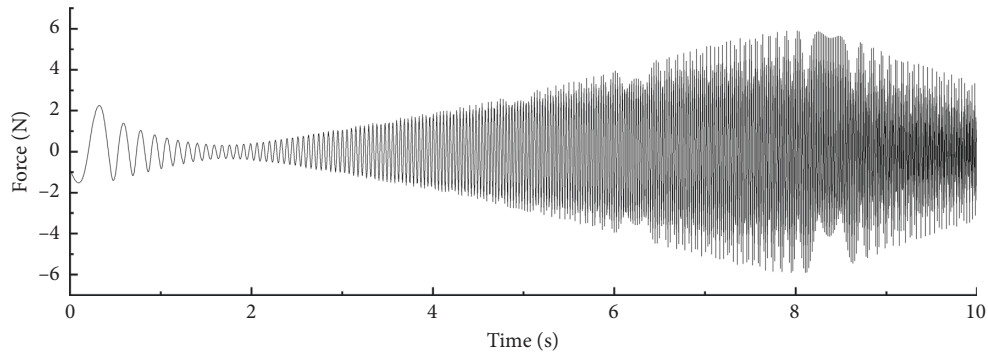
FIGURE 7: Measured input force values at point 5.
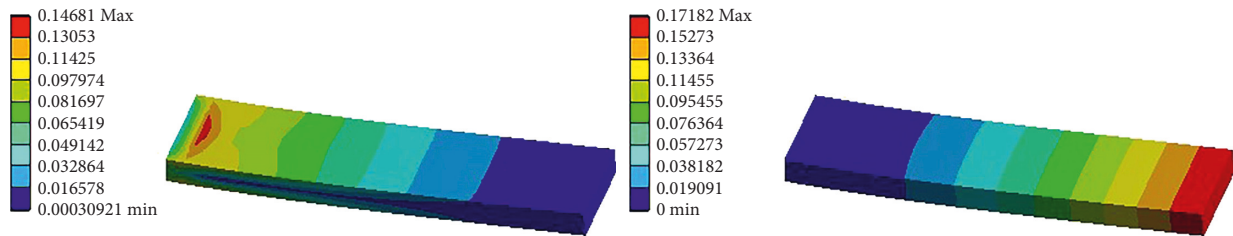
FIGURE 8: Strain and displacement contour.

accelerometer and a force sensor, the force data can be read in SIEMENS TESTLAB; these data are obtained after rectangular windowing and used as the reference input values for transient structure analysis. According to the results of the test measurement, the measured maximum force value is 5.90 N (as shown in Figure 7).

4. Finite Element Simulation and Analysis

The realization of finite element simulation is based on Workbench. Workbench is a collaborative simulation environment proposed by ANSYS to solve the heterogeneous problem of CAE software in the process of enterprise product development. The left end of the viscoelastic cantilever beam is constrained by a fixed end, which is realized with a self-made fixture. At the right edge is a concentrated load (infinitely close to the edge). The geometric model is realized by using the drawing function of the software [39, 40]. The length, width, and height of the cuboid model are 150, 40, and 10 mm, respectively. In the finite element simulation of viscoelastic materials, Prony series are mainly used to express its constitutive equation. The density of this material was measured to be 1700 kg/m^3, and Poisson's ratio was 0.495. All the elements are categorized according to their hexahedral solids. In the finite element method, the number of meshes is 64000 and the number of nodes is 281621. On this basis, the calculation shows good convergence. As observed, the maximum strain (as shown in the left in Figure 8) is 0.14681 and the maximum displacement (as shown in the left in Figure 8) is 0.17182 m.

The accelerations measured at the five points (by sensors No. 1 to No. 5) using the SIEMENS TESTLAB are exported and compared with those determined using finite element simulation. In the time domain, the simulated and measured accelerations at point 1 coincide well for the first 7 s; however, the overall simulated acceleration from 7–10 s is slightly smaller than the measured acceleration. The measured peak acceleration is 20.39 m/s^2, simulated peak acceleration is 20.88 m/s^2, peak acceleration error is 2.4%, and the simulated and measured peak accelerations appear at about 8 s. The simulated and measured accelerations at point 2 coincide well, and the peak acceleration also appears at approximately 8 s. The measured peak acceleration is 48.59 m/s^2, simulated peak acceleration is 49.70 m/s^2, and peak acceleration error is 2.28%. The simulated and measured values at point 3 do not coincide that well as those at point 2; however, both appear at 8 s. The measured peak acceleration is 59.50 m/s^2, simulated peak acceleration is 59 m/s^2, and peak acceleration error is 0.84%. At point 4, a good match is observed between the simulated and measured accelerations in the first 4 s, which becomes slightly worse from 4 to 8 s; however, the values still exhibit a reasonable match. The measured peak acceleration is 45.58 m/s^2, simulated peak acceleration is 45.53 m/s^2, peak acceleration appears at 8 s, and peak acceleration error is 0.10. At point 5, the measured peak acceleration is 41.82 m/s^2, simulated peak acceleration is 43.00 m/s^2, and peak acceleration error is 2.82%; the simulated peak acceleration appears at 9 s, which coincides with the time when the measured peak acceleration appears. Among the measured accelerations at the five points, the maximum acceleration of the cantilever beam appears at point 3 (59.50 m/s^2) and the minimum acceleration of the cantilever beam appears at point 1 (20.38 m/s^2). The maximum simulated acceleration of the cantilever beam appears at point 3 (59 m/s^2. The minimum acceleration appears at point 1 (20.88 m/s^2),
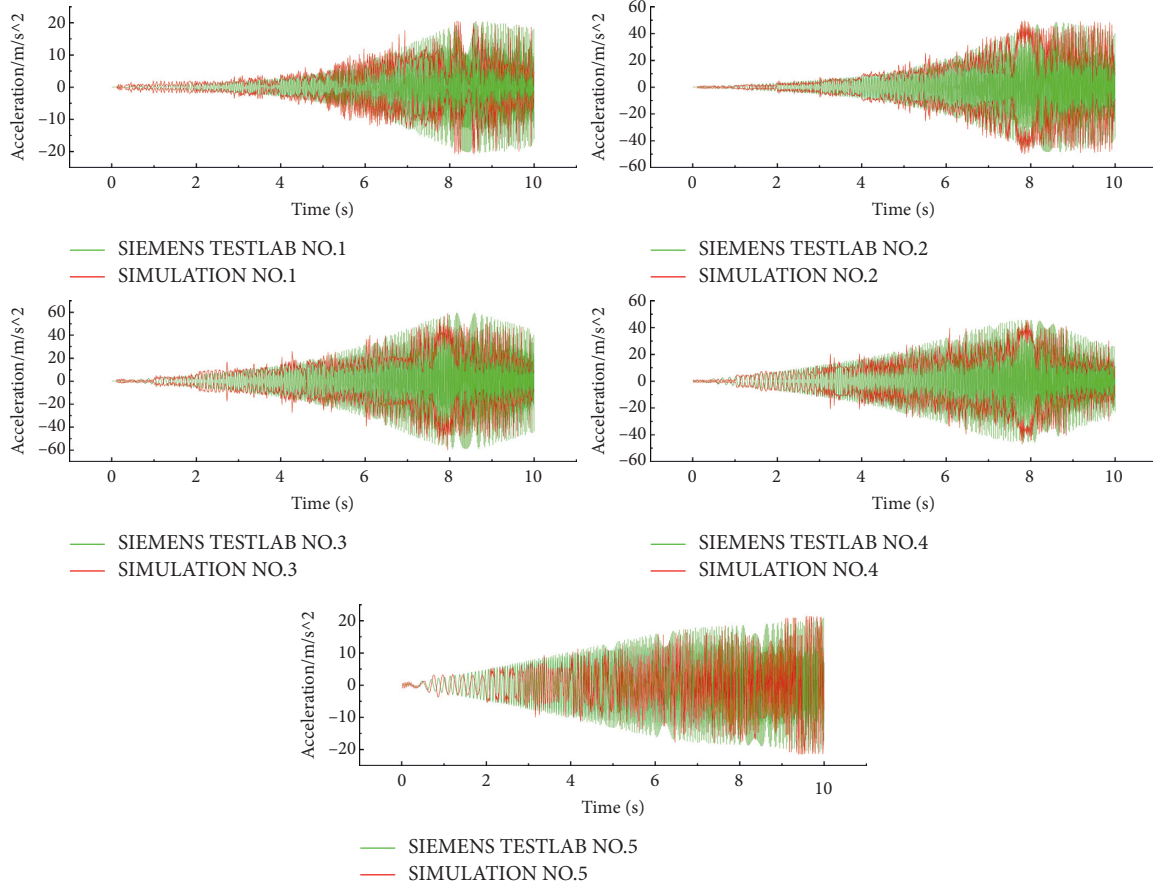
Figure 9: Measured and simulated accelerations at points 1 to 5.

Table 5: Maximum measured and simulated accelerations.

No.	Maximum measured acceleration (m/s²)	Maximum simulated acceleration (m/s²)	Relative error of simulation (%)
Point 1	20.39	20.88	2.40
Point 2	48.59	49.70	2.28
Point 3	59.50	59.00	0.84
Point 4	45.58	45.53	0.10
Point 5	41.82	43.00	2.82

and the simulated and measured values correspond well as shown in Figure 9 and Table 5.

In terms of the time domain, the peak errors of the simulated and measured values at the five points are all smaller than 3%. Furthermore, the peak accelerations also correspond well in the time domain.

5. Conclusion

This study carries out an experimental and simulation analysis on a viscoelastic cantilever beam, which analyzes the dynamic responses under dynamic conditions. The following conclusions are obtained:

(1) When the viscoelastic cantilever beam is sinusoidally excited, the maximum acceleration of the entire viscoelastic cantilever beam appears at the third point (the middle point), while the maximum

acceleration of other linear materials appears at the fifth point (movable endpoint), and the two are the smallest. The accelerations all occur at point 1 (fixed endpoint), and the reason for this difference is that viscoelastic materials experience a combination of viscosity and elasticity when they are sinusoidally excited.

(2) In the sinusoidal excitation experiment, by measuring the acceleration response of the viscoelastic cantilever beam at points 1, 2, 3, 4 and 5, it is observed that the overall acceleration peak error and the finite element simulation result are less than 3%. The time-domain correspondence is satisfactory. The 19-parameter Prony constitutive equation can accurately describe the dynamic response of viscoelastic materials at low frequencies (<80 Hz). Therefore, the use of the 19-parameter Prony series

method to describe viscoelastic materials is still one of the most effective methods in simulation.

Future work will continue to study the dynamic response of viscoelastic material cantilever beams under random vibration.

Data Availability

The data supporting the conclusion of the article are shown in the relevant figures and tables in the article.

Conflicts of Interest

The authors declare that there are no conflicts of interest regarding the publication of this article.

Acknowledgments

References

[1] L. Wei, *Identification of Fractional Derivative Viscoelasticity Model Parameters and its Finite Element Implementation*, Southwest Jiaotong University, Sichuan, China, 2018.

[2] H. Qian, Y. Wu, R. Zhu, and D. Zhang, "Modal Identification of Ultralow-Frequency Flexible Structures Based on Digital Image Correlation Method," *Applied sciences*, vol. 12, no. 1, 2021.

[3] J. Xu, Y. Ju, J. Zheng, and B. Han, "Acquisition of the relaxation modulus of composite solid propellant," *Chinese Journal of Explosives & Propellants*, vol. 34, no. 5, 2019.

[4] T. Miller, J. A. Louke, and C. S. Wojner, "Measuring propellant stress relaxation modulus using dynamic mechanical analyzer," *Journal of Propulsion & Power*, vol. 33, no. 5, 2017.

[5] Z. Zhou, X. Dong, Z. Li, K. Yu, C. Ding, and Y. Yang, "Spatiotemporal feature encoding for traffic accident detection in VANET environment," *IEEE Transactions on Intelligent Transportation Systems*, vol. 14, 2022.

[6] L. He, *Dynamic Analysis of Viscoelastic Materials Based on Prony Series and GHM Model*, Tsinghua University, Beijing, China, 2013.

[7] L. Zhao, H. Chai, Y. Han, K. Yu, and S. Mumtaz, "A collaborative V2X data correction method for road safety," *IEEE Transactions on Reliability*, vol. 55, pp. 1–12, 2022.

[8] G. M. Rowe, S. F. Brown, M. J. Sharrock, and M. G. Bouldin, "Viscoelastic analysis OF hot mix asphalt pavement structures," *J. Transportation Research Record*, vol. 12, 1995.

[9] H. Wang, *Design Optimization and Viscoelastic Response Analysis of Conductive Asphalt Pavement Based on Snow and Ice Melting*, Wuhan University of Technology, Hubei, China, 2010.

[10] D. Meng, Y. Xiao, Z. Guo et al., "A data-driven intelligent planning model for UAVs routing networks in mobile internet of things," *Computer Communications*, vol. 179, pp. 231–241, 2021.

[11] Y. Zhao, C. Zhou, G. Wang, and Z. Wang, "Analyses of viscoelastic responses of asphalt pavements under pulse loading," *Jersey Journal of Dalian University of Technology*, vol. 11, 2011.

[12] B. Wang and G. Zhang, "Analysis of dynamic response in three-dimensional viscoelastic large deformation," *J. Journal of Propulsion Technology*, vol. 20, 1994.

[13] X. Yuan and H. Sun, "Finite element analysis on viscoelastic properties of resin-based three-dimensional braided composites," *J. Chinese Journal of Applied Mechanics*, vol. 195, 2012.

[14] Z. Shi, C. Liu, and J. Yang, "Modified Riemann-Liouville fractional order derivative definition in solid propellant viscoelasticity constitutive model," *Chinese Journal of Applied Mechanics*, vol. 15, 2009.

[15] Z. Guo and H. Wang, "A deep graph neural network-based mechanism for social recommendations," *IEEE Transactions on Industrial Informatics*, vol. 17, no. 4, pp. 2776–2783, 2021.

[16] H. Zhou, L. Wang, H. Wang, and Y. Dai, "Viscous-elastic dynamic response for SRM grain under random loading," *Missiles and Space Vehicles*, vol. 20, 2019.

[17] J. Baqersad, P. Poozesh, C. Niezrecki, and B. Avaitabilie, "Comparison of Modal Parameters Extracted Using MIMO, SIMO, and Impact Hammer Tests on a Three-Bladed Wind Turbine," in *Proceedings of the Conference Proceedings of the Society for Experimental Mechanics Series book series (CPSEMS)*, Orlando, FL, USA, April 2014.

[18] W. Zheng and H. Chen, "Inverse multi-step prediction model method for MIMO random vibration test control," *Acta Aeronautica*, vol. 12, 2020.

[19] F. Zhu and Z. Deng, "Research on damage identification method based on random vibration response," *Annual Conference of Beijing Mechanics Society*, vol. 252, 2013.

[20] O. Yakaboski and A. V. Kumar, "Modeling and Simulation of RDX Powder Thermo-mechanical Response to Drop impact," *Propellants, Explosives, Pyrotechnics*, vol. 46, 2020.

[21] QJ 2487-1993, "Method for measuring uniaxial tensile stress relaxation modulus and master curve of composite solid propellant," 1993, https://www-bzgfw-com.translate.goog/forum.php?mod=misc&action=attachpay&aid=149529&tid=149521&_x_tr_sl=zh-CN&_x_tr_tl=en&_x_tr_hl=en&_x_tr_pto=sc&_x_tr_sch=http.

[22] J. J. Zhai, X. X. Kong, and L. C. Wang, "Thermo-Viscoelastic Response of 3D Braided Composites Based on a Novel FsMsFE Method," *Materials (Basel)*, vol. 14, 2021.

[23] R. W. Ogden, "Large deformation isotropic elasticity: on the correlation of theory and experiment for compressible rubberlike solids," *Proceedings of the Royal Society A: Mathematical*, vol. 326, 1972.

[24] P. H. Mott, C. M. Roland, and R. D. Corsaro, "Acoustic and dynamic mechanical properties of a polyurethane rubber," *Journal of the Acoustical Society of America*, vol. 111, 2002.

[25] Y. Wang, Y. Bai, X. Xu, J. Wang, and L. Li, "A Method for High-Accuracy Spectrum Analysis of Structural Response in Sine-Swept Vibration Test," *Journal of Spacecraft Environment Engineering*, vol. 983, 2020.

[26] H. Roy and S. Chandraker, "Dynamic study of viscoelastic rotor: modal analysis of higher order model considering various asymmetries," *Journal of Mechanism and Machine Theory*, vol. 109, 2017.

[27] N. Mills, "Finite element models for the viscoelasticity of open-cell polyurethane foam," *Journal of Cellular Polymers*, vol. 25, 2006.

[28] M. Liu, "Frequency Domain Method of the Crack Growth Life Analysis for Structure Vibration Fatigue," *Nanjing University of Aeronautics and Astronautics*, vol. 47, 2017.

[29] H. Fouad, A. Mourad, B. A. Alshammari, and M. K. Hassan, "Fracture toughness, vibration modal analysis and viscoelastic

behavior of Kevlar, glass, and carbon fiber/epoxy composites for dental-post applications," *Journal of the Mechanical Behavior of Biomedical Materials*, vol. 101, 2019.

[30] H. Shuai, C. Wen, and X. Gou, "Modal analysis of fractional derivative damping model of frequency-dependent viscoelastic soft matter," *Advances in Vibration Engineering*, vol. 10, no. 3, 2016.

[31] E. D. Lorenzo, S. Manzato, B. Peeters, and V. Ruffini, "Modal Analysis of Wind Turbine Blades with Different Test Setup Configurations," *Topics in Model Analysis and Testing*, vol. 8, 2020.

[32] W. Xie and Z. Zhang, "Dynamic Test and Analysis of the Structure of the Stadium Stand in Suzhou Industrial Park," *Applied sciences*, vol. 12, 2021.

[33] S. H. Wang, L. Zhang, and T. Li, "Vibration test analysis and control of solid rocket motor," *J. Computer Measurement and Control*, vol. 57-63, 2017.

[34] R. M. Hidalgo, J. G. Fernandez, R. R. Rivera, and H. A. Lorrondo, "A simple adjustable window algorithm to improve FFT measurements," *IEEE Transactions on Instrumentation and Measurement*, vol. 51, 2002.

[35] H. Zheng, J. P. Ertel, M. Kourmpetis, and J. Kanfoud, "Integrity testing of cast in situ concrete piles based on an impulse response function method using sine-sweep excitation by a shaker," *Journal of Non-destructive Evaluation*, vol. 55, 2019.

[36] Y. F. Wang, G. C. Li, and X. W. Wang, "Storage and life prediction of solid rocket motors in marine environment," *Chinese Journal of Explosives & Propellants*, vol. 66, 2008.

[37] Z. Li, *Viscoelastic Fractional Derivative Model and its Application to Solid Motors*, Tsinghua University, Beijing, China, 2000.

[38] A. Plouin and E. Balmès, "Steel/viscoelastic/steel sandwich shells," in *Proceedings of the Computational Methods and Experimental Validations//International Modal Analysis Conference*, Honolulu, Hawaii, December, 2000.

[39] G. Xia, T. Zhao, and L. Guan, "Enhanced thermal and mechanical properties of PW-based HTPB binder using polystyrene (PS) and PS–SiO$_2$ microencapsulated paraffin wax (MePW)," *Journal of Applied Polymer Science*, vol. 110, 2018.

[40] H. B. Li and Y. B. Li, "Experimental study on Poisson's ratio of viscoelastic grain," *The Journal of New Industrialization*, vol. 61, 2016.

Research Article

Digital Evaluation of Vertical Compressive Bearing Capacity for Jet Grouting Pile-Mini Steel Pipe Pile Composite Foundation

Xiaojun Wang [ID],[1] **Zhipeng Mao,**[2] **and Wendi Wang**[3]

[1]*School of Civil Engineering and Architecture, NingboTech University, Ningbo, Zhejiang, China*
[2]*Zhejiang Wenzhou Yongtaiwen Expressway Co Ltd, Wenzhou, Zhejiang, China*
[3]*Ningbo Architectural Design and Research Institute Co Ltd, Ningbo, Zhejiang, China*

Correspondence should be addressed to Xiaojun Wang; wangxj@nit.zju.edu.cn

The jet grouting pile-mini steel pipe pile in soft soil area is composed of the jet grouting pile and the mini steel pipe pile. Through the analysis of the stress mode of the composite foundation under the overall compression of the pile top, the hypothetical diagram and calculation equation of the interfacial friction resistance distribution of the composite foundation are put forward. Thus, the calculation equation of the axial force of the mini steel pipe pile and the jet grouting pile is deduced, and the axial force distribution diagram of the mini steel pipe pile and the jet grouting pile in the composite foundation is defined. The vertical compression composite foundation in the field was selected for bearing capacity test and calculation and comparative analysis, and the relative error was 3%. Therefore, the stress mode and calculation method of the jet grouting pile-mini steel pipe pile proposed in this paper can meet the needs of engineering design and popularization and application of the composite foundation.

1. Introduction

The jet grouting pile-mini steel pipe pile composite foundation refers to the combined system formed by the jet grouting pile and the mini steel pipe pile to share external load [1]. In the soft soil layer, the jet grouting pile with a certain depth and diameter shall be constructed first. Before the initial solidification of the jet grouting pile [2], the mini steel pipe pile with diameter less than Φ300 mm and length less than the length of the jet grouting pile is vertically pushed into the jet grouting pile along the central part by the improved microinserting and pressing mechanical equipment. After the strength of the jet grouting pile reaches 28 days, the composite foundation is formed [3]. In this combined system, the pile top load is mainly transmitted to the jet grouting pile through the friction around the mini steel pipe pile [4], and then the load is transmitted to the soil around the pile mainly by the friction force around the jet grouting pile [5] so as to complete the load transmission [6].

This system can take maximum advantage of the "high strength" characteristics of mini steel pipe pile to bear the load [7] and use the reinforcement effect of jet grouting pile on soft soil and large pile side surface area to provide sufficient side friction resistance [8]. Although the load plate test is more appropriate to discuss the bearing capacity of the composite foundation [9], its deformation and load transfer law cannot be directly extended to the actual engineering design. Therefore [10], it is necessary to study and give a reasonable and simple calculation method of the bearing capacity of the composite foundation [11] so as to make the composite foundation better popularized in engineering application [12], which is the main scientific and technological problem to be solved in this paper. The composite foundation is used in the foundation reinforcement project with the engineering geological condition of soft soils. For the convenience of description, the jet grouting pile-mini steel pipe pile composite foundation is abbreviated as the composite foundation.

2. Stress Mode Analysis of the Composite Foundation under Vertical Compressive Load

It is assumed that in the composite foundation, the uniformity of the jet grouting pile is good [13], and the diameter of the pile body remains unchanged in the depth direction. The mini steel pipe pile and the composite foundation are regarded as pure friction piles, and the bottom axial force is considered as 0. Figure 1 is a schematic diagram of the force transfer mechanism of the composite foundation under vertical compressive load. According to the vertical force transfer characteristics of the composite foundation shown in Figure 1, the composite foundation can be divided into upper and lower parts of "inserted mini steel pipe pile section" and "pure jet grouting pile section" along the depth direction. Due to the small rigidity of the jet grouting pile, when the length of the pure jet grouting pile section is large, the side friction resistance of the "pure jet grouting pile section" mainly acts on the "effective section of the pure jet grouting pile" with the length of L_c. The side friction resistance between the non-effective section at the bottom of the jet grouting pile and soil around the pile is very small, which can be ignored. Therefore, in the calculation of bearing capacity, the effective length of the "pure jet grouting pile section" in the composite foundation should be guaranteed as far as possible so as to reduce the length of the mini steel pipe pile. It is generally believed that the effective pile length of the jet grouting pile shall not exceed 10 m. Combined with the concept of effective pile length of jet grouting pile, the value of the "effective section of pure jet grouting pile" L_c in the composite foundation can be obtained by the following equation:

$$L_c = L_j - L_s \leq \min\{\beta D_j, 10\}. \tag{1}$$

In the formula, L_c is the length of the "effective section of the pure jet grouting pile"; L_j is the effective length of the jet grouting pile; L_s is the length of the mini steel pipe pile. According to the strength of the jet grouting pile body, $\beta = 10 \sim 18$. D_j is the diameter of the jet grouting pile.

Under the overall compression mode of the mini steel pipe pile and jet grouting pile jointly bearing the upper load, the bearing performance of the mini steel pipe pile and the jet grouting pile should be considered at the same time [14, 15].

The ultimate compressive bearing capacity of the mini steel pipe pile at the pile top shall meet the following equation:

$$Q_{0s} \leq Q_{su} = \sigma_{su} A_s. \tag{2}$$

The load shared by the top of the jet grouting pile can be calculated according to the following formula:

$$Q_{ju} \geq Q_{0j} = \frac{Q_{su} A_j}{A_s n_p}, \tag{3}$$

$$A_j = \begin{cases} \left(D_j^2 - D_s^2\right)\dfrac{\pi}{4} & (0 < Z < L_s), \\ D_j^2 \dfrac{\pi}{4} & (L_s \leq Z). \end{cases} \tag{4}$$

In the equation, Q_{0s} is the compressive load shared by the pile top of the mini steel pipe pile; Q_{0j} is the compressive load shared by the top of the jet grouting pile; Q_{su} is the vertical ultimate compressive bearing capacity of the mini steel pipe pile controlled by yield strength; Q_{ju} is the vertical ultimate compressive bearing capacity of the jet grouting pile without confined compressive strength control; σ_{su} is the yield strength of the mini steel pipe pile; A_s is the cross-sectional area of the mini steel pipe pile, $A_s = \pi(T_s D_s - T_s^2)$, where T_s is the wall thickness of the mini steel pipe pile, and D_s is the outer diameter of the mini steel pipe pile; D_j is the diameter of the jet grouting pile; $n_p = \sigma_{0s}/\sigma_{0j}$ is the stress sharing ratio of the mini steel pipe pile and the jet grouting pile at the pile top; A_j is the cross-sectional area of the jet grouting pile, determined by (4); Z is the depth; L_s is the length of the mini steel pipe pile; L_j is the effective length of the jet grouting pile.

In addition, to coordinate the ultimate side friction at the interface between the mini steel pipe pile and the jet grouting pile with the ultimate side friction at the interface between the jet grouting pile and soil, it should also be noted that there is no shear failure between the mini steel pipe pile and the jet grouting pile under the condition of ensuring the material strength of the pile body [16–18]. Therefore, the bonding strength (ultimate side friction) at the interface between the mini steel pipe pile and the grouting pile should meet the following conditions:

$$Q_{0s} \leq f_{su}, \tag{5}$$

$$f_{su} = U_s \int_0^{L_s} q_s(Z)dz \ \ 0 \leq Z \leq L_s, \tag{6}$$

The composite foundation is used as a friction pile, so the pile top load shall not be greater than the ultimate side friction resistance of the jet grouting pile-soil interface.

$$Q_0 \leq f_{ju}, \tag{7}$$

$$Q_0 = Q_{0s} + Q_{0j}, \tag{8}$$

$$f_{ju} = U_j \int_0^{L_j} q_j(Z)dz \ \ 0 \leq Z \leq L_j, \tag{9}$$

In the equation, $q_s(Z)$ is the side friction resistance at the interface between the mini steel pipe pile and the jet grouting pile at depth Z; $q_j(Z)$ is the side friction resistance at the interface between the jet grouting pile and soil at depth Z; f_{su} is the ultimate side friction resistance at the interface between the mini steel pipe pile and the jet grouting pile; f_{ju} is the ultimate side friction resistance at the interface between the jet grouting pile and soil; U_s is the perimeter of the mini steel pipe pile; U_j is the perimeter of the jet grouting pile; Z is the depth; L_s is the length of the mini steel pipe pile; L_j is the effective length of the jet grouting pile; Q_0 is the pile top load.

According to the analysis results of the numerical model [19, 20], under the vertical compressive load, the maximum axial force of the jet grouting pile appears at the depth of 0 m
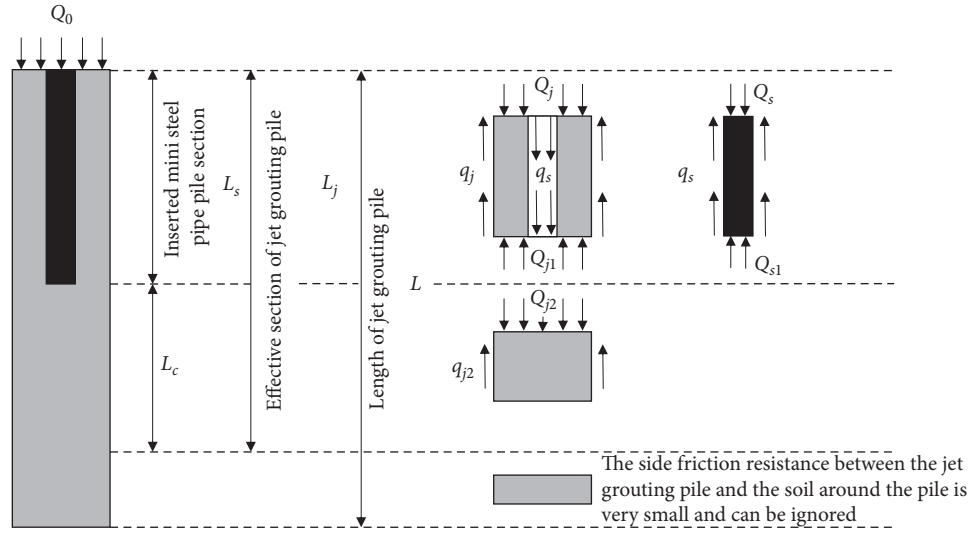
FIGURE 1: The schematic diagram of the force transfer mechanism of the composite foundation under vertical compressive load.

and the bottom of the mini steel pipe pile ($Z = L_s$). Therefore, when calculating the compressive bearing capacity of the composite foundation, the strength of the jet grouting pile needs to be checked according to equations (10) to (12).

$$Q_{0j} \leq Q_{ju} = \sigma_{ju} A_j, \tag{10}$$

$$Q_j (L_s) \leq R_2, \tag{11}$$

$$R_2 = \gamma_c Q_{ju}. \tag{12}$$

In the equation, σ_{ju} is the vertical compressive strength of the jet grouting pile (taking unconfined compressive strength); $Q_j (L_s)$ is the axial force of the jet grouting pile at depth L_s; R_2 is the maximum bearing capacity controlled by the pile body material of the "pure jet grouting pile section"; γ_c is the reduction coefficient of vertical compressive strength of the jet grouting pile. In case of lack of test data, $\gamma_c = 1$.

3. Assumption of the Interfacial Friction Distribution of the Composite Foundation under Vertical Compressive Load

According to relevant research results [20–22], the distribution law of side friction resistance between the mini steel pipe pile and the jet grouting pile and side friction resistance between the jet grouting pile and the soil around pile can be simply assumed, as shown in Figures 2 and 3, so as to facilitate design and calculation.

3.1. Assumption of Interfacial Friction Resistance Distribution between the Mini Steel Pipe Pile and the Jet Grouting Pile under Vertical Compressive Load. As can be seen from Figure 2, after simplifying the hypothesis, the side friction resistance between the mini steel pipe pile and the jet grouting pile presents a three-step distribution of small in the upper and
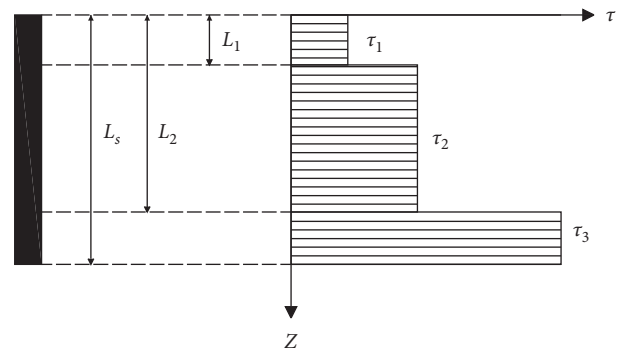
FIGURE 2: Distribution of interfacial friction resistance between the mini steel pipe pile and the jet grouting pile under overall compression mode.
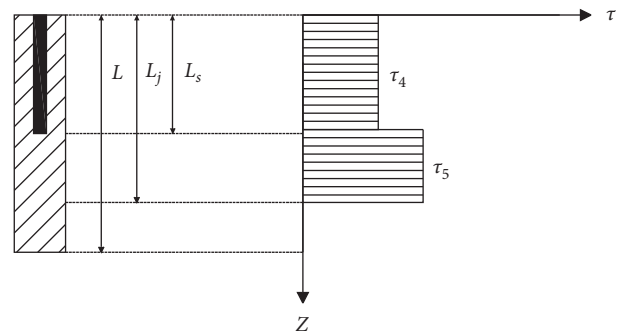
FIGURE 3: Distribution of interfacial friction resistance between the jet grouting pile and soil under overall compression mode.

large in the lower. The depth range of the first step is $0 \sim L_1$, and the average side friction resistance is τ_1; the depth range of the second step is $L_1 \sim L_2$, and the average side friction is τ_2; the depth range of the third step is $L_2 \sim L_s$, and the average side friction resistance is τ_3. The distribution of side friction resistance $q_s (Z)$ at the interface between the mini steel pipe pile and the jet grouting pile can be expressed by as

$$q_s(Z) = \begin{cases} \tau_1 & (0 \le Z < L_1) \\ \tau_2 & (L_1 \le Z < L_2), \\ \tau_3 & (L_2 \le Z < L_s) \end{cases} \quad (13)$$

$$\tau_2 = 2\tau_1 = \xi\tau_3, \quad (14)$$

$$\tau_3 = \tau_u = \kappa\sigma_{ju}, \quad (15)$$

$$L_1 = \alpha D_s, \quad (16)$$

$$L_2 = L_s - L_1. \quad (17)$$

In the equation, $q_s(Z)$ is the side friction resistance between the mini steel pipe pile and the jet grouting pile; Z is the depth; τ_1, τ_2, and τ_3 are the average side friction resistance between the mini steel pipe pile and the jet grouting pile in different depth ranges. The value of ξ is based on the extent of the bonding force in the middle section of the mini steel pipe pile, and its proposed value is 0.05 according to the numerical simulation results. τ_u is the ultimate side friction resistance at the interface between the mini steel pipe pile and the jet grouting pile, which is related to the compressive strength of the jet grouting pile and the smoothness of the mini steel pipe pile κ, $\kappa = 0.15 \sim 0.4$; σ_{ju} is the compressive strength of the jet grouting pile; L_s is the length of the mini steel pipe pile; D_s is the outer diameter of the mini steel pipe pile; the value of α is taken according to the range of bonding force between the mini steel pipe pile and the jet grouting pile. When the whole composite foundation is compressed, $\alpha = 15$.

3.2. Assumption of the Distribution of Interfacial Friction Resistance between the Jet Grouting Pile and Soil under Vertical Compressive Load. As can be seen from Figure 3, the side friction resistance at the interface between the jet grouting pile and the soil after the simplified assumption is divided into the upper and lower parts of "inserted mini steel pipe pile section" and "pure jet grouting pile section." The properties of the upper soil layer are often poor, and the ultimate side friction resistance at the upper part of the jet grouting pile-soil interface will be less than that at the lower part, which generally presents a two-step distribution. Therefore, the distribution of side friction resistance at the interface between the jet grouting pile and soil is

$$q_j(Z) = \begin{cases} \tau_4 & (0 \le Z < L_s) \\ \tau_5 & (L_s \le Z < L_j) \\ 0 & (L_j \le Z \le L). \end{cases} \quad (18)$$

In the equation, $q_j(Z)$ is the side friction resistance between the jet grouting pile and the soil around the pile; Z is the depth; τ_4 and τ_5 are the average ultimate side friction resistance of the jet grouting pile-soil interface in different depth ranges, which can be obtained according to the geological exploration report; L_s is the length of the mini steel pipe pile; L_j is the effective length of the jet grouting pile, and the value is shown in equation (1); L is the pile length of the jet grouting pile.

4. Axial Force Calculation of the Composite Foundation under Vertical Compressive Load

The above assumption of interfacial friction resistance distribution can be applied to the calculation of axial force of the composite foundation. According to the numerical simulation results, the mini steel pipe pile and the composite foundation can be regarded as the pure friction pile, and the bottom axial force can be regarded as 0. According to the force transmission mechanism of the composite foundation, the calculation equation of axial force of the composite foundation is established.

The cumulative sum of the side friction resistance of the mini steel pipe pile is equal to the upper load shared by its pile top. The axial force of the mini steel pipe pile can be expressed as

$$Q_s(Z) = Q_{0s} - U_s \int_0^Z q_s(Z)dZ. \quad (19)$$

Substituting equation (13) into equation (19), we obtain the following equation:

$$Q_s(Z) = \begin{cases} Q_{0s} - U_s\tau_1 Z & (0 \le Z < L_1), \\ Q_{0s} - U_s(\tau_1 L_1 + \tau_2 Z) & (L_1 \le Z < L_2), \\ \tau_3(L_s - Z) & (L_2 \le Z < L_s). \end{cases} \quad (20)$$

In the equation, $Q_s(Z)$ is the axial force of the mini steel pipe pile at different depths; τ_1, τ_2, and τ_3 are the average side friction resistance at the interface between the mini steel pipe pile and the jet grouting pile in different depth ranges; U_s is the perimeter of the mini steel pipe pile; Z is the depth; L_s is the length of the mini steel pipe pile; the values of L_1 and L_2 refer to equations (16) and (17), respectively.

The axial force of the jet grouting pile in the "inserted mini steel pipe pile section" is composed of the upper load shared by the top of the jet grouting pile, the side friction resistance of the mini steel pipe pile-jet grouting pile interface, and the side friction resistance of the jet grouting pile-soil interface, which can be expressed by equation (21).

The axial force distribution of the jet grouting pile is

$$Q_j(Z) = Q_{0j} + U_s \int_0^Z q_s(Z)dZ - U_j \int_0^Z q_j(Z)dZ. \quad (21)$$

Substituting equations (13) and (18) into equation (21), equation (22) can be obtained as follows:

$$Q_j(Z) = \begin{cases} Q_{0j} + (U_s\tau_1 - U_j\tau_4)Z & (0 \le Z < L_1), \\ Q_{0j} + (U_s\tau_1 - U_j\tau_4)L_1 + (U_s\tau_2 - U_j\tau_4)Z & (L_1 \le Z < L_2), \\ Q_{0j} + (U_s\tau_1 - U_j\tau_4)L_1 + (U_s\tau_2 - U_j\tau_4)L_2 + (U_s\tau_3 - U_j\tau_4)Z & (L_2 \le Z < L_3), \\ U_j(L_j - Z)\tau_5 & (L_s \le Z < L_j). \end{cases}$$ (22)

In the equation, $Q_j(Z)$ is the axial force of the jet grouting pile; Q_{0j} is the load shared on the top of the jet grouting pile; τ_1, τ_2, and τ_3 are the average side friction resistance at the interface between the mini steel pipe pile and the jet grouting pile in different depth ranges; U_s is the perimeter of the mini steel pipe pile; U_j is the perimeter of the jet grouting pile; τ_4 and τ_5 are the average side friction resistance of the jet grouting pile-soil interface in different depth ranges, which can be obtained according to the geological exploration report; L_s is the length of the mini steel pipe pile; L_j is the effective length of the jet grouting pile.

According to equations (20) and (22), under the overall compression mode of the composite foundation, the axial force distribution of the mini steel pipe pile and the jet grouting pile is shown in Figures 4 and 5, respectively.

5. Calculation of Bearing Capacity of the Composite Foundation under Vertical Compressive Load

The field vertical compression composite foundation in soil layers shown in Table 1 was selected for bearing capacity test and calculation comparative analysis. The calculation of the vertical compressive bearing capacity of the composite foundation is divided into the calculation of the ultimate bearing capacity controlled by the interface strength of the composite foundation and the calculation of the ultimate bearing capacity controlled by the material strength of the pile body of the composite foundation, and the smaller of the two is taken as the ultimate compressive load of the composite foundation. The parameters of the jet grouting pile and the mini steel pipe pile of the test pile are shown in Tables 2 and 3, respectively. The ultimate side friction resistance of each soil layer in the test site is shown in Table 1. The stratum distribution and composite profile at the test site is shown in Table 4.

According to the concept of the effective pile length, D_j is substituted into (1), and $\beta = 18$. It is calculated that the "effective section of pure jet grouting pile" $L_c = 10$m, and the calculation process is shown in equations (23) and (24), so there is no "invalid section of the jet grouting pile" in the composite foundation.

$$L_c = L_j - L_s = 10\text{m},$$ (23)

$$\min\{\beta D_j, 10\} = \min\{18 \times 0.6, 10\} = 10\text{m} \ge L_c.$$ (24)

5.1. Maximum Bearing Capacity Controlled by Iinterface Strength.
According to Table 1 and Figure 6, the ultimate side friction resistance of the jet grouting pile-soil interface calculated in combination with equation (9) is

$$\begin{aligned} f_{ju} &= U_j \int_0^{L_j} q_j(Z)dz = 0.6\pi \times (1 \times 30 + 2 \times 23 + 6 \times 18 \\ &+ 5 \times 40 + 6 \times 29) = 1051\text{kN}. \end{aligned}$$ (25)

Combined with equation (6), equation (13), and Figure 2, the ultimate side friction resistance at the interface between the mini steel pipe pile and the jet grouting pile is calculated. Substituting the data in Table 3 into equations (16) and (17), respectively, $L_1 = 1.62$m and $L_2 = 8.38$m can be obtained, where $\alpha = 15$. According to Table 2, $\sigma_{ju} = 8$MPa $= 8000$kPa. $\kappa = 0.15 \sim 0.4$, so when taking $\kappa = (0.15 + 0.4)/2 = 0.275$ and substituting it into equation (15), $\tau_3 = 2200$kPa can be obtained; substituting $\xi = 0.05$ and τ_3 into equation (14), $\tau_2 = 110$kPa and $\tau_1 = 55$kPa can be obtained. Therefore, from equations (6) and (13), we obtain

$$\begin{aligned} f_{su} &= U_s \int_0^{L_s} q_s(Z)dz = U_s(L_1\tau_1 + (L_2 - L_1)\tau_2 + L_1\tau_3) \\ &= 0.108\pi \times (1.62 \times 55 + (8.38 - 1.62) \times 110 \\ &+ 1.62 \times 2200) = 1492\text{kN}. \end{aligned}$$

(26)

Therefore, according to equations (25) and (26), $f_{ju} < f_{su}$, so the maximum bearing capacity controlled by the interface strength of the composite foundation under the overall compression mode is

$$R_i = f_{su} = 1051\text{kN}.$$ (27)

5.2. The Maximum Bearing Capacity of the Composite Pile Top Controlled by Pile Material Strength.
The maximum bearing capacity of the mini steel pipe pile top under the control of pile material strength calculated by equation (2) and Table 3 is

$$\begin{aligned} Q_{0s} &\le Q_{su} = \sigma_{su}A_s = \sigma_{su}(T_sD_s - T_s^2)\pi \\ &= 358 \times 10^3 \times (0.008 \times 0.108 - 0.008^2)\pi = 900\text{kN}. \end{aligned}$$ (28)

The cross-sectional area of the jet grouting pile at the pile top calculated by equation (4) and Table 2 is

$$A_j = (D_j^2 - D_s^2)\frac{\pi}{4} = (0.6^2 - 0.108^2)\frac{\pi}{4} = 0.274\text{m}^2.$$ (29)
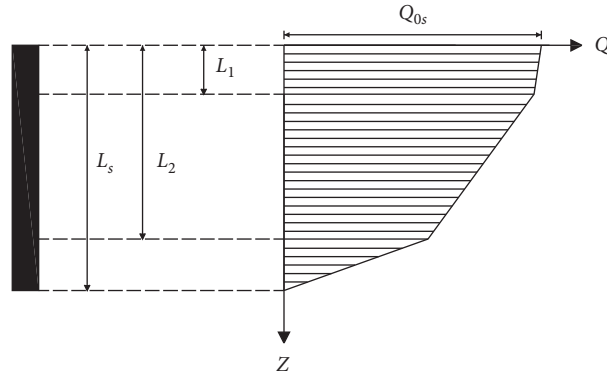
Figure 4: Axial force distribution of the mini steel pipe pile in the composite foundation under overall compression mode.
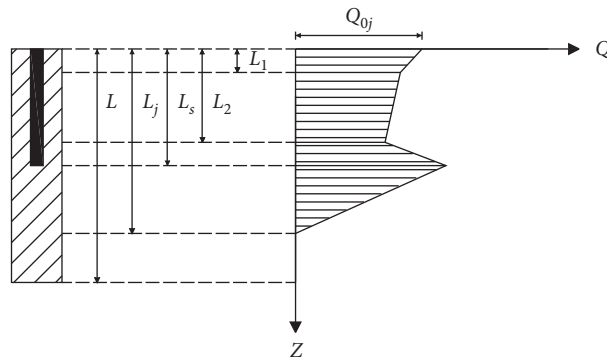
Figure 5: Axial force distribution of the jet grouting pile in the composite foundation under overall compression mode.

Table 1: Recommended value of ultimate side friction resistance of each soil layer.

Number	Name of soil	The state of the soil	Recommended value of ultimate side friction resistance/kPa
1	Silty clay	Plastic state, medium to high compressibility	30
2	Silty clay	Soft plastic state, medium to high compressibility	23
3	Mucky clay	High water content, high compressibility, flow plastic state	18
4	Silty clay with sand	Medium compressibility, slightly dense~moderately dense state	40
5	Silty clay	Soft plastic state, high compressibility	29

Table 2: Calculation parameters of the jet grouting pile.

Type of pile	Pile diameter D_j	Pile length L_j	Unconfined compressive strength	Tensile strength
Jet grouting pile	0.6 m	20 m	8 MPa	0.6 MPa

Table 3: Calculation parameters of the mini steel pipe pile.

Type of pile	Outer diameter D_s	Pile length L_s	Wall thickness T_s	Compressive yield strength	Tensile strength
Mini steel pipe pile	0.108 m	10 m	8 mm	358 MPa	410 MPa

Table 4: Comparison of measured and calculated bearing capacity of the composite foundation.

Load mode	Measured value of bearing capacity R_a/kN	Calculated value of bearing capacity R_c/kN	Absolute error/ kN	Relative error/%
Overall compressive strength of the composite foundation	1083	1051	32	3
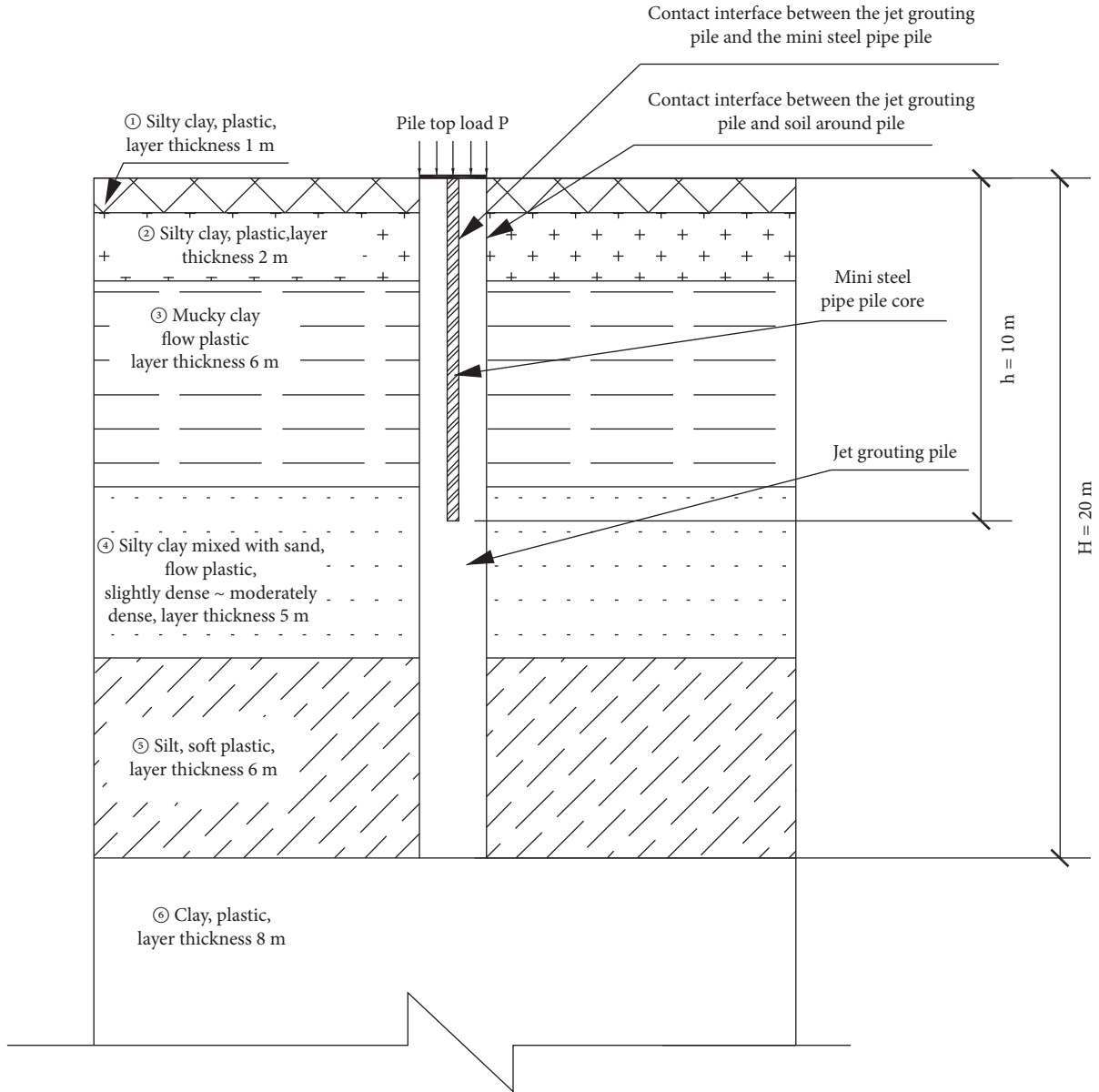
FIGURE 6: Stratum distribution and composite foundation profile at the test site.

The maximum bearing capacity of the jet grouting pile top under the control of pile material strength is calculated by substituting equation (10):

$$Q_{ju} = \sigma_{ju} A_j = 8 \times 10^3 \times 0.274 = 2192 kN. \tag{30}$$

According to the numerical simulation analysis under the overall compression mode of the composite foundation, the pile top stress sharing ratio of the mini steel pipe pile and the jet grouting pile is $n_p = 140$ [7]. The load Q_{0j} shared by the top of the jet grouting pile calculated by equation (3) is

$$Q_{0j} = Q_{su} \frac{A_j}{A_s n_p} = 900 \times \frac{0.274}{0.002513 \times 140} = 700 kN < Q_{ju}$$
$$= 2192 kN. \tag{31}$$

Therefore, the maximum bearing capacity of the pile top of the composite foundation under the overall compression mode is

$$R_t = Q_{su} + Q_{0j} = 900 + 700 = 1600 kN. \tag{32}$$

5.3. Maximum Bearing Capacity of the "Pure Jet Grouting Pile Section". Using equation (22) and Table 1, the maximum bearing capacity of the "pure jet grouting pile section" under the control of ultimate side friction resistance of the jet grouting pile is

$$R_1 = Q_j(L_c) = U_j \int_{L_s}^{L_j} q_j(Z) dz = 0.6\pi \times (4 \times 40 + 6 \times 29)$$
$$= 630 kN. \tag{33}$$

Using equation (10), Q_{ju} of the "pure jet grouting pile section" can be obtained as follows:

$$Q_{ju} = \sigma_{ju}A_j = \sigma_{ju}D_j^2\frac{\pi}{4} = 8 \times 10^3 \times 0.6^2 \times \frac{\pi}{4} = 2260\text{kN}. \qquad (34)$$

We substitute equation (12), and $\gamma_c = 1.0$. The maximum bearing capacity of the jet grouting pile under the control of material strength is

$$R_2 = \gamma_c Q_{ju} = 1 \times 2260 = 2260\text{kN}. \qquad (35)$$

Therefore, according to equations (33) and (35), $R_1 < R_2$, so the "pure jet grouting pile" section of the composite foundation will not be damaged under the overall compression mode.

Based on the above (1) to (3), $R_i = 1051\text{kN} < R_t = 1600\text{kN}$, so the ultimate bearing capacity of the composite foundation under the overall compression mode is

$$R_c = R_i = 1051\text{kN}. \qquad (36)$$

5.4. Comparative Analysis of the Experimental Calculation of Vertical Compressive Bearing Capacity of the Composite Foundation. The comparison of measured and calculated bearing capacity of the composite foundation is shown in Table 4.

As can be seen from the table, under the overall compression mode, the measured test value of the bearing capacity of the composite foundation is 1083 kN. The calculated value determined by the calculation formula deduced under the assumed force distribution mode in this paper is 1051 kN, the absolute error between them is 32 kN, and the relative error is 3%. Therefore, both absolute error and relative error are very small. Therefore, the stress mode and calculation method of the jet grouting pile-mini steel pipe pile composite foundation proposed in this paper can meet the needs of engineering design and popularization and application of the composite foundation.

6. Conclusions

(1) Under the overall compression mode of the pile top of the composite foundation, the mini steel pipe pile and jet grouting pile jointly bear the upper load. According to the vertical force transmission characteristics of the composite foundation, the composite foundation can be divided into "inserted mini steel pipe pile section" and "pure jet grouting pile section" along the depth direction, and the jet grouting pile has "effective length." In the checking calculation of bearing capacity, the bearing performance of the mini steel pipe pile and jet grouting pile should be considered. Accordingly, the coordination effect of ultimate side friction resistance between the mini steel pipe pile and the jet grouting pile and ultimate side friction resistance between the jet grouting pile and soil should also be considered.

(2) The simplified hypothetical distribution diagram and calculation formula of interfacial friction resistance between the mini steel pipe pile and the jet grouting pile and interfacial friction resistance between the jet grouting pile and soil are put forward. The interfacial friction resistance between the mini steel pipe pile and the jet grouting pile presents a three-step distribution of small in the upper and large in the lower. The interfacial friction resistance between the jet grouting pile and soil generally presents a two-step distribution, and the ultimate side friction resistance at the upper part is less than that at the lower part.

(3) The mini steel pipe pile and the composite foundation can be regarded as pure friction piles, and the bottom axial force can be regarded as 0. According to the force transmission mechanism of the composite foundation, the calculation equation of the axial force of the composite foundation is established, the calculation formula of the axial force of the mini steel pipe pile and the jet grouting pile under the overall compression mode is deduced, and the axial force distribution diagram of the mini steel pipe pile and the jet grouting pile in the composite foundation is put forward.

(4) The calculation of the vertical compressive bearing capacity of the composite foundation is divided into the calculation of the ultimate bearing capacity controlled by the interface strength of the composite foundation and the calculation of the ultimate bearing capacity controlled by the material strength of the pile body of the composite foundation. The smaller of the two is taken as the ultimate compressive load of the composite foundation.

(5) The conclusions of this paper need to be further verified and improved by more engineering design examples.

Data Availability

The data supporting the conclusion of the article are shown in the relevant figures and tables in the article.

Conflicts of Interest

The authors declare that there are no conflicts of interest regarding the publication of this article.

Acknowledgments

References

[1] M. Aboutabikh, A. M. Soliman, and M. H. El Naggar, "Performance of hollow bar micropiles using green grout incorporating treated oil sand waste," *Journal of Building Engineering*, vol. 27, Article ID 100964, 2020.

[2] X. Liang, H. He, and Y. Zhang, "Optimization design of micro-piles in landslide safety protection based on machine learning," *Safety Science*, vol. 118, pp. 861–867, 2019.

[3] X. Li, Ming-Zhou Bai, M.-Z. Bai et al., "Application of carbon-fiber composite material in micropile structure," *Journal of Performance of Constructed Facilities*, vol. 34, no. 2, Article ID 04020017, 2020.

[4] J. Veludo, D. D. d. Costa, E. N. B. S. Júlio, and P. L. Pinto, "Bond strength of textured micropiles grouted to concrete footings," *Engineering Structures*, vol. 35, pp. 288–295, 2012.

[5] J. Veludo, E. N. B. S. Júlio, and D. Dias-da-Costa, "Compressive strength of micropile-to-grout connections," *Construction and Building Materials*, vol. 26, no. 1, pp. 172–179, 2012.

[6] F. Han, M. Prezzi, R. Salgado, and M. Zaheer, "Axial resistance of closed-ended steel-pipe piles driven in multilayered soil," *Journal of Geotechnical and Geoenvironmental Engineering*, vol. 143, no. 3, Article ID 04016102, 2017.

[7] N. Borthakur and A. K. Dey, "Evaluation of group capacity of micropile in soft clayey soil from experimental analysis using SVM-based prediction model," *International Journal of Geomechanics*, vol. 20, no. 3, Article ID 04020008, 2020.

[8] M. Khidri and L. Deng, "Field axial cyclic loading tests of screw micropiles in cohesionless soil," *Soil Dynamics and Earthquake Engineering*, vol. 143, p. 106601, 2021.

[9] M. T. Suleiman, L. Ni, J. D. Helm, and A. Raich, "Soil-Pile Interaction for a Small Diameter Pile Embedded in Granular Soil Subjected to Passive Loading," *Journal of Geotechnical and Geoenvironmental Engineering*, vol. 140, no. 5, Article ID 04014002, 2014.

[10] S. A. Davidow and D. G. Carr, "Micropile design and construction in a limited access wetland habitat," in *Proceedings of the Electrical Transmission and Substation Structures 2015*, pp. 35–45, Branson, Missouri, 2015.

[11] R. K. Gupta and S. Chawla, "Performance evaluation of micropiles as a ground improvement technique for existing railway tracks:finite-element and genetic programming approach," *International Journal of Geomechanics*, vol. 22, no. 3, Article ID 04021287, 2022.

[12] Z. Sun, L. Kong, and Y. Wang, "Seismic behaviour of a micropile-reinforced cut slope behind a cantilever retaining wall," *Soil Dynamics and Earthquake Engineering*, vol. 152, Article ID 107058, 2022.

[13] K. Boschi, Giulio di Prisco, C. G. di Prisco, and M. O. Ciantia, Micromechanical investigation of grouting in soils," *International Journal of Solids and Structures*, vol. 187, pp. 121–132, 2020.

[14] W. Zhang, Y. Li, A. T. C. Goh, and R. Zhang, "Numerical study of the performance of jet grout piles for braced excavations in soft clay," *Computers and Geotechnics*, vol. 124, Article ID 103631, 2020.

[15] A. M. Alnuaim, M. H. El Naggar, and H. El Naggar, "Performance of micropiled rafts in clay: numerical investigation," *Computers and Geotechnics*, vol. 99, pp. 42–54, 2018.

[16] H. Bayesteh, M. A. Fakharnia, and M. Khodaparast, "Performance of driven grouted micropiles: full-scale field study," *International Journal of Geomechanics*, vol. 21, no. 2, Article ID 04020250, 2021.

[17] L. Wen, G. Kong, Q. Li, and Z. Zhang, "Field tests on axial behavior of grouted steel pipe micropiles in marine soft clay," *International Journal of Geomechanics*, vol. 20, no. 6, Article ID 06020006, 2020.

[18] K. A. Kershaw and R. Luna, "Full-scale field testing of micropiles in stiff clay subjected to combined axial and lateral loads," *Journal of Geotechnical and Geoenvironmental Engineering*, vol. 140, no. 1, pp. 255–261, 2014.

[19] W. El Kamash, H. El Naggar, P. To, and N. Sivakugan, "The effect of long-term consolidation on foundations underpinned by micropiles in soft clay," *Ain Shams Engineering Journal*, vol. 13, no. 1, Article ID 101487, 2022.

[20] M. Esmaeili, M. Gharouni Nikand, and Farid Khayyer, "Experimental and numerical study of micropiles to reinforce high railway embankments," *International Journal of Geomechanics*, vol. 13, no. 6, pp. 729–744, 2013.

[21] M. S. Robison, "Excavation support and micropile underpinning in vail, Colorado," *GeoTrends*, pp. 112–118, 2010.

[22] K. Larsson and D. Jog, "Performance of micropiles used to underpin highway bridges," *Journal of Performance of Constructed Facilities*, vol. 28, no. 3, pp. 592–607, 2014.

Research Article

Dimension Measurement and Quality Control during the Finishing Process of Large-Size and High-Precision Components

Fei Lv [ID],[1] Chang'an Hu [ID],[2,3] Wenbo Du,[3] and Xi Wang[4]

[1]*Chengdu Normal University, Chengdu 611130, China*
[2]*Istitute of Optics and Electronics, Chinese Academy of Sciences, Chengdu 610209, China*
[3]*National Institute of Measurement and Testing Technology, Chengdu 610021, China*
[4]*Ningxia Lanson Precision Manufacturing Technology Co., Ltd, Wuzhong 751100, China*

Correspondence should be addressed to Chang'an Hu; huchangan19@mails.ucas.ac.cn

The accurate measurement and control of the geometric dimensions and shape errors of large-size and high-precision key components are key factor to ensure the machining quality of the equipment package. Aiming to address the urgent problems of poor measurement conditions, complicated error propagation, and difficulty in obtaining accurate measurement results, this research studied the measurement method and control of dimensional accuracy and geometric tolerance in the process of hole machining at room temperature, taking Metso MP 1250 cone level 6 precision point pair workpiece as the object. Through linear analysis and demonstration of quality problems in the existing processing technology, the influence of the expansion coefficient of the workpiece material, measurement error and other factors is analyzed. After correcting the temperature error model, many measurements were carried out in machining experiments, and the normal ability was analyzed by Minitab software. The experimental results showed that the workpiece temperature rises by 1°C, the workpiece will be deformed by 8.503 um. In the measurement process of high-precision and large-size components, the correction accuracy of the temperature error is affected by the combined influence of the model error, the material expansion coefficient error, and the temperature measurement error. The results of this study are of guiding significance for the measurement of the dimension and geometric tolerance precision of large-size and high-precision castings.

1. Introduction

The application of more high-tech has become an urgent and crucial task for the iterative upgrading of the machinery manufacturing industry. The focus of the manufacturing industry is shifting from hardware competition to software competition, from mechanization to intellectualization [1]. Comparing this development trend with the status quo of machining equipment and machining technology for large-size and high-precision components, it can be concluded that increasing the application of high-tech machining technology (especially in high-precision products) has become an inevitable demand for market development [2–5]. Large-scale mining machinery is a kind of power machinery whose cone is the key core component that burns fuel and directly converts heat energy into power. The accurate measurement and control

of geometric dimension and shape error of large-size and high-precision key parts is the key factor to ensure the processing quality of the whole set of equipment. The main shaft of the mining machine has a large structural size, high design accuracy and presents a cone shape. It is the main bearing component in the cone-shaped shell of the mining machine. The operation process is similar to the inner and outer rings of the sliding bearing and belongs to liquid dynamic pressure lubrication. Therefore, this requires high surface roughness and shape accuracy of the main shaft and its matched shell. In recent years, with the increasingly fierce market competition, improving the finishing quality of the cone of large mining machines has become a top priority for further developing related machinery manufacturing enterprises.

At present, scholars from many manufacturing companies and research institutions at home and abroad have

done a great deal of research on the key technology of mining machining cones [6, 7]. Based on experimental experiment system, Dogan et al. studied the physical requirements, structural characteristics, and technical requirements of the cone, analyzed the influence of stress-relief heat treatment process, welding process, and important cutting parameters (tool feed, cutting speed, etc.) on the quality of cone machining, and finally proposed a reasonable heat treatment method and machining process scheme for cone [8–11]. Mao et al. improved the structure of the flange cone. The flange was still formed by casting in his design, while the cone was manufactured by blanking and rivet welding. The two parts were welded at last, which not only saved raw materials and reduced the machining and manufacturing period, but also improved the overall quality of the flange cone [12]. Guo et al. applied virtual manufacturing technology to the machinery manufacturing process. They established the production process and production system model and virtual model, realizing the connection between the virtual manufacturing environment and the real manufacturing environment [13, 14]. It can be seen that both improving measuring tools and applying virtual manufacturing technology play an indispensable role in the machining of high-precision cones. Virtual simulation technology, comprehensively using the display and control technology of computer graphics system, can effectively improve the machining efficiency and quality. Given the related machining parameters of the machining object, the simulation optimized machining process can guide the actual machining process [15, 16].

From the perspective of MP1250 cone machining and manufacturing quality, the application of virtual manufacturing technology can effectively improve the quality of machining and optimize machining procedure, tool path, cutting parameters, blanking allowance and process structure, and reduce interference between fixtures and workpieces, and collision of machine tools, etc. [17, 18]. Applying the modular design method to the production process of remanufactured products can effectively reduce machining costs and improve the efficiency and accuracy of assembly [19]. Because different manufacturing companies have different processing places, changes of factory ambient temperature can affect the processing quality of high precision products [20], so the modular design is rarely applied in the research on machining cones of large mining machines. There are generally two measures to address this. One is to strictly control the temperature of the measured workpiece in a standard state [21]; the other is to correct the temperature error [22]. The first method requires high-precision measurement conditions, which is generally difficult to achieve, whereas the second is simple and easy to implement, and it is economical and applicable [23–25]. This suggests that the machining error control with temperature factors considered needs further research in high-efficiency machining technology, which is the significance of the present research.

In view of this, this research intended to take the Grade 6 precision spot facing work of Metso MP1250 cone as the object to study the measurement method and control of the dimensional accuracy and geometric tolerance of the high-precision spot facing work during machining. Based on the linear analysis and demonstration of quality problems existing in the existing machining process, this paper summarizes and analyzes the main factors affecting the machining quality of high-precision hole. Under the existing machining workshop environment and temperature conditions of the target enterprise, the influence of the expansion coefficient of the workpiece material, measurement error and other factors is analyzed. Before being used to guide on-site machining, the temperature error model was revised, and batches machining experiments were carried out to verify and determine reasonable machining methods and parameters, and to solve the problems of low machining efficiency and unstable quality. The research can provide a practical basis for the finishing process scheme of key parts with large size and high precision.

2. Analysis of Cone and Dimension Precision of GP Series Crusher

Metso GP series heavy cone crusher mainly comprises a frame, fixed cone, moving cone, spring mechanism, bowl-shaped shaft bracket, transmission parts, and auxiliary systems, as shown in Figure 1. When in operation, the motor drives the eccentric sleeve to rotate through the V-belt, large pulley, transmission shaft, a small bevel gear and bevel gear. The cone crusher axis rotates and swings under the force of the eccentric sleeve, so that the surface of the crushing wall approaches and leaves the surface of the rolling mortar wall. As a result, the material is continuously impacted, squeezed, and bent in the annular crushing cavity composed of the fixed cone and the movable cone until it is broken. The cone is one of the key components under great stress. It becomes the nodus during the machining due to its high precision and large size. Specifically, there are many holes, shafts, and keyway dimensions on the cone having transition fit and interference fit with small tolerance range, which are affected by the environmental factors of the machining plant, making it difficult to obtain accurate measurement values during the machining process, thus failing to meet technical requirements of assembly. Part of the design size of the cone is shown in Figure 2. In the process of machining, it is necessary to measure the process size of high-precision hole repeatedly. The basic dimension of the three holes are about $\varphi 1000$ mm, with the dimensional tolerance reaching IT5-IT6 precision, and the tolerances of radial runout and hole axis perpendicularity are both within 0.05 mm, as shown in Table 1.

3. Existing Machining Quality Problems

The research object of this paper is one of the businesses we have only carried out in recent years. Since the working hours of continuous processing of a cone reach 36 days. Through the statistical classification of 17 products with quality defects on-site, the main reasons for the quality problems of the products were summarized as shown in the following figure.

Figure 1: Structure diagram of cone crusher.
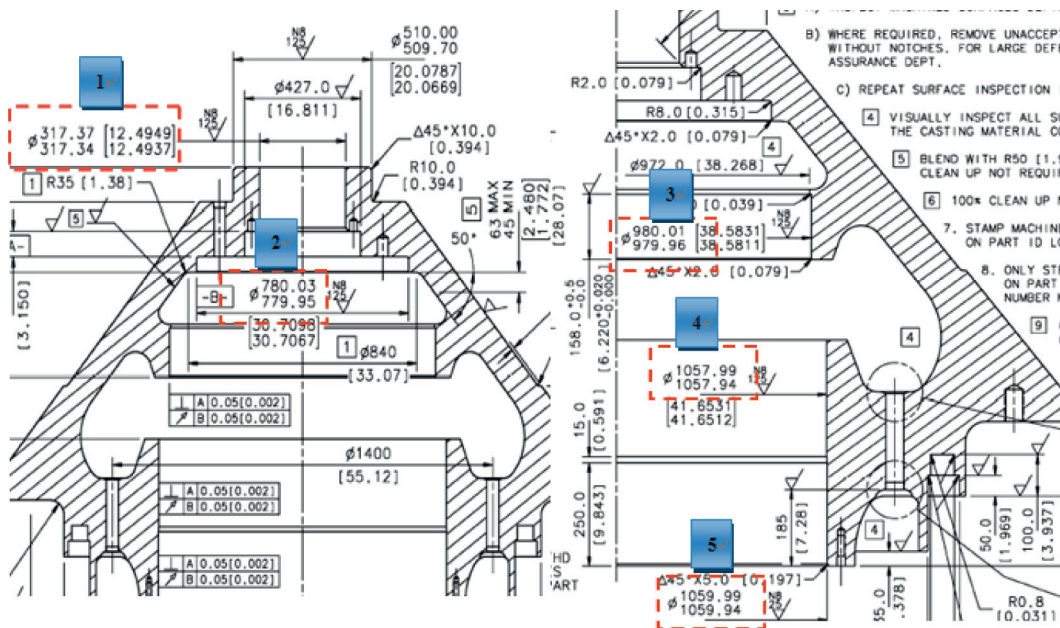
Figure 2: Dimensions of the cone structure.

Table 1: Dimension precision of high-precision holes.

SN	1	2	3	4	5
Drawing dimension (mm)	¢ 317.34	¢ 779.95	¢ 979.96	¢ 1057.94	¢ 1059.94
Tolerance range (mm)	0.03	0.08	0.05	0.05	0.05
Precision level	IT5	IT7	IT6	IT6	IT6

Linear analysis and field demonstration showed that indirect measurement was often adopted during the machining process due to the large diameter of the fine turning hole. The improper use of the measuring tool was one of the reasons for the measurement error. In contrast, the large size of the workpiece, high heat capacity, the unstable temperature at the site, temperature changes in the workpiece during machining, and the complex composite error propagation of the measuring tool under the influence of the temperature were the leading causes of the unstable measurement accuracy. It can be seen from Figure 3 that among the various defects that cause the unqualified cone machining, the excessive machining of the high-precision spot facing work was the main reason. Among the ten defective products with excessive spot facing work, nine products are due to the excessive machining along the diameter direction of the hole, and the rest is due to the excessive machining along the axial dimension, which is concentrated in the SN 3, 4, and 5 holes in Table 1. However, further analysis of the processing data on the processing record shows that the measured data before and after each processing are within the required size range.
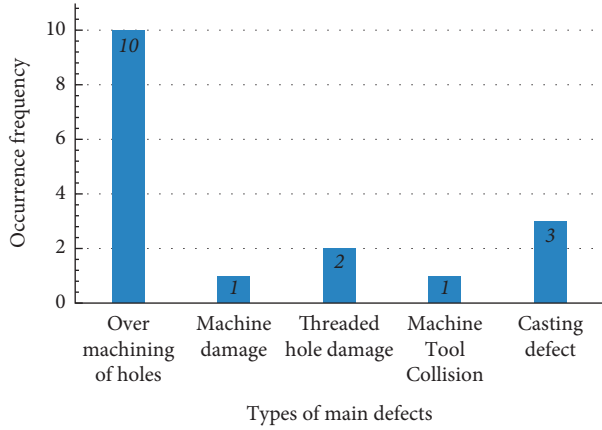
FIGURE 3: Analysis of quality problems during cone machining process.

4. Correction of the Temperature Error Model

Because the temperature affects the measurement results, the current correction method was to adjust the expansion coefficient of the material of the component, the relationship between the actual temperature, the standard temperature deviation, and the length of the component. That is, at the same temperature difference, the larger the nominal dimension of the measured workpiece, the more the temperature error increases, and the more sensitive it is to changes in temperature. The relationship between temperature and length can be expressed by the following functional equation:

$$\Delta L = L\,\alpha\,(t - 20). \tag{1}$$

Where, ΔL is the dimensional change, L is the nominal dimension of the measured workpiece, α is the coefficient of linear expansion of the object ($1/°C$), t is the temperature of the object ($°C$).

From equation (1), it can be seen that the dimensional change of the measured workpiece is proportional to the temperature difference with the standard temperature of $20°C$ and the nominal dimension of the workpiece. Therefore, ΔL is also called the temperature error correction value.

This modified model can meet the requirements when applied to small-size or low-precision measurement occasions, and the error after the correction can be ignored. However, for the high-precision measurement of large-size workpieces, the residual error after the correction still significantly impacted the precision. Therefore, based on the precision analysis, corresponding precision assurance measures were proposed to ensure high-precision measurements for large-size workpieces. The main factors affecting the accuracy of temperature error include the error of the temperature error correction model, the linear expansion coefficient of the material, temperature measurement error and so on. In addition, considering the large fluctuation of ambient temperature in the processing plant, the influence of temperature gradient on the measurement accuracy is also included.

Under a uniform temperature field of the measured workpiece, the temperature error correction value can be obtained through the following equation:

$$\Delta L = L\left(\alpha\Delta t + \beta\Delta t^2\right), \tag{2}$$

where α is expansion coefficient of the material, β is the secondary expansion coefficient of the material, and for commonly used materials, $\beta \leq 10^{-7}/°C$. Compared with equation (1), it can be seen that the traditional error correction formula is an approximate formula obtained by ignoring the above quadratic items. Because the thermal expansion coefficient of the higher-order term was very small, and expansion coefficients might be positive or negative, it can offset some deformation error. The formula was simplified as shown in equation (2). Thus, the error caused by the linearization of the temperature error correction model can be obtained as

$$\delta_m = L\,\beta\Delta t^2. \tag{3}$$

Then, the maximum uncertainty component μ_1 caused by the error of temperature error correction model can be expressed as

$$\mu_1 = L\left|\beta\Delta t^2\right|. \tag{4}$$

As can be seen from the above equation, the measurement uncertainty caused by the error of the temperature error correction model increased with the increase of the nominal dimension of the measured workpiece and the rise of the temperature. On the other hand, the measurement of temperature error also had a great influence on the measurement accuracy of large-sized workpiece. Assuming that the temperature measurement uncertainty is $\mu_{\Delta t}$, then the measurement uncertainty μ_2 caused by the temperature measurement error can be expressed as

$$\mu_2 = \left|\frac{\partial\Delta L}{\partial\Delta t}\right|\mu_{\Delta t} = L\,\partial\Delta t. \tag{5}$$

The same conclusion can be obtained: μ_2 increases with the increase of the measured dimension, the coefficient of linear expansion, and the uncertainty of the measured temperature.

The current expansion coefficients of various materials provided in the engineering manual were the evaluation values of the material expansion coefficients obtained from the thermal deformation test within a large range of temperature on round bar specimens with a certain diameter-length ratio. Compared with the research object, the evaluation value is uncertain. Assuming the measurement uncertainty caused by the error of the material expansion coefficient is u_3, it can be expressed as

$$\mu_3 = \left|\frac{\partial\Delta L}{\partial\alpha}\right|\mu_0 = L|\Delta t|\mu_0. \tag{6}$$

Where, μ_0 is the uncertainty of the material, usually being $2 \times 10^{-6}/°C$.

When measuring the large-size workpieces studied in this paper, the differential expansion coefficient of the measured component material should be determined first,

and then use this coefficient to correct the temperature error. Using this diagram, the error of the temperature error correction model can be compensated in the accurate determination of the expansion coefficient, which significantly reduced the uncertainty of measurement caused by temperature changes. In summary, the temperature error correction model in the measurement of a large-size workpiece can be expressed as

$$\Delta L = L\left(a_{t2}t_2 + a_{t1}t_1\right). \tag{7}$$

Because the cone material of this research object was mainly alloy steel, the $\varphi 1057.94$ mm fine turning hole in Figure 2 was taken as an example. According to the actual temperature of the machining site, the following values were taken after calculating as per the applicable temperature range and checking the engineering manual:

$$\begin{aligned}
t_2 &= 19.85°C, \\
a_{t2} &= 8.0342 \times 10^{-5}\,\mu m, \\
t_1 &= 9.84°C, \\
a_{t2} &= 8.0334 \times 10^{2}\,\mu m.
\end{aligned} \tag{8}$$

Then, at the first temperature gradient,

$$\begin{aligned}
\Delta L_1 &= L\left(a_{t2}t_2 + a_{t1}t_1\right) = 85.090\,\mu m, \\
\frac{\Delta L_1}{\Delta t} &= L\left(a_{t2}t_2 + a_{t1}t_1\right) = \frac{8.500\,\mu m}{°C}.
\end{aligned} \tag{9}$$

Similarly, at the second temperature gradient, the following values were taken:

$$\begin{aligned}
t_2 &= 29.90°C, \\
a_{t2} &= 8.0351 \times 10^{-5}\,\mu m, \\
t_1 &= 19.85°C, \\
a_{t2} &= 8.0342 \times 10^{2}\,\mu m.
\end{aligned} \tag{10}$$

It was obtained that

$$\begin{aligned}
\Delta L_2 &= L\left(a_{t2}t_2 + a_{t1}t_1\right) = 85.454\,\mu m, \\
\frac{\Delta L_2}{\Delta t} &= L\left(a_{t2}t_2 + a_{t1}t_1\right) = \frac{8.503\,\mu m}{°C}.
\end{aligned} \tag{11}$$

After comparing with the above calculation results, it was found in the in-process measurement of the research object, every $1°C$ increase in casting temperature would cause $8.503\,\mu m$ dimensional deformations of the casting. Therefore, in the actual machining of the cone casting, the casting temperature must be measured to compensate for the effect of temperature on the dimensional measurement.

5. Improvement and Implementation of Measurement Scheme

In order to avoid the influence of the operator's body temperature on the measuring tool and the errors caused by the expansion of the measuring tool due to the hand temperature, gloves with good heat insulation ability should be worn when measuring, with the hand holding the tool no more than 2 min. Therefore, a special measuring tool was designed for cone alignment and quick measurement, as shown in Figure 4.

This tooling includes a handle, a laser generator (the red line refers to the laser beam), the body, the high progress reference guide rail on the back of the body, and an adjusting screw. The adjusting screw can adjust the upper and lower positions of the laser. The supporting surface is in contact with the processing surface of the workpiece, and the supporting surface can be changed into a circular one (measuring coaxially). The horizontal and numerical distance between the laser beam and the adjacent surface is determined. If the height deviation between two distant surfaces is measured, the tooling will contact one side and the laser beam will hit the other side. Therefore, measuring the distance between the laser beam and the surface will measure the distance between the two surfaces.

The specific implementation steps were as follows:

(a) After machining is completed, place the workpiece to be tested for more than 30 minutes, so that its temperature is the same as the ambient temperature. As shown in Table 2, the variation of the factory ambient temperature with time on a certain day during the measurement process was obtained.

(b) After measuring the current temperature of the measured workpiece and combining the above compensation conclusion, the gradual deformation compensation at the current temperature was calculated.

(c) The current dimension of the workpiece to be measured was measured through the repetitive measurement method, i.e., each point was measured in no less than three groups, each group no less than three times, and the average value was taken as the final result of the measurement point.

(d) The final dimension of the object to be measured was determined. According to the principle of obtaining the sum of the inner diameter difference and the outer diameter of the hole, after calculating the size value and deformation compensation value of the workpiece at the current temperature, the final size of the object to be measured was determined. The compensation relationship was obtained as shown in Table 3. The machining results of a ϕ 1057.94 mm spot facing work were measured. The errors were obtained through a comparison between different measurement results of different batches and the drawing results, as shown in Figure 5.

Measurements were performed according to the above requirements, and the measurement data were organized and recorded after completion, according to the Bessel formula:
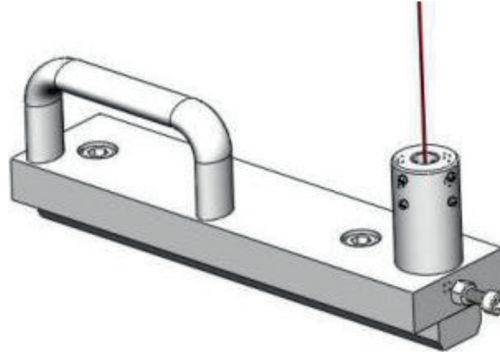
FIGURE 4: Laser alignment measurement tool.

TABLE 2: Time-varying temperature in plant environment (September).

Temperature (°C)	21.5	19	20	24	25	26	24	23
Time (h)	00 : 00	03 : 00	06 : 00	09 : 00	12 : 00	15 : 00	18 : 00	21 : 00

TABLE 3: Measured dimension compensation.

In situ temperature (°C)	19	20	21	22	23	24	25	26
Inner diameter compensation (μm)	+8.503	0	−8.503	−17.006	−25.509	−34.012	−42.515	−51.018
Outer diameter compensation (μm)	−8.503	0	+8.503	+17.006	+25.509	+34.012	+42.515	+51.018
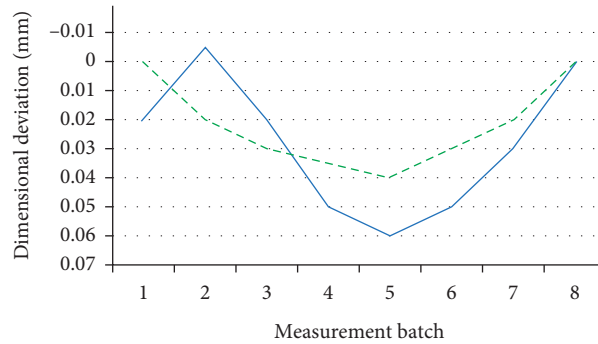
FIGURE 5: Dimensional deviation among different measurements.

$$S = \sqrt{\frac{\sum_1^i (x - x_i)^2}{i - 1}}. \tag{12}$$

Calculate the standard deviation of the experiment, and according to the principle of maximum error, eliminate the result that the reading deviates from the average value by more than 3 times. The Minitab software was used to carry out statistical analysis of normal capacity and process capability analysis. Taking the ϕ 1057.94 mm hole as an example, its normal capacity distribution was obtained, as shown in Figure 6.

The method of normal capability analysis is used to evaluate the potential (intragroup) capability and overall capability of the process according to the normal distribution. In this analysis, the following operations are mainly performed: determine whether the process can generate output that meets the processing requirements. Compare the overall capability of the process with its potential (in

group) capability to assess opportunities for improvement. When performing the analysis, specify the lower or upper specification limit, the limit size of the current machined hole, to define the process requirements. This analysis will be relative to the expansion of the specification limit evaluation process data. When the process is capable, the process expansion is less than the specification expansion. This analysis can also indicate whether your process is centered and reaches the target value. In addition, this analysis will estimate the ratio of products that do not meet the specifications.

Multiple sets of measurement results of holes with a machining target of ϕ 1057.94 mm showed that the measurement process was in a steady-state, and 99.73% of the characteristic values of the processed objects were scattered in the interval $[\mu - 3\sigma, \mu + 3\sigma]$. In other words, almost all product characteristic values fall within the range of 6σ, indicating that the measurement evaluation process capacity was consistent with the specified requirements.

Process capability analysis of 1057.94 (0°)

Process data	
LB	1057.94
No.	*
UB	1057.99
Sample mean	1057.95
Sample N	13
SD (in)	0.0302157
SD (all)	0.0255526

in
all

Ability (in)	
CP	*
CPL	*
CPU	*
CPK	*

Ability (all)	
PP	*
PPL	*
PPU	*
PPK	*
CPM	*

1057.88 1057.90 1057.92 1057.94 1057.96 1057.98 1058.00 1058.02

Measured performance		E P (in)		E P (all)	
PPM < Min	307692.31	PPM < Min	*	PPM < Min	*
PPM > Max	0.00	PPM > Max	*	PPM > Max	*
SUM PPM	307692.31	SUM PPM	*	SUM PPM	*

Figure 6: Normal capability distribution.

6. Conclusion

In the measurement process of large-size, high-precision components, the correction accuracy of the temperature error is affected by the combined influence of the model error, the material expansion coefficient error, and the temperature measurement error.

A comparison of the results of several measurements and calculations showed that every $1°C$ increase in casting temperature would cause a deformation of 8.503 um to the casting dimension. In the actual casting process, the casting temperature must be measured to compensate for the effect of temperature on the dimension measurements.

According to the corrected error model and measurement compensation values, the measurement process capability of the measured object completed by the improved measurement scheme showed that the measurement process was in a stable state and the measurement process capability is sufficient to meet the machining quality. The results of this study provide guidance for carrying out precision measurement of the dimension and geometric tolerance of large-size, high-precision castings.

Data Availability

The data used to support the findings of this study are included within the article.

Conflicts of Interest

The authors declare that they have no conflicts of interest.

References

[1] S. Liu, J. Bao, Y. Lu, J. Li, S. Lu, and X. Sun, "Digital twin modeling method based on biomimicry for machining aerospace components," *Journal of Manufacturing Systems*, vol. 58, 2020.

[2] K. Berggren, Q. Xia, K. Likharev et al., "Roadmap on emerging hardware and technology for machine learning," *Nanotechnology*, vol. 32, 2020.

[3] M. Shafique, T. Theocharides, C. S. Bouganis et al., "An overview of next-generation architectures for machine learning: roadmap, opportunities and challenges in the IoT era," in *Proceedings of the 2018 Design, Automation & Test in Europe Conference & Exhibition (DATE)*, Dresdan, Germany, March 2018.

[4] H. Qi, S. Qin, Z. Cheng, Q. Teng, T. Hong, and Y. Xie, "Towards understanding performance enhancing mechanism of micro-holes on K9 glasses using ultrasonic vibration-assisted abrasive slurry jet," *Journal of Manufacturing Processes*, vol. 64, pp. 585–593, 2021.

[5] S. Li, J. Zhang, Y. Tang, J. Yin, and W. Zhao, "Modeling of mapping relationship between part machining error and machine tool geometric error," *Journal of Xi'an Jiaotong University*, vol. 55, no. 10, pp. 50–59, 2021.

[6] A. Keski-Koukkari, J. Rekola, A. Kulmala, R. Juntunen, K. Maki, and M. Valtee, "Methodology to analyze effect of electric mining machines on the mine grid," in *Proceedings of the 2020 IEEE Transportation Electrification Conference & Expo (ITEC)*, Chicago, USA, June 2020.

[7] N. Varshney, C. Janarthanan, P. Muthuvel, N. R. Ramesh, C. R. Deepak, and M. A. Atmanand, "Virtual modelling and navigation controls of underwater mining machine," in *Proceedings of the Ocean Electronics (SYMPOL), 2013*, Kochi, India, October 2013.

[8] A. Dogan and D. Birant, "Machine learning and data mining in manufacturing," *Expert Systems with Applications*, vol. 166, no. 2, Article ID 114060, 2021.

[9] D. Wu, H. Wang, and J. Yu, "Research on machining error transmission mechanism and compensation method for near-net-shaped jet engine blades CNC machining process," *International Journal of Advanced Manufacturing Technology*, vol. 117, no. 1, pp. 1–19, 2021.

[10] L. Tian, *Machining Error Analysis and Experimental Research of High Precision star Sensitive Support*, Beihua Institute of Aerospace Technology, Coimbatore, India, 2021.

[11] Y. Hu, T. Li, H. Qun, and C. Xu, "Machining error measurement of aspheric Vertex Curvature Radius Based on partially compensated interference," *Journal of metrology*, vol. 41, no. 8, pp. 903–908, 2020.

[12] P. H. Mao, J. X. Li, and L. Ding, "The GREEN design of horizontal type transfer machine for underground coal mine belt department," *Advanced Materials Research*, vol. 591–593, pp. 80–83, 2012.

[13] D. Guo, J. Bao, G. Shi et al., "Research on modeling of aerospace structural parts manufacturing workshop based on digital twin," *Journal of Donghua University*, 2018.

[14] W. Komatsu and K. Nakamoto, "Machining process analysis for machine tool selection based on form-shaping motions," *Precision Engineering*, vol. 67, pp. 199–211, 2021.

[15] P. A. Dreyfus, F. Psarommatis, G. May, and D. Kiritsis, "Virtual metrology as an approach for product quality estimation in Industry 4.0: a systematic review and integrative conceptual framework," *International Journal of Production Research*, vol. 60, Article ID 1976433, 2021.

[16] M. Liang, C. Yang, X. Liu, and Y. Xia, "Tang Qiang in situ compensation technology of machining error of ultra precision machine tool based on micro tool holder," *Journal of Jilin University (Science Edition)*, vol. 50, no. 6, pp. 2019–2027, 2020.

[17] K. Hyun Baek, K. Song, C. Han, G. Choi, H. Ku Cho, and T. F. Edgar, "Implementation of a robust virtual metrology for plasma etching through effective variable selection and recursive update technology," *Journal of Vacuum Science & Technology B, Nanotechnology and Microelectronics: Materials, Processing, Measurement, and Phenomena*, vol. 32, no. 1, Article ID 012203, 2014.

[18] H. Cai, J. Feng, Q. Yang, W. Li, X. Li, and J. Lee, "A virtual metrology method with prediction uncertainty based on Gaussian process for chemical mechanical planarization," *Computers in Industry*, vol. 119, Article ID 103228, 2020.

[19] T. Liu, G. Liu, S. Song, and J. Zhao, "Product modular design for active remanufacturing," *Chine Mechanical Engineering*, vol. 10, pp. 1180–1187, 2012.

[20] D. Wu, H. Wang, and J. Yu, "Machining errors control method for near-net-shape jet engine blade CNC machining process," *Journal of Physics: Conference Series*, vol. 1885, no. 2, Article ID 022006, 2021.

[21] Z. Ren, L. Shen, and H. Bai, "Study on the mechanical properties of metal rubber with complex contact friction of spiral coils based on virtual manufacturing technology," *Advanced Engineering Materials*, vol. 22, no. 8, pp. 1012–1021, 2020.

[22] Y. Torun and H. Dogan, "Modeling of Schottky diode characteristic by machine learning techniques based on experimental data with wide temperature range," *Superlattices and Microstructures*, vol. 160, 2021.

[23] W. Shi, "Influence of mechanical manufacturing process on machining accuracy," *Modern Industrial Economy and Informationization*, vol. 11, no. 8, pp. 174-175 + 178, 2021.

[24] Z. Jin, "Measurement process and uncertainty evaluation of climate chamber," *Advanced Measurement and Laboratory Management*, vol. 13, no. 3, p. 3, 2005.

[25] H. Jeong and C.-M. Lee, "A study on improvement of tool life using a heat shield in laser assisted machining to Inconel 718," *Optics & Laser Technology*, vol. 142, 2021.

Research Article

Optimization of Networked Governance Models Using Complex System Governance Concepts in Sports Services

Yuhua Gao [ID],[1] **Xinxi Zhen,**[1] **and Yan Xiong**[2]

[1]*Guangzhou Sports University, Guangzhou, Guangdong, China*
[2]*College of P.E. & Sports Science, Guangzhou University, Guangzhou, Guangdong, China*

Correspondence should be addressed to Yuhua Gao; 11071@gzsport.edu.cn

In order to increase the participation rate of community residents in sports services, on the governance concept of a complex system, the networked governance model under sports services has been studied. Firstly, by introducing the background of networked governance, the supply of sports services is selected as the research object. The selected sports service providers are the government, universities, enterprises, associations, and residents. Secondly, the structural model of sports service supply has been constructed. Combining the direct effects model and the intermediary relationship model, the questionnaire is designed. The current situation of sports service supply in the study area is analyzed. Finally, on this basis, the networked governance model strategy has been optimized. The results show that because the age distribution of the subjects is relatively young, the residents in the study area have a higher degree of understanding of sports services. In the direct relationship model and the mediating effect model, the 6 fitting indicators are consistent with the standard values, and no abnormal data appeared. The government, universities, and associations have a significant influence on the supply of sports services. The impact of enterprises and residents on the supply of sports services is not significant. The community environment plays an intermediary role in the supply of residents and sports services, and the supply of enterprises and sports services. Network governance should pay more attention to the participation of multiple subjects, change the leading role of the government, break down the communication barriers between supply subjects, establish an information security mechanism, and build an information sharing system. The research results provide a reference direction for the development of network management in sports services.

1. Introduction

Sports services refer to people who have certain professional knowledge, skills, and experience in sports. These people can be engaged in the production of sports services [1]. And they carry out purposeful activities to produce the special use value of this sports service [2, 3]. With the acceleration of urbanization, the living functions of urban communities have become the core of community construction [4], and the construction of healthy urban communities is closely related to the rationality of the layout of sports service resources [5, 6]. China's current development requirements are to modernize the country's governance capabilities and realize the country's governance system. Since the twenty-first century, Internet technology has developed rapidly, and

networked governance can integrate and mobilize social multiresources through public entities and existing public interest needs to deal with complex social situations [7, 8].

The United States is the first to research on sports public services. In 2010, the US government clearly proposed to improve the physical fitness of residents [9]. The United Kingdom, Germany, Japan, and Australia have also promulgated related bills and made certain rules and regulations for sports services [10, 11]. China's research on networked governance is on meeting China's actual needs, so it has certain Chinese applicability [12, 13]. For example, researchers used a widely defined network-based framework to track the evolution of urban renewal decisions in Guangzhou, China, and learned from the concept of network governance to obtain China's ever-developing urban

regeneration policies and a broader governance network in urban regeneration practices [14]. Network governance goes beyond grid governance and gives market management more vitality [15].

At this stage, the participation rate of residents in community sports services is low in China. Therefore, the research combines the concept of complex system governance to conduct in-depth exploration on the supply of community sports services. The purpose is to solve the problems exposed in sports services at this stage and implement a sports service network model that is more in line with the current urban development in China. The innovative point lies in the integration of networked governance into the supply of community sports services, combining the different levels of networked governance with the characteristics of the supply of community sports services, and proposed existing targeted networked governance measures. The research has made a certain contribution to promoting national governance capacity and governance system, innovation, and strengthening the construction of social governance system.

2. Research Method of Optimizing Networked Governance Model

The community sports service in a province of China is selected as the research object. Since community services are mainly public services, the research is mainly about the optimization of networked governance models under sports public services. Firstly, the research introduces the background. Secondly, it analyses the status quo of sports services in the study area by taking the supply relationship of sports services as the breakthrough point. Finally, on this basis, optimization measures are proposed for networked governance.

2.1. Implementation of Sports Service Supply Structure Model. The supply subjects of the study area are divided into five categories, including government, universities, enterprises, community residents, and associations, as variables in the sports service supply model, shown in Figure 1.

Figure 1 shows that among these five main bodies, the government plays a guiding and supporting role. The enterprise also has advantages in sports services, and the business principles of the enterprise require the enterprise to continuously iterate its products and services. As the main body of providing social services and transporting talents to the society, colleges and universities radiate intelligence and human resources to the surrounding communities. As a participant of the main body of supply, the association is an innovative measure to improve the way of sports service [16]. As the main body of supply, community residents are also demanders of sports services [17].

The specific content of the community environment is shown in Figure 2.

Figure 2 shows that among the three main parts of the community environment, the community political environment refers to the interactive relationship between the

state and the community, and the relationship between the democratization of community politics and political construction. The process of community residents' participation in decision-making is mainly reflected in the expectations of managers for their own roles [18]. The community development environment is the overall level of community development and innovation. The community service environment includes medical and health, cultural propaganda, traffic environment, etc. [19].

Sports service supply is an important part of China's social system and social structure. The elements of sports service supply include sports service infrastructure and service scale to meet the needs of physical exercise, the sports service management system is perfect and the supply organization is set up reasonable, and the sports service supply capacity is on the rise [20, 21].

The research sets 5 direct hypotheses and 11 indirect hypotheses, as shown in Table 1.

Table 1 shows that the direct hypothesis here is mainly the hypothesis of the relationship between the supply of sports services and the five supply entities. The indirect hypothesis is mainly the hypothesis of the relationship between the five supply entities and the community environment, as well as the community environment and sports supply.

Implement a conceptual model of the influence relationship and path between the main body of sports service and service supply, as shown in Figure 3.

The basic structure in Figure 3 is used to analyze the path of influence between the supply of sports services and the main body of the service. The conceptual model is verified by a questionnaire, and the results of the questionnaire will provide theoretical support for the sports service supply model.

The questionnaire set up is divided into four parts, including the basic information of the respondent, the main elements of the surveyor's provision of sports services (18 test questions), the community environment (8 test questions), and the sports service degree of approval (3 test questions). The evaluation adopts the 5-level scoring method of the Likert scale [22], with 1–5 indicators, which represent "very disagree," "disagree," "general," "agree," and "very agree," respectively. 209 questionnaires were distributed, and 193 valid questionnaires were recovered, with an effective rate of 92.3%. The questionnaire distribution method is a combination of online and offline. Analysis of Moment Structure 21.0 and Statistical Product and Service Solutions 26.0 data analysis tools are adopted here.

The specific items of the questionnaire are shown in Table 2.

In the descriptive analysis of the questionnaire, basic information includes gender, age, education level, occupation, and average monthly income. Among them, the age is divided into 18 years old, 18–35 years old, 36–45 years old, 46–60 years old, and 60 years old and above; education level is divided into junior high school and below, high school or college, undergraduate, master, and doctor and above; occupations are divided into civil servants and public institutions, corporate personnel, freelancers, retirees, and
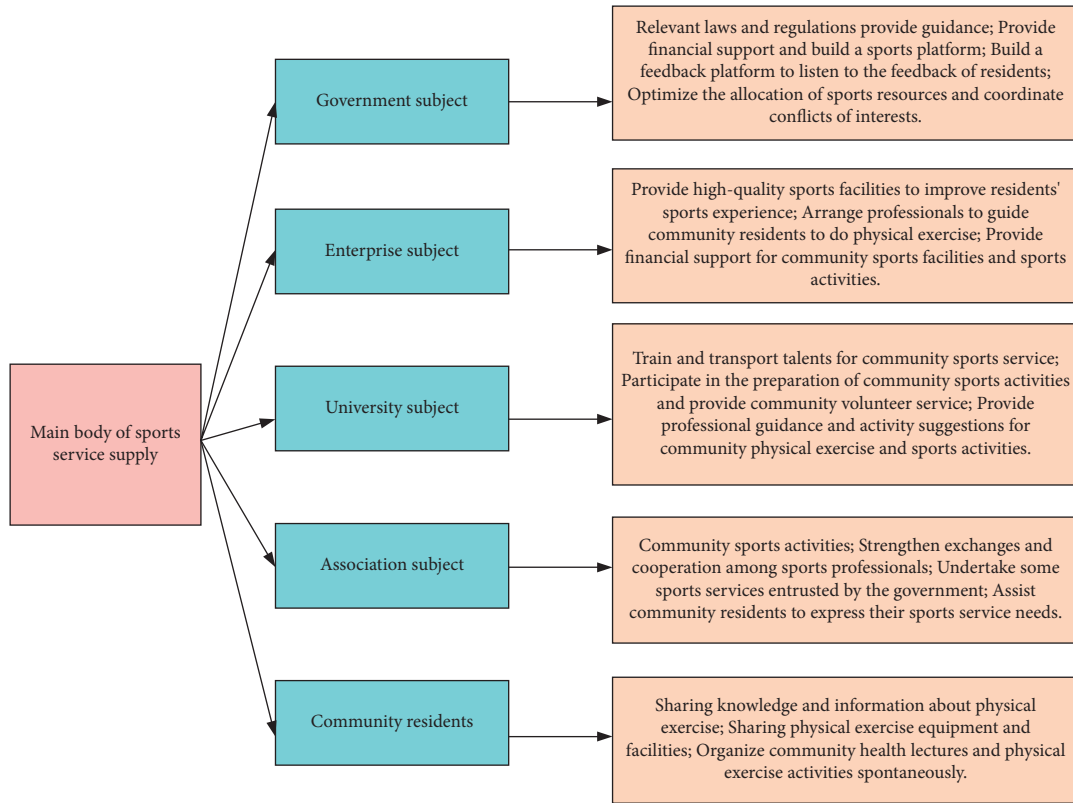
FIGURE 1: The main supply body of sports service.
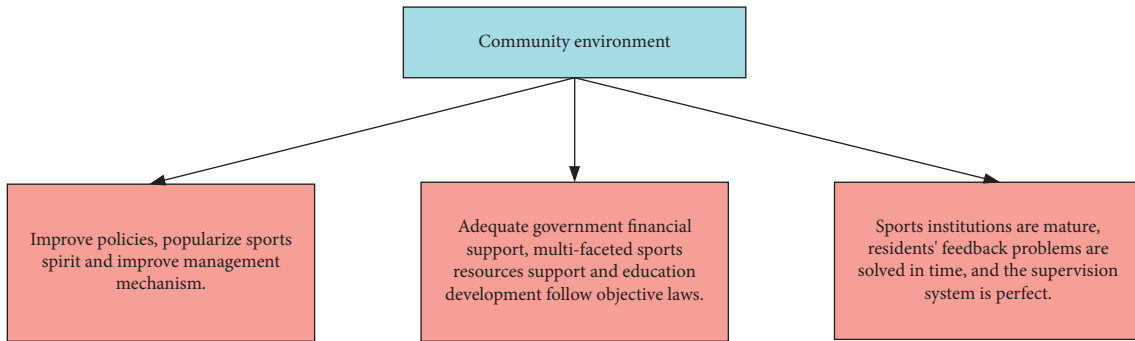
FIGURE 2: The elements of the community environment.

others; the average monthly income is divided into 3000 yuan or less, 3000–5000 yuan, 5001–8000 yuan, 8001–10000 yuan, and 10000 yuan or more. 1–5 represent 5 divided areas.

The reliability test of the scale is carried out by Cronbach's α [23]. If the value of α is less than or equal to 0.7, the internal consistency of the scale is unacceptable. The calculation of Cronbach's α is expressed as

$$\alpha = \left(\frac{k}{k-1}\right) \cdot \left(1 - \frac{\sum S_i^2}{S_T^2}\right). \tag{1}$$

In Eq. (1), k is the number of question items of the survey target, S_i^2 is the variance of the i-th question of all respondents, and S_T^2 is the variance of the sum of the answers to all the question items. Among them, the calculation of variance S_T^2 is as follows:

$$S_T^2 = \frac{\sum (T - \mu)^2}{N}. \tag{2}$$

In Eq. (2), T is the variable, μ is the overall mean, and N is the number of overall cases.

The evaluation of the reliability of a single index uses Corrected Item-Total Correlation (CITC) and the revised item [24]. The definition of CITC is shown as follows:

$$v(I, J) = \frac{\text{Cov}(I, J)}{\sqrt{\text{var}[I]\text{var}[J]}}. \tag{3}$$

TABLE 1: Research hypothesis.

Hypothetical type	Hypothetical number	The specific content of the hypothesis
Direct hypotheses	S1a	Sports services are significantly affected by government entities
	S2a	Sports services are significantly affected by the main body of the enterprise
	S3a	Sports services are significantly affected by the main body of colleges and universities
	S4a	Sports services are significantly affected by the main body of the association
	S5a	Sports services are significantly affected by residents
Indirect hypotheses	S1b	The community environment is significantly affected by the government
	S2b	The community environment is significantly affected by business entities
	S3b	The community environment is significantly affected by the main body of the university
	S4b	The community environment is significantly affected by the main body of the association
	S5b	The community environment is significantly affected by the residents
	S6	Sports services are significantly affected by the community environment
	S6a	The community environment plays an intermediary role between sports services and the supply of government entities
	S6b	The community environment plays an intermediary role between the sports service and the supply of the main body of the enterprise
	S6c	The community environment plays an intermediary role between sports services and the supply of the main body of colleges and universities
	S6d	The community environment plays an intermediary role between the sports service and the supply of the main body of the association
	S6e	The community environment plays an intermediary role between sports services and the supply of residents
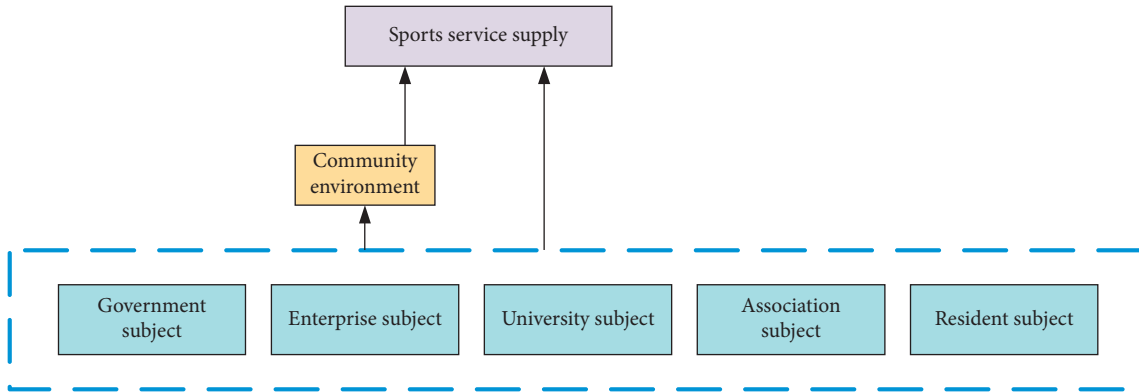
FIGURE 3: Supply conceptual model of sports service.

In equation (3), $\text{Cov}(I, J)$ is the covariance and var refers to the variance, which must be greater than 0.5. When the CITC value and α value of the observed variable and the latent variable do not meet the requirements, they need to be revised or deleted [25]. Reliability analysis includes the analysis of the supplier, the community environment, and the supply of sports services.

The validity analysis is carried out from the aspect of construct validity [26]. Kaiser–Meyer–Olkin (KMO) and Bartlett sphere test are used to determine whether the questionnaire data can be used for factor analysis. The specific equations of KMO and Bartlett sphere test are expressed as (4)–(6).

$$KMO = \frac{BB}{AA + BB}. \tag{4}$$

In equation (4), AA is the sum of squares of the partial correlation coefficients between the two in all variables and BB is the sum of squares of the correlation coefficients between the two in all variables. When KMO value > 0.8, the data is good.

$$X^2 = -\left(n - \frac{2p + 11}{6}\right)\ln|R|, \tag{5}$$

$$df = \frac{p(p - 1)}{2}. \tag{6}$$

Equations (5) and (6) are the calculation process of the statistics in the Bartlett test of sphericity. Among them, n is the number of data records, p is the number of variables in the factor analysis, and $|R|$ is the determinant of the correlation coefficient matrix R value.

The average variance extraction method (AVE) and the topic factor loading coefficient method are used to measure the convergence validity of the questionnaire data [27], and the specific expressions are shown in equations (7) and (8).

TABLE 2: Questionnaire specific items.

Latent variable	Index number	The specific content of the topic
Government entities	Z1	Policy guidance such as laws and regulations
	Z2	Financial support
	Z3	Build a feedback platform
	Z4	Optimize resource allocation and coordinate conflicts
The main body of colleges and universities	G1	Provide voluntary services for sports services
	G2	Provide venue and facility support
	G3	Provide professional guidance
	G4	Carry out diverse exchanges
The main body of the enterprise	Q1	Provide high-quality facilities
	Q2	Arrange professional guidance
	Q3	Provide financial support
The main body of the association	X1	Carry out several sports exchange activities
	X2	Communicate with professionals in sports
	X3	Undertake government-entrusted sports activities
	X4	Assist in responding to the needs of the masses
Residents	J1	Physical exercise information and knowledge sharing
	J2	Facilities and equipment sharing
	J3	Spontaneous organization of sports activities
The community environment	H1	Improve laws and regulations and popularize sportsmanship
	H2	Improve management service mechanism
	H3	The government provides sufficient financial support
	H4	Obtain multiple sports resources
	H5	Possesses the potential for sports development
	H6	Sports service agencies are mature
	H7	Residents can get timely feedback on problems
	H8	Improve the supervision system
Sports service supply	T1	Physical exercise needs can be met by infrastructure and sports services
	T2	The supply of sports products is on the rise
	T3	The sports service management system is perfect, and the supply organization is set up reasonably

$$AVE = \frac{\sum_{i=1}^{n} Li^2}{n}, \tag{7}$$

$$A = \left(\sqrt{\lambda_1 \eta_1}, \sqrt{\lambda_2 \eta_2}, \cdots, \sqrt{\lambda_m \eta_m} \right). \tag{8}$$

Equation (7) is the calculation equation of the average extraction variance method. Among them, Li^2 is the variance and n is the number of terms. In equation (8), λ is the eigenvalue of the correlation coefficient, η is the corresponding normalized eigenvector, and m is the number of terms. For items that require high factor loading in the measurement model, the average extraction variance should be no less than 0.5, and the combined reliability of the latent variables should be no less than 0.7. Finally, the discriminative validity analysis is performed, and the correlation coefficient between the square root factors of the average extracted variance value is used to evaluate the relationship [28]. Both the construct validity and the convergence validity are greater than 0.5, indicating that the validity is good.

After the direct relationship model and the intermediary relationship model are implemented, they are evaluated. The evaluation method uses the fit of the model to check whether the fit index meets the requirements and obtain the result of the model path verification. Model testing also includes Bootstrap mediation effect testing, which mainly tests the

influence relationship between the outcome variable and the antecedent variable [29, 30]. The model fitting index and the core calculation equation in Bootstrap are shown in equations (9) and (10).

$$X^2 = \sum_{i=1}^{k} \frac{(O_i - T_i)^2}{T_i}. \tag{9}$$

In equation (9), k is the number of groups, O is the observation frequency, and T is the theoretical frequency.

$$\overline{X} - t \frac{s}{\sqrt{n}} < \mu < \overline{X} + t \frac{s}{\sqrt{n}}. \tag{10}$$

Equation (10) is the calculation of the confidence interval in the Bootstrap intermediary effect test. Among them, t is the degree of freedom, s is the number of observations, and $\overline{X}$ is the mean.

2.2. The Theoretical Background of Networked Governance.
The core of network governance is the equal participation of multiple subjects. Government departments, enterprises, associations, and other entities should coordinately develop and jointly assume the responsibilities as the main body of supply. The government's responsibility in network governance is to organize resources, allocate public resources rationally, and maximize public value through the role of the

relationship network of multiple subjects. Enterprises must follow the principles of market-oriented and profit-driven principles and ultimately achieve a win-win result of multiagent cooperation. Social organizations should strengthen their own social role and undertake the main body of sports services. The subjects of network governance can be divided into behavioral interaction and organizational relationships. As the core of network governance, the government is mainly responsible for promoting the realization of sports service goals and building networks from the perspective of organizational relationships. From the perspective of behavioral interaction, networked governance has changed the traditional mode of government work, making the horizontal connection between the government and social organizations and enterprises closer.

Information security mechanisms and effective communication are the two cores that make networked governance work. The information security mechanism requires that the major subjects be guided by common interests, timely understand the goals and trends of other subjects, strengthen information communication, and jointly coordinate resources. The effective communication mechanism is using the embedded network environment, which ensures the benign communication between the subjects and the efficiency of the coordination and interaction process.

The governance tools used in networked governance are no longer traditional norms and compulsory methods, but methods such as calling, mechanism design, etc., integrating economic and administrative methods into the field of sports service governance. The guiding ideology of networked governance of sports service supply in the study area includes "people-oriented," multisubject coordination, and networked governance.

3. Analysis on the Research Results of Sports Service

3.1. Basic Information Descriptive Statistical Results. The proportion of male and female in this survey is shown in Table 3.

Table 3 shows that among the 193 people who participated in the survey this time, 95 are females, accounting for 49.22%, and 98 are males, accounting for 50.78%. The number of males is slightly higher than the number of females, but the ratio of males to females is basically the same. In the number of participants in this survey, gender has no influence on the problems of this research.

The specific distribution of age, education level, occupation, and average monthly income is shown in Figure 4.

In Figure 4, the age distribution of the survey subjects is mainly concentrated in the 18- to 35-year-old population, and the proportion of the number of people in this range is 36.52. The 36- to 45-year-old population accounts for 32.08%. In the education level survey, the proportion of people with a high school or junior college degree is the highest. In the occupational survey, the highest proportion is enterprise personnel, that is, the number of people with an average monthly income in the range of 3000–5000 yuan has

TABLE 3: Gender ratio.

Options	Number (person)	Proportion (%)
Female	95	49.22
Male	98	50.78
Total	193	100.00
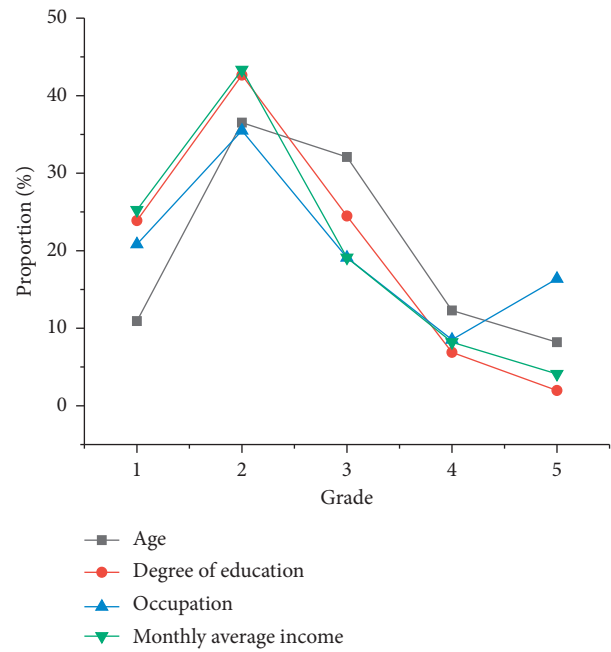
FIGURE 4: Basic information distribution.

the highest proportion. The main ages of residents in the research area are 18–45 years. The education level is mainly high school or junior college, the occupation is enterprise personnel, and the average monthly income is 3000–4000 yuan. Due to the relatively young age distribution, residents in the research area have a higher degree of understanding of sports services.

3.2. Structural Model Analysis. Combining the previous content, it is concluded that the reliability of the scale is 0.85 > 0.7, the reliability of the latent variable combination is 0.8 > 0.7, and the KMO value is 0.9 > 0.8, indicating that the scale data is good. The construct validity is 0.58 > 0.5, the convergence validity is 0.61 > 0.5, and the reliability and validity results are all good. Therefore, the structural model can be used.

A direct relationship model is constructed between the main body of the community environment supply and the supply of sports services, as shown in Figure 5.

Figure 5 shows that, in the direct relationship structure model, five supply entities influence each other, and the five supply entities contain a total of 18 elements. Among them, the main body of the government is that with the widest radiation, which directly affects the main body of enterprises, universities, associations, and residents. The content of Figure 5 has yet to be verified. The content of Figure 5 will be evaluated later, and the nonconforming parts will be eliminated.
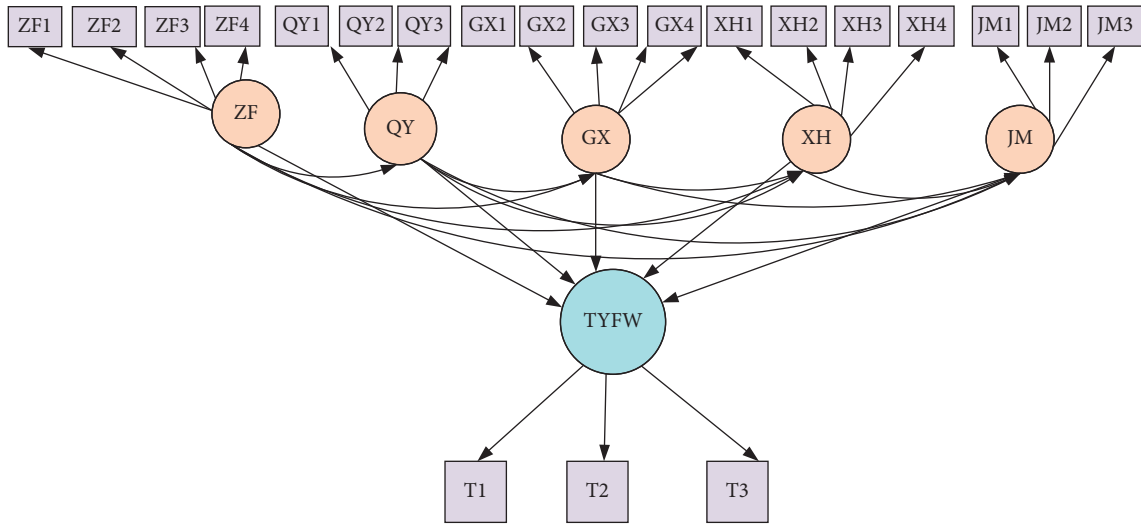
FIGURE 5: Direct relationship model.

The mediating effect model of the community environment is shown in Figure 6.

Figure 6 is used to test the hypothesis put forward in the previous part. The Bootstrap mediation effect test shows that the confidence intervals of the three mediation effects of government, community environment, sports service supply, colleges and universities, community environment, sports service supply, associations, community environment, and sports service attack all contain 0. Therefore, there is no mediating effect, so the assumptions S1b, S3b, and S4b are not valid, and the assumptions S6a, S6c, and S6d are deleted. The mediation effect only considers the relationship between the community environment and the main body of supply and the supply of sports services.

The fit degree of Figures 5 and 6 is judged, and the result is shown in Figure 7.

Figure 7 shows that, in the direct relationship model and the mediation effect model, the 6 fitting indicators are consistent with the standard values, and no abnormal data appear. There is no mismatch in the indicators, and the data do not need to be revised. Therefore, the elements in the model are identified, and hypotheses that do not meet the requirements are deleted.

The standardized path coefficients and significance levels in the structural model are shown in Table 4.

The result of the hypothetical judgment in the mediation effect is as follows: the enterprise, community environment, and sports service supply are 0.29; the confidence interval does not include 0; the mediation effect value of residents, community environment, and sports service supply is 0.60; the confidence interval does not include 0. Hence, S6b and S6e are both established. In Figure 6, the standardized path coefficient of the enterprise to the community environment is 0.3; the path coefficient of the residents to the community environment is 0.06; the significant level is less than 0.001, so, S2b and S5b are established.

Finally, the hypothesis test results are given, as shown in Table 5.

3.3. Analysis of Optimization Results of Networked Governance Model.

The networked governance model is shown in Figure 8.

Figure 8 suggests the following: (1) At present, the task of optimizing the networked governance model in the research area is to transform the leading role of the government and to give full play to the government's overall responsibility. Diversified and autonomous sports service supply is the current trend. In addition to the government, enterprises, universities, associations, and residents enter the field of sports services as important supplementary forces, which can solve the problem of the lack of professional talents in the government departments of the research area. (2) Supporting and cultivating social forces and maximizing the synergy can deal with the problem of insufficient sports services in the research area. The government should strictly access standards, cultivate social supply entities, and continuously optimize the supply structure of sports services in the research area. The division of powers and responsibilities in the market should give full play to the synergy of themes. (3) Supply links should be continuously improved, interaction between subjects should be continuously enhanced, and communication barriers should be broken. For example, the government achieves direct supply through policy guidance to sports service areas. Intermediate links between market entities should be reduced, supply efficiency should be improved, Internet resources should be effectively used, and complete efficient supply. (4) The role of the community environment should be maximized. S6b and S6e show that the community environment plays an intermediary role. This requires reasonable planning and simplification of the supply process in networked governance. (5) The main body should pay more attention to improving the communication mechanism. The degree of informatization should be improved, and the supply risk should be avoided in time. (6) The government plays a supervisory function and establishes an information security mechanism to provide guarantees for information security. The government should regulate the main access mechanism of the information system. (7)
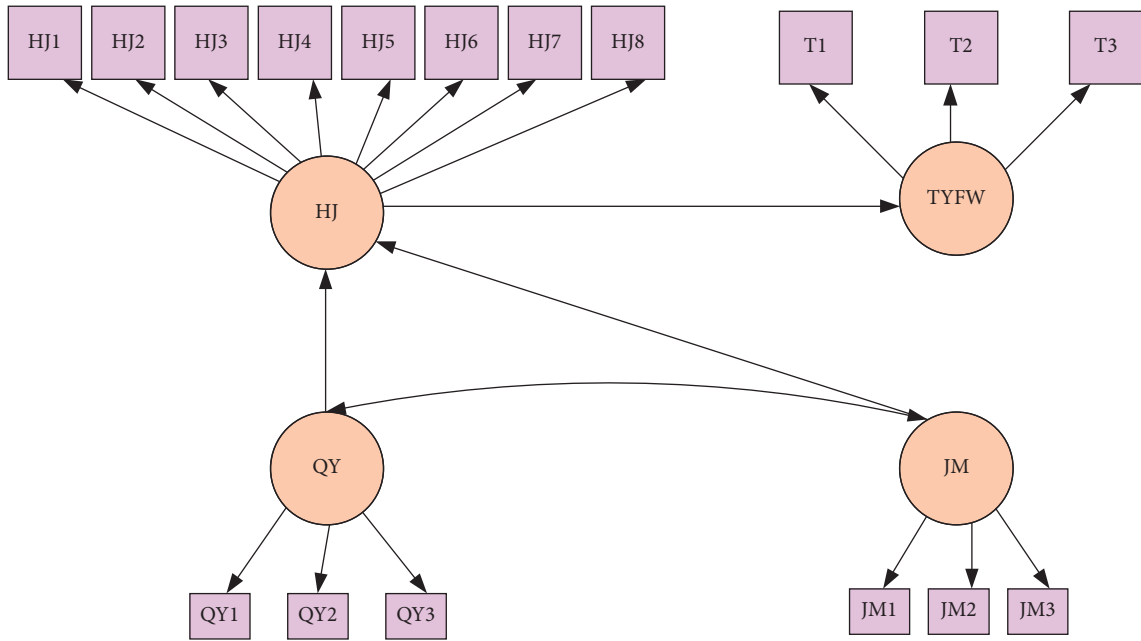
FIGURE 6: The model of mediating effect.
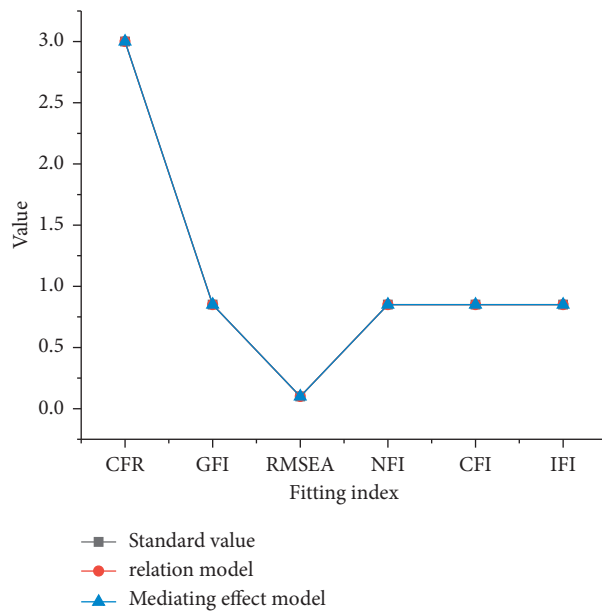
FIGURE 7: The test result of fitting index.

TABLE 4: Hypothetical judgments in the direct relationship.

Supply body	Standardized path coefficient	Significant level	Hypothetical judgment
Government	0.56	<0.01	S1a established
Colleges	0.16	<0.05	S3a established
Association	0.08	<0.05	S4a established
Enterprise	−0.24	<0.05	S2a not established
Resident	−0.14	<0.05	S5a not established

TABLE 5: Hypothesis test results.

Hypothetical number	The specific content of the hypothesis	Result
S1a	Sports services are significantly affected by government entities	Established
S2a	Sports services are significantly affected by the main body of the enterprise	Not established
S3a	Sports services are significantly affected by the main body of colleges and universities	Established
S4a	Sports services are significantly affected by the main body of the association	Established
S5a	Sports services are significantly affected by residents	Not established
S1b	The community environment is significantly affected by the government	Delete
S2b	The community environment is significantly affected by business entities	Established
S3b	The community environment is significantly affected by the main body of the university	Delete
S4b	The community environment is significantly affected by the main body of the association	Delete
S5b	The community environment is significantly affected by the residents	Established
S6	Sports services are significantly affected by the community environment	Established
S6a	The community environment plays an intermediary role between sports services and the supply of government entities	Not established
S6b	The community environment plays an intermediary role between the sports service and the supply of the main body of the enterprise	Established
S6c	The community environment plays an intermediary role between sports services and the supply of the main body of colleges and universities	Not established
S6d	The community environment plays an intermediary role between the sports service and the supply of the main body of the association	Not established
S6e	The community environment plays an intermediary role between sports services and the supply of residents	Established
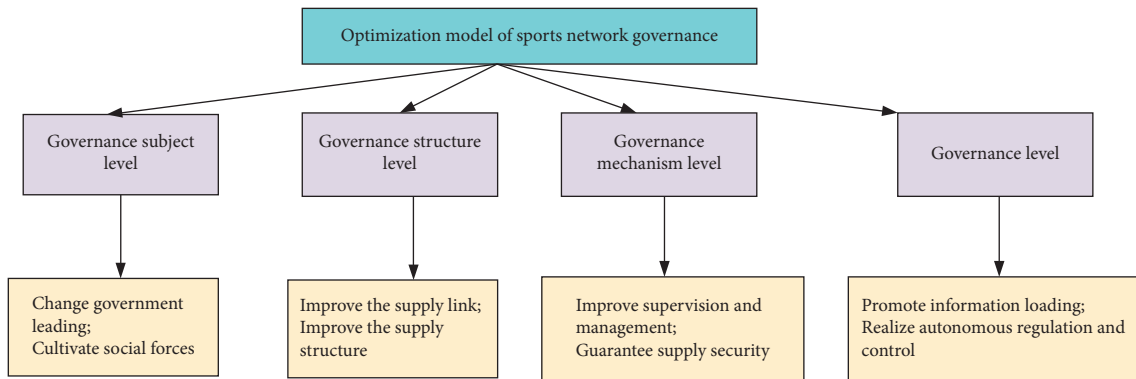
FIGURE 8: Optimization results of networked governance.

Information sharing tools should be used rationally, and information delivery systems should be established. (8) Network management should be promoted. Use networked management tools to connect the entire supply process and guide residents to actively participate in networked management.

4. Conclusions

Through the introduction of the background of networked governance, the supply strategy of sports services is analyzed. Since the supply problem, the networked governance model of the complex system under the sports service has been optimized. The results show that the government, universities, associations, and societies have a direct and positive impact on the supply of sports services. Enterprises and residents have little impact on the supply of sports

services, but they have a positive effect on the community environment. The community environment promotes the supply of sports services and plays an intermediary role. Network governance should focus on the participation of multiple subjects, change the leading role of the government, break down the communication barriers between subjects, and establish an efficient communication mechanism and information sharing system. There are still deficiencies in the research. In determining the subject, due to the sample size, there may be other subjects that have not been taken into consideration. Subsequent research will analyze this part of the content in depth. Scientific governance is provided with a new possibility. The proposed networked governance model provides a greater space for autonomy in public sports services. It advocates the vigorous development of community nongovernmental organizations, stimulates the enthusiasm of community residents to participate, and

ultimately promotes diversified network governance to achieve diversified participation and joint construction. The research provides a certain reference for the networked governance of sports services in the study area.

Data Availability

The data used to support the findings of this study are included within the article.

Conflicts of Interest

The authors declare that they have no conflicts of interest.

Acknowledgments

References

[1] M. Alguacil, J. Núñez-Pomar, F. Calabuig, P. Escamilla-Fajardo, and I. Staskeviciute-Butiene, "Creation of a brand model through SEM to predict users' loyalty and recommendations regarding a public sports service," *Heliyon*, vol. 7, no. 6, Article ID e07163, 2021.

[2] P. Pinheiro and L. Cavique, "Regular sports services: dataset of demographic, frequency and service level agreement," *Data in Brief*, vol. 36, Article ID 107054, 2021.

[3] J. Garcia-Unanue, J. L. Felipe, L. Gallardo, C. Majano, and G. Perez-Lopez, "Decentralisation and efficiency in municipal sports services: expenditure vs. cost," *Sustainability*, vol. 13, no. 4, Article ID 2260, 2021.

[4] D. J. Jalolova, D. A. Xudaybyerdiyeva, and B. A. Abbosov, "The importance of marketing strategies in the provision of physical education and sports services," *South Asian Journal of Marketing & Management Research*, vol. 10, no. 4, pp. 111–119, 2020.

[5] A. Mario, S. G. Javier, and V. Irena, "Be congruent and I will be loyal: the case of sport services," *Sport in Society*, vol. 23, no. 2, pp. 234–248, 2020.

[6] V. Demetris, V. Milena, S. Francesca, and M. Christofi, "Managing technological innovation in the sports industry: a challenge for retail management," *Competitiveness Review: An International Business Journal*, vol. 30, no. 1, pp. 78–100, 2019.

[7] A. Mario, N. P. Juan, P. C. Carlos, and V. Gascó, "Perceived value, satisfaction and future intentions in sport services: putting congruence and brand trust in the equation – linear models vs QCA," *Academia. Revista Latinoamericana de Administración*, vol. 32, no. 4, pp. 566–579, 2019.

[8] K. Kyungyeol, K. B. Kevin, B. Wooyeul, and A. Williams, "Examining structural relationships among sport service environments, excitement, consumer-to-consumer interaction, and consumer citizenship behaviors," *International Journal of Hospitality Management*, vol. 82, pp. 318–325, 2019.

[9] P. F. Katina, J. C. Pyne, C. B. Keating, and D. Komljenovic, "Complex system governance as a framework for asset management," *Sustainability*, vol. 13, no. 15, Article ID 8502, 2021.

[10] A. Mario, "Bottom-Up identification of subsystems in complex governance systems," *Policy Studies Journal*, vol. 48, no. 3, pp. 782–805, 2020.

[11] P. F. Katina and O. F. Keskin, "Complex system governance as a foundation for enhancing the cybersecurity of cyber-physical systems," *International Journal of Cyber Warfare & Terrorism*, vol. 11, no. 3, pp. 1–14, 2021.

[12] B. K. Charles and P. F. Katina, "Complex system governance: concept, utility, and challenges," *Systems Research and Behavioral Science*, vol. 36, no. 5, pp. 687–705, 2019.

[13] T. Yuan, "Towards network governance: educational reforms and governance changes in China (1985–2020)," *Asia Pacific Education Review*, vol. 22, pp. 1–14, 2021.

[14] N. Zhao, Y. Liu, and J. Wang, "Network governance and the evolving urban regeneration policymaking in China: a case study of insurgent practices in enninglu redevelopment project," *Sustainability*, vol. 13, no. 4, p. 2280, 2021.

[15] J. H. Richard, C. Stephen, M. B. Joseph, and C. Keating, "Systems engineering and complex systems governance – lessons for better integration," *INCOSE International Symposium*, vol. 29, no. 1, pp. 421–433, 2019.

[16] W. Dave, "Leadership and foresight in complex system governance," *International Journal of System of Systems Engineering*, vol. 8, no. 3, pp. 249–267, 2018.

[17] N. H. Sweilam, D. Kumar, C. M. A. Pinto, and D. Baleanu, "Editorial note on the special issue: "fractional calculus models for the dynamics of complex systems," *Journal of Advanced Research*, vol. 32, pp. A1–A3, 2021.

[18] M. Grassia, M. De Domenico, and G. Mangioni, "Machine learning dismantling and early-warning signals of disintegration in complex systems," *Nature Communications*, vol. 12, no. 1, p. 5190, 2021.

[19] T. Go, B. F. Henrique, S. S. Roberto, and L. Basso, "Professional learning in physical education in Brazil: issues and challenges of a complex system," *Sport, Education and Society*, vol. 26, no. 7, pp. 773–787, 2021.

[20] N. Kapucu and Q. Hu, "The development of network governance and its relevance for public affairs education," *Journal of Public Affairs Education*, vol. 27, no. 3, pp. 267–275, 2021.

[21] A. H. Kabir, "Network governance' and the formation of the strategic plan in the higher education sector in Bangladesh," *Journal of Education Policy*, vol. 36, no. 4, pp. 1–25, 2021.

[22] M. Etemadi, P. Kenis, K. Ashtarian, H. Abolghasem Gorji, and H. Mohammadi Kangarani, "Network governance theory as basic pattern for promoting financial support system of the poor in Iranian health system," *BMC Health Services Research*, vol. 21, no. 1, p. 556, 2021.

[23] A. Matei, A.-S. Dumitru, and C.-G. Antonovici, "The EU health technology assessment and the open method of coordination: a relation with Potential in the context of network governance," *Sustainability*, vol. 13, no. 6, Article ID 3582, 2021.

[24] G. Giorgos and K. Ashok, "A dynamic model of global value network governance," *Environment and Planning*, vol. 53, no. 1, pp. 53–72, 2021.

[25] N. Kapucu and S. Beaudet, "Network governance for collective action in implementing united nations sustainable development goals," *Administrative Sciences*, vol. 10, no. 4, p. 100, 2020.

[26] O. Steven, V. Niels, M. Hugo, and B. Brugghemans, "Network of networks: preliminary lessons from the antwerp port authority on crisis management and network governance to deal with the COVID -19 pandemic," *Public Administration Review*, vol. 80, no. 5, pp. 880–894, 2020.

[27] O. L. Larsson, "The governmentality of network governance: collaboration as a new facet of the liberal art of governing," *Constellations*, vol. 27, no. 1, pp. 111–126, 2020.

[28] D. Macdonald, R. Johnson, and B. Lingard, "Globalisation, neoliberalisation, and network governance: an international study of outsourcing in health and physical education," *Discourse: Studies in the Cultural Politics of Education*, vol. 41, no. 2, pp. 169–186, 2020.

[29] P. Oren, C. Reuven, and S. Nir, "Governance through global networks and corporate signalling," *Regulation & Governance*, vol. 13, no. 4, pp. 447–469, 2019.

[30] T. Cragg, T. McNamara, I. Descubes, and F. Guerin, "Manufacturing SMEs, network governance and global supply chains," *Journal of Small Business and Enterprise Development*, vol. 27, no. 1, pp. 130–147, 2019.

Research Article

Performance Evaluation of MU-MIMO Transmissions with Joint Interference Constraint in HetNet

Wenjian Zhang [iD] **and Senlin Jiang** [iD]

Wuxi Institute of Technology, Wuxi, China

Correspondence should be addressed to Wenjian Zhang; zhangwj@wxit.edu.cn

In this paper, we investigate the per-tier outage probability of multiuser multiple-input multiple-output (MU-MIMO) transmissions in heterogeneous networks (HetNets) with joint interference constraint. In the tier of cellular cell, user equipment (UE) is required to report measured channel information and the base station (BS) adopts ZF-based precoding MU-MIMO transmission to achieve multiuser diversity gain. With the constraint of cross-tier interference and unpredicted inter-beam interference, we derive the closed-form expression of outage probability of downlink MU-MIMO transmissions. Considering the capacity of nodes in the tier of ad hoc networks, a max-SINR scheduler and codebook-based MU-MIMO transmission are employed. The scheduler selects the best receiving nodes for each beam in predefined codebook according to measured signal to interference plus noise ratio (SINR), and the transmitting node performs data transmissions using orthogonal beams. In the presence of inter-node interference, inter-beam interference, and cross-tier interference, we obtain the closed-form expression of outage probability of MU-MIMO transmissions when downlink or uplink transmissions occur in cellular cell. Additionally, in case that the outage probability in ad hoc networks should satisfy quality of service (QoS) requirement, a restricted area in cellular cell in which the outage probability in ad hoc networks is not greater than a required threshold is explored. Numerical results show that the unpredictable inter-beam interference in cellular cell degrades the outage probability slightly. The restricted area increases with the outage probability threshold.

1. Introduction

Wireless ad hoc network is an autonomous network consisting of a collection of peer nodes equipped with wireless transceiver. The nodes communicate with each other directly or by multihop link with the help of intermediate nodes. Due to the flexible structure, ad hoc networks have attracted a lot of attention in different application areas, such as military battlefield [1], emergency mission, postdisaster reconstruction [2], and vehicular communication [3]. In this paper, the temporary ad hoc networks without infrastructure and the widely deployed cellular cells constitute HetNets [4], as shown in Figure 1.

Due to the scarcity of frequency resource and lack of coordination, the HetNets usually share the same channels. The occurrence of cross-tier interference with each other is inevitable. In order to lower the impact on the performance of the coexisting system, some interference coordination schemes, such as spectrum allocation, power control, and interference cancellation, have been studied in prior works [5–7]. Since there are several transmitting nodes in the ad hoc networks that send data on the same channels simultaneously, a receiving node experiences the inter-node interference signal from other transmitting nodes additionally. The effect of inter-node interference signal was investigated in [8].

With the goal of improving the performance of HetNets, MU-MIMO technology has been employed. Due to its extremely high spectral efficiency, MU-MIMO has received a significant attention [9–11]. In the 3rd Generation Partnership Project (3GPP) Long-Term Evolution-Advanced (LTE-A) [12] and IEEE 802.11ac [13], the MU-MIMO has
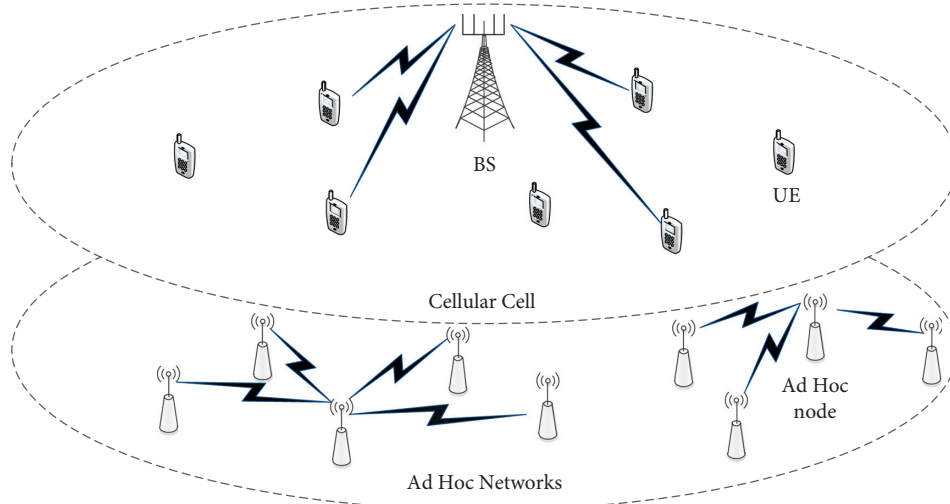
Figure 1: HetNet consisting of cellular cell and ad hoc network with MU-MIMO transmissions.

been adopted. In MU-MIMO transmissions, according to the measured information feedback from receivers, the forward transmission could be achieved in different ways. In the first way, the receivers perform channel information measurement and feed back the measured information to the transmitter. The scheduler selects the matching receivers and assigns orthogonal beams. Then, the transmitter sends data to the selected receivers using the assigned beams. The precoding matrixes of beamforms are calculated according to the feedback channel information by some algorithms, such as SVD [14], block diagonalization [15], zero-forcing (ZF) precoding, and dirty-paper coding [16]. In the second way, the precoding matrixes are predefined in codebook. The receivers perform the SINR measurement for each predefined beam and report the measured SINRs to the transmitter. The max-SINR scheduler selects the best receivers for each beam according to the reported SINRs [17]. Then, the transmitter simultaneously transmits data to the selected receivers, using orthogonal random beams.

The first way is applicable to the situation that the transmitter could get the full channel information. In case of perfect channel state information (CSI), the beams for each receiver keep orthogonal in data transmission phase. If perfect CSI could not be obtained due to some reasons, such as quantization error, the beams interfere with each other. In the second way, since the max-SINR scheduler does not need perfect CSI, the beam for a selected receiver may mismatch with its forward channel in data transmission phase. Hence, the beams for each receiver interfere with each other. The inter-beam interference impairs the performance of MU-MIMO transmissions inevitably.

Moreover, the cross-tier interference signal that a receiving node suffers may come from the cellular BS in a downlink interval. Because the transmitting power of BS is much greater than that of a transmitting node, the receiving nodes close to the BS may experience a high outage probability which could not satisfy the QoS requirements. This means that there is a performance restricted area around the BS in which the outage probability of a receiving node

exceeds a required threshold. The area of the restricted area is worth exploring.

Motivated by the discussion above, in the paper, we evaluate per-tier outage probability performance of MU-MIMO transmissions with joint interference constraint in HetNets. Our main contributions are given as follows:

(i) We adopt different MU-MIMO transmission models in cellular cell and ad hoc networks according to the capacity of equipment and the complexity of network structure. The models have different complexities and transmission performances.

(ii) We derive per-tier closed-form outage probability of MU-MIMO transmissions with the joint interference constraint.

(iii) We explore the restricted area in cellular cell in which the outage probability of the MU-MIMO transmissions in ad hoc networks could not satisfy QoS requirements.

The remainder of the paper is structured as follows. Section 2 gives network model and transmission model. Section 3 derives per-tier outage probability of MU-MIMO transmissions in the presence of joint interference. Section 4 explores the restricted area in cellular cell. Section 5 describes the numerical results. Finally, Section 6 gives the conclusions.

2. System Model

We assume a HetNet consisting of a time division multiplexing access (TDMA) cellular system and coexisting ad hoc networks in this paper.

2.1. Network Model. In cellular cell, the cellular BS B_0 at the center serves a circle area. The UEs are distributed in the coverage of B_0 according to a spatial Poisson point process (SPPP) with intensity λ_c. Hence, the UEs are denoted as

$\Psi(\lambda_c) = \{Z_\psi\}$, where Z_ψ is the position of UE $\psi \in Z_\psi$. The model has been used, and the validity has been confirmed in prior works [18–20].

In coexisting ad hoc networks, we assume that the ALOHA slotted protocol is adopted [21]. In each slot, a subset of nodes transmits data on the same channel simultaneously. The transmitting nodes are assumed to be distributed according to a SPPP with intensity λ_f. Similarly, the transmitting nodes are denoted as $\Phi(\lambda_f) = \{Z_\varphi\}$.

2.2. Transmission Model. The BS B_0 and the transmitting nodes in ad hoc networks are assumed to be equipped with N_c and N_f transmitting antennas, respectively, and the receivers are assumed to be equipped with single receiving antenna.

In cellular cell, the CSI feedback is widely employed, as in the LTE system. It is easy for the BS to obtain the feedback CSI from UE, and thus the linear ZF-based precoding transmission is assumed to be applied in downlink interval due to its low complexity. With ZF-based precoding transmission, the BS B_0 chooses its precoding matrix $\mathbf{W} \in \mathbb{C}^{N_c \times K_c} = [\mathbf{w}_i]_{1 \leq i \leq K_c}$ as the normalized columns of the pseudo-inverse $\mathbf{H}^*(\mathbf{HH}^*)^{-1} \in \mathbb{C}^{N_c \times K_c}$, where $\mathbf{H}^*$ represents the conjugate transpose of $\mathbf{H}$ and K_c $(1 \leq K_c \leq N_c)$ is number of selected UEs. In the data transmission phase, the BS transmits data to the selected UE using the beams $\mathbf{w}_i$ $(i = 1, 2, \ldots, K_c)$. The total power of BS is assumed to be P_c. In uplink interval of cellular cell, all scheduled UEs send data packet to the BS simultaneously with the same power P_m.

Considering that the processing capacity of ad hoc node is weaker than that of cellular BS, the real-time calculation of precoding matrixes could not be achieved. Hence, the codebook-based MU-MIMO transmission with finite-rate feedback is adopted in ad hoc networks. In each slot, the max-SINR scheduler of transmitting node selects K_f $(1 \leq K_f \leq N_f)$ receiving nodes for each beam based on measured SINRs. In the data transmission phase, the transmitting node transmits data to the selected receiving nodes simultaneously, using random orthogonal beams $\mathbf{v}_k$ $(k = 1, 2, \ldots, K_f)$ [17]. The total power of a transmitting node is assumed to be P_f.

3. Per-Tier Outage Probability Evaluation

In this section, we evaluate per-tier outage probability of MU-MIMO transmissions with joint interference constraint and give the closed-form expressions of outage probability.

3.1. Outage Probability of Downlink MU-MIMO Transmissions in Cellular Cell. We assume that UE i is located at the origin. In downlink interval, the UE i suffers the unpredicted inter-beam interference signal and cross-tier interference signal. Hence, the instantaneous received signal for the UE i is denoted as

$$y_i = \underbrace{\sqrt{\frac{P_c}{K_c}D_i^{-\alpha}}\mathbf{h}_i^H\mathbf{w}_i\mathbf{s}_i}_{\text{desired signal}} + \underbrace{\phi\sum_{j\in K_c, j\neq i}\sqrt{\frac{P_c}{K_c}D_i^{-\alpha}}\mathbf{h}_i^H\mathbf{w}_j\mathbf{s}_j}_{\text{inter-beam interference signal}} + \underbrace{\sum_{f\in\Phi}\sqrt{P_f\left|Z_f\right|^{-\alpha}}g_{f,i}s_f}_{\text{cross-tier interference signal}} + n_i, \tag{1}$$

where $\mathbf{h}_i \in \mathbb{C}^{N_c \times 1}$ is the channel gain vector between UE i and the BS B_0, whose entries follow complex Gaussian distribution $h_{i,j} \sim CN(0,1)$. Similarly, $g_{f,i}$ is the channel gain between UE i and a transmitting node in ad hoc networks. $\mathbf{s}_i$ is the symbol vector for UE i. n_i represents the additive white Gaussian noise (AWGN) with zero mean and variance of σ^2. ϕ is a switching variable. In case of perfect CSI or $K_c = 1$, $\phi = 0$. Otherwise, $\phi = 1$.

It is obvious that the system is an interference-limited system. Hence, the effect of thermal noise could be ignored for analysis simplicity. The instantaneous received SINR is denoted as

$$\gamma_i = \frac{P_c D_i^{-\alpha}/K_c\left|\mathbf{h}_i^H\mathbf{w}_i\right|^2}{\phi\left(P_c D_i^{-\alpha}/K_c\right)\sum_{j\in K_c, j\neq i}\left|\mathbf{h}_i^H\mathbf{w}_j\right|^2 + P_f\sum_{f\in\Phi}\left|Z_f\right|^{-\alpha}\left|g_{f,i}\right|^2}$$

$$= \frac{\vartheta S}{\phi\vartheta I_{\text{IBI}} + I_{\text{CTI}}}, \tag{2}$$

where $\vartheta = P_c D_i^{-\alpha}/K_c$. The random variables $S = |\mathbf{h}_i^H\mathbf{w}_i|^2$ and $I_{\text{IBI}} = \sum_{j\in K_c, j\neq i}|\mathbf{h}_i^H\mathbf{w}_j|^2$ are chi-square random variables with $2(N_c - K_c + 1)$ and $2(K_c - 1)$ degrees of freedom, respectively. The random variable $I_{\text{CTI}} = P_f\sum_{f\in\Phi}|Z_f|^{-\alpha}|g_{f,k}|^2$ represents the power of cross-tier interference signal.

The outage probability of an MU-MIMO transmission is defined as the probability that instantaneous received SINR does not exceed the required SINR threshold. Assuming that the SINR threshold of cellular cell is $\gamma_{c,\text{thre}}$, the outage probability of downlink MU-MIMO transmissions is denoted as

$$\begin{aligned} p_i(D_i) &= \mathbb{P}\left(\gamma_i \leq \gamma_{c,\text{thre}}\right) \\ &= \mathbb{P}\left(S \leq \omega\left(\phi\vartheta I_{\text{IBI}} + I_{\text{CTI}}\right)\right) \\ &= \int_0^\infty \mathbb{P}\left(S \leq \omega x\right) f_{\phi\vartheta I_{\text{IBI}} + I_{\text{CTI}}}(x)\mathrm{d}x, \end{aligned} \tag{3}$$

where $\omega = \gamma_{c,\text{thre}}/\vartheta$.

Note that the random variable S obeys chi-square distribution with $2(N_c - K_c + 1)$ degrees of freedom. Hence, the term $\mathbb{P}(S \leq \omega x)$ is denoted as

$$\mathbb{P}(S \leq \omega x) = \int_0^{\omega x} \frac{t^{N_c - K_c}}{2^{N_c - K_c + 1}(N_c - K_c)!} e^{-(t/2)} dt$$

$$= 1 - \frac{1}{(N_c - K_c)!} \Gamma(N_c - K_c + 1, \omega x) \quad (4)$$

$$= 1 - e^{-\omega x} \sum_{m=0}^{N_c - K_c} \frac{(\omega x)^m}{m!},$$

$$p_i(D_i) = \left\{ 1 - \sum_{m=0}^{N_c - K_c} \frac{(-\omega)^m}{m!} \frac{d^m}{d\omega^m} \mathscr{L}_{I_{\text{CTI}}}(\omega), \phi = 0, 1 - \sum_{m=0}^{N_c - K_c} \frac{(-\omega)^m}{m!} \frac{d^m}{d\omega^m} \mathscr{L}_{I_{\text{IBI}}}(\vartheta\omega) \mathscr{L}_{I_{\text{CTI}}}(\omega), \phi = 1, \right. \quad (5)$$

where $\mathscr{L}_V(\cdot)$ denotes the Laplace transform of the random variable V. The transform of $\mathscr{L}[t^m f(t)] = (-1)^m F^{(m)}(s)$ is employed.

Since I_{IBI} is the chi-square random variable with $2(K_c - 1)$ degrees of freedom, the Laplace transform of I_{IBI} and its m-th order differential are, respectively, defined as

$$\mathscr{L}_{I_{\text{IBI}}}(\vartheta\omega) = \frac{1}{(1 + \gamma_{c,\text{thre}})^{K_c - 1}}$$

$$\frac{d^m}{d\omega^m} \mathscr{L}_{I_{\text{IBI}}}(\vartheta\omega) = \frac{(-\vartheta)^m}{(1 + \vartheta\omega)^{K_c + m - 1}} \prod_{j=0}^{m-1}(K_c + j - 1). \quad (6)$$

In addition, the transmitting nodes in a slot are distributed according to a SPPP with intensity λ_f, and hence the cross-tier interference signal is modeled as a general Poisson shot noise process [22]. The Laplace transform of I_{CTI} could be obtained as

$$\mathscr{L}_{I_{\text{CTI}}}(\omega) = \exp\left\{ -\lambda_f \int_{\mathbb{R}^2} 1 - \mathbb{E}_H[\exp(-\omega H |x|^{-\alpha})] \right\}$$

$$= \exp\left\{ -2\pi\lambda_f \int_0^\infty \frac{x}{1 + |x|^\alpha/\omega} dx \right\} \quad (7)$$

$$= \exp(-\lambda_f Q \omega^\delta),$$

where $\Gamma(a, t) = \int_0^t x^{a-1} e^{-x} dx$ is complementary incomplete gamma function with $a > 0$. Since the variables I_{IBI} and I_{CTI} are independent random variables, substituting the result in equation (4) into (3), the outage probability of downlink MU-MIMO transmissions is rewritten as

where $\delta = 2/\alpha$ and $Q = \pi P_f^\delta \Gamma(\delta)\Gamma(1 - \delta)$.

If a high probability of successful reception in cellular cell is required, it is reasonable that the density of transmitting nodes λ_f is very small. Hence, the m-th order differential of $\mathscr{L}_{I_{\text{CTI}}}(\omega)$ can be evaluated using first-order Taylor series around $\lambda_f Q \omega^\delta = 0$. For all $m \geq 1$, the m-th order differential of $\mathscr{L}_{I_{\text{CTI}}}(\omega)$ is given approximately as

$$\frac{d^m}{d\omega^m} \mathscr{L}_{I_{\text{CTI}}}(\omega)$$

$$\approx -\left(\lambda_f Q \omega^{\delta - m} \prod_{l=0}^{m-1}(\delta - m) \right) e^{-\lambda_f Q \omega^\delta} + \Psi(\lambda_f^2 Q^2 \omega^{2\delta}). \quad (8)$$

In case of $\phi = 0$, the outage probability of downlink MU-MIMO transmissions is denoted as

$$p_i(D_i) = \left\{ \begin{array}{ll} 1 - \exp(-\lambda_f Q \omega^\delta), & K_c = N_c, \\[2em] \lambda_f Q \omega^\delta \left(1 + \sum_{m=1}^{N_c - K_c} \frac{1}{m!} \prod_{l=0}^{m-1}(1 - \delta) \right), & 1 \leq K_c < N_c. \end{array} \right. \quad (9)$$

In case of $\phi = 1$ and $K_c = N_c$, the outage probability is denoted as

$$p_i(D_i) = 1 - \frac{e^{-\lambda_f Q \omega^\delta}}{(1 + \gamma_{c,\text{thre}})^{K_c - 1}}. \quad (10)$$

If $1 < K_c < N_c$, the outage probability is denoted as

$$
\begin{aligned}
p_i(D_i) &= 1 - \sum_{m=0}^{N_c - K_c} \frac{(-\omega)^m}{m!} \sum_{l=0}^{m} \binom{m}{l} \frac{d^l}{d\omega^l} \mathscr{L}_{I_{\mathrm{IBI}}}(\omega) \frac{d^{m-l}}{d\omega^{m-l}} \mathscr{L}_{I_{\mathrm{CTI}}}(\omega) \\
&= \mathscr{F}_{\frac{\gamma_{c,\mathrm{thre}}}{1 + \gamma_{c,\mathrm{thre}}}} (N_c - K_c + 1, K_c - 1) \\
&\quad + \lambda_f Q \omega^\delta \left(\mathscr{K}(K_c - 1) - \mathscr{F}_{\frac{\gamma_{c,\mathrm{thre}}}{1 + \gamma_{c,\mathrm{thre}}}} (N_c - K_c + 1, K_c - 1) \right).
\end{aligned}
\tag{11}
$$

For the definitions of the function $\mathscr{F}_x(a, b)$ and the variable $\mathscr{K}(a)$, refer to the work [9].

3.2. Outage Probability of MU-MIMO Transmissions in Ad Hoc Network.

Firstly, it is noted that some intermediate variables in the previous section are reused in this section for expression simplicity.

In ad hoc networks, a receiving node suffers inter-node interference signal additionally. Hence, for a receiving node k located at the origin, the received signal for the assigned beam $\mathbf{v}_k$ is denoted as

$$
y_k = \underbrace{\sqrt{\frac{P_f}{K_f} D_k^{-\alpha}} \mathbf{h}_k^H \mathbf{v}_k s_k}_{\text{desired signal}} + \underbrace{\sum_{j \in K_f, j \neq k} \sqrt{\frac{P_f}{K_f} D_k^{-\alpha}} \mathbf{h}_j^H \mathbf{v}_j s_j}_{\text{inter-beam interference signal}} + S_{(D,U)} \left\{ \underbrace{\sqrt{P_c D_{c,k}^{-\alpha}} g_{c,k} s_c, \sum_{\psi \in \Psi} \sqrt{P_m |X_\psi|^{-\alpha}} g_{\psi,k} s_\psi}_{\text{cross-tier interference signal}} \right\} + \underbrace{\sum_{\varphi \in \Phi/T_k} \sqrt{P_f |Z_\varphi|^{-\alpha}} g_{\varphi,k} s_\varphi}_{\text{inter-node interference signal}} + n_k,
\tag{12}
$$

where $\mathbf{h}_k \in \mathbb{C}^{N_f \times 1}$ is the channel gain vector between the receiving node k and the transmitting node. $g_{\varphi,k}$ is the channel gain between receiving node k and a transmitter φ, which follows Rayleigh distribution. $S_{(D,U)}\{S_1, S_2\}$ represents $S = S_1$ in case of D or $S = S_2$ in case of U. Hence, the cross-tier interference signal from cellular cell is $\sqrt{P_c D_{c,k}^{-\alpha}} g_{c,k} s_c$ in case of downlink interval or $\sum_{\psi \in \Psi} \sqrt{P_m |X_\psi|^{-\alpha}} g_{\psi,k} s_\psi$ in case of uplink interval.

Note that the cross-tier interference signal in the data transmission phase may change to be different from that of SINR measurement. If the power of instantaneous cross-tier interference signal increases, the receiving node that has the best SINR for the assigned beam may be changed. However, the receiving node could not be adjusted during data transmission. The performance of MU-MIMO transmissions may degrade.

For the receiving node k, the instantaneous received SINR for the assigned beam $\mathbf{v}_k$ is denoted as

$$
\begin{aligned}
\gamma_k &= \frac{(P_f/K_f) D_k^{-\alpha} |\mathbf{h}_k^H \mathbf{v}_k|^2}{\phi(P_f D_k^{-\alpha}/K_f) \sum_{j \in K_f, j \neq k} |\mathbf{h}_j^H \mathbf{v}_j|^2 + P_f \sum_{\varphi \in \Phi/T_k} |Z_\varphi|^{-\alpha} |g_{\varphi,k}|^2 + I_{\mathrm{CTI}}} \\
&= \frac{\vartheta S}{\phi \vartheta I_{\mathrm{IBI}} + I_{\mathrm{INI}} + I_{\mathrm{CTI}}},
\end{aligned}
\tag{13}
$$

where $\vartheta = P_f D_k^{-\alpha}/K_f$. The definition of random variables S and I_{IBI} is similar to that in equation (2). In terms of the properties of the SPPP model, the random variable I_{INI} has same property as the variable I_{CTI} in equation (2). The random variable I_{CTI} is dependent on the type of interval in cellular cell. In case of downlink interval,

$I_{\text{CTI}} = P_c |D_{c,k}|^{-\alpha} |g_{c,k}|^2$. In case of uplink interval, $I_{\text{CTI}} = \sum_{\psi \in \Psi} P_m |X_\psi|^{-\alpha} |g_{\psi,k}|^2$. ϕ is a switching variable. In case $K_f = 1$, $\phi = 0$. Otherwise, $\phi = 1$.

Similarly, we assume that the SINR threshold in ad hoc networks is $\gamma_{f,\text{thre}}$. Referring to equation (3), the outage probability is denoted as

$$p_k(D_k) = \mathbb{P}\left(S \leq \omega\left(\phi \vartheta I_{\text{IBI}} + I_{\text{INI}} + I_{\text{CTI}}\right)\right), \tag{14}$$

where $\omega = \gamma_{f,\text{thre}}/\vartheta$.

Considering that the random variable S obeys exponential distribution and I_{IBI}, I_{INI}, and I_{CTI} are independent random variables, the outage probability is expressed as

$$p_k(D_k) = \begin{cases} 1 - \mathscr{L}_{I_{\text{INI}}}(\omega)\mathscr{L}_{I_{\text{CTI}}}(\omega), & \phi = 0, \\ 1 - \mathscr{L}_{I_{\text{IBI}}}(\vartheta\omega)\mathscr{L}_{I_{\text{INI}}}(\omega)\mathscr{L}_{I_{\text{CTI}}}(\omega), & \phi = 1. \end{cases} \tag{15}$$

Since I_{IBI} is the chi-square random variable with $2(K_f - 1)$ degrees of freedom, the Laplace transform of I_{IBI} is defined as

$$\mathscr{L}_{I_{\text{IBI}}}(\vartheta\omega) = \frac{1}{(1 + \vartheta\omega)^{K_f - 1}}. \tag{16}$$

The inter-node interference signal could be modeled as a general Poisson shot noise process. Hence, the Laplace transform of I_{INI} is the same as the result in equation (7), i.e.,

$$\mathscr{L}_{I_{\text{INI}}}(\omega) = \exp\left(-\pi\lambda_f B(\delta, 1 - \delta)\left(\omega P_f\right)^\delta\right), \tag{17}$$

where $B(a, b) = \Gamma(a)\Gamma(b)/\Gamma(a + b)$ denotes the beta function with gamma function $\Gamma(a) = \int_0^\infty x^{a-1} e^{-x} dx$.

If the cross-tier interference signal comes from UEs in uplink interval, since the UEs are distributed according to a SPPP with intensity λ_c, similarly the term of $\mathscr{L}_{I_{\text{CTI}}}(\omega)$ is given as

$$\mathscr{L}_{I_{\text{CTI}}}(\omega) = \exp\left(-\pi\lambda_c B(\delta, 1 - \delta)\left(\omega P_m\right)^\delta\right). \tag{18}$$

Substituting the results in equations (16)~(18) into equation (15), the outage probability of MU-MIMO transmissions is denoted as

$$p_k(D_k) = \begin{cases} 1 - e^{-\pi\omega^\delta\left(\lambda_f P_f^\delta + \lambda_c P_m^\delta\right)B(\delta, 1-\delta)}, & \phi = 0, \\ 1 - \dfrac{e^{-\pi\omega^\delta\left(\lambda_f P_f^\delta + \lambda_c P_m^\delta\right)B(\delta, 1-\delta)}}{\left(1 + \gamma_{f,\text{thre}}\right)^{K_f - 1}}, & \phi = 1. \end{cases} \tag{19}$$

If the cross-tier interference signal comes from cellular BS in downlink interval, taking the Rayleigh fading channel into account, the term of $\mathscr{L}_{I_{\text{CTI}}}(\omega)$ is given as

$$\mathscr{L}_{I_{\text{CTI}}}(\omega) = \frac{1}{1 + \omega P_c D_{c,k}^{-\alpha}}. \tag{20}$$

By using the results in equations (16)~(17) and (20), the outage probability is denoted as

$$p_k(D_k) = \begin{cases} 1 - \dfrac{e^{-\pi\lambda_f\left(\omega P_f\right)^\delta B(\delta, 1-\delta)}}{\left(1 + \omega P_c D_{c,k}^{-\alpha}\right)}, & \phi = 0, \\[4mm] 1 - \dfrac{e^{-\pi\lambda_f\left(\omega P_f\right)^\delta B(\delta, 1-\delta)}}{\left(1 + \omega P_c D_{c,k}^{-\alpha}\right)\left(1 + \gamma_{f,\text{thre}}\right)^{K_f - 1}}, & \phi = 1. \end{cases} \tag{21}$$

4. Restricted Area in Cellular Cell

For a receiving node in MU-MIMO transmission in ad hoc networks, it suffers the cross-tier interference signal from cellular cell. Considering that the transmitting power of cellular BS is greater than that of a transmitting node, the cross-tier interference signal may severely impair the performance of MU-MIMO transmissions in ad hoc networks during the downlink interval.

For the receiving nodes close to the cellular BS, their outage probability performance may not satisfy the QoS requirements. Hence, the instantaneous outage probability is not greater than a required threshold, i.e.,

$$p_k(D_k) = 1 - \frac{P_c D_{c,k}^{-\alpha} e^{-\pi\omega^\delta\left(\lambda_f P_f^\delta\right)B(\delta, 1-\delta)}}{(1 + \omega)(1 + \vartheta\omega)^{K_f - 1}} \leq \varepsilon, \tag{22}$$

where ε is the outage probability threshold. Consequently, the distance between BS B_0 and the receiving node k should satisfy

$$D_{c,k} \geq \left(\frac{P_c e^{-\pi\omega^\delta\left(\lambda_f P_f^\delta\right)B(\delta, 1-\delta)}}{(1 - \varepsilon)(1 + \omega)\left(1 + \gamma_{f,\text{thre}}\right)^{K_f - 1}}\right)^{1/\alpha}$$
$$> \left(\frac{P_c\left(1 - \pi\omega^\delta\left(\lambda_f P_f^\delta\right)B(\delta, 1-\delta)\right)}{(1 - \varepsilon)(1 + \omega)\left(1 + \gamma_{f,\text{thre}}\right)^{K_f - 1}}\right)^{1/\alpha}. \tag{23}$$

Considering $\omega = K_f \gamma_{f,\text{thre}}/(P_f D_k^{-\alpha})$, the distance $D_{c,k}$ is the subtractive function of the distance D_k. Intuitively, the decrease of the distance D_k improves the power of desired signal at a receiving node, and thus more receiving nodes could tolerate the cross-tier interference to satisfy QoS requirements.

Furthermore, we assume that the minimum distance between a transmitting node and its receiving node is R, and hence the minimum value of $D_{c,k}$ is denoted as

$$D_{c,k}^{\min} = \left(\frac{P_c P_f\left(1 - \pi\lambda_f R^2\left(K_f \gamma_{f,\text{thre}}\right)^\delta B(\delta, 1-\delta)\right)}{(1 - \varepsilon)\left(P_f + K_f R^\alpha \gamma_{f,\text{thre}}\right)\left(1 + \gamma_{f,\text{thre}}\right)^{K_f - 1}}\right)^{1/\alpha}. \tag{24}$$

TABLE 1: Simulation configurations.

| Parameter	Value
Total transmitting power $P_c/P_f/P_m$	46/23/13 dBm
Transmitting antennas N_c and N_f	8
Receiving UE K_c	4,8
Receiving nodes K_f	4,8
Path loss exponent α	4
SINR threshold $\gamma_{c,\ thre}$	−30 dB
SINR threshold $\gamma_{f,\ thre}$	−20, −30 dBm
Distance between BS and UE D_i	500 m
Distance between transmitting node and receiving node D_k	100 m
MU-MIMO scheme in cellular cell	ZF-based
MU-MIMO scheme in ad hoc networks	Codebook-based
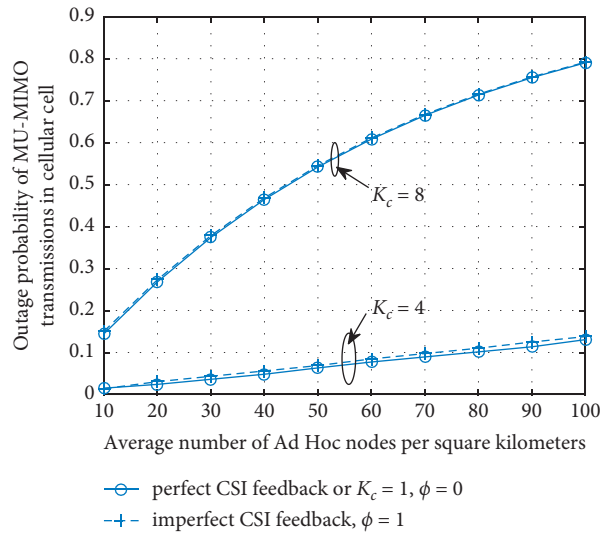
FIGURE 2: Outage probability of MU-MIMO transmissions in cellular cell vs. average number of ad hoc nodes.
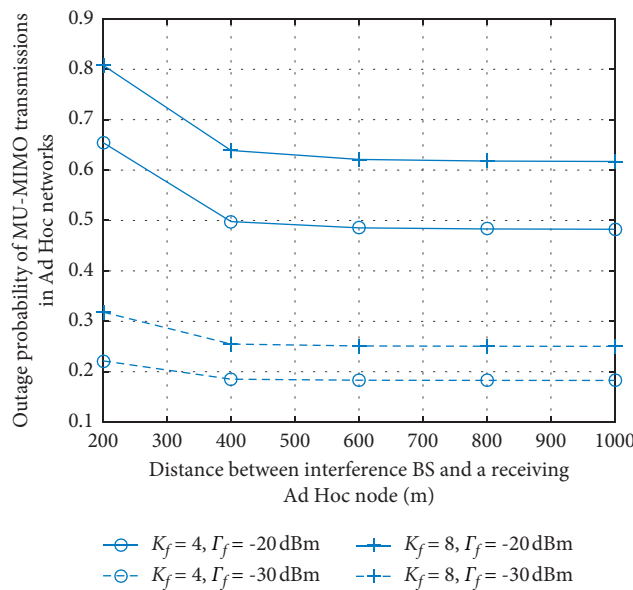

FIGURE 3: Outage probability in ad hoc networks (downlink interval) vs. distance between cellular BS and a receiving node.
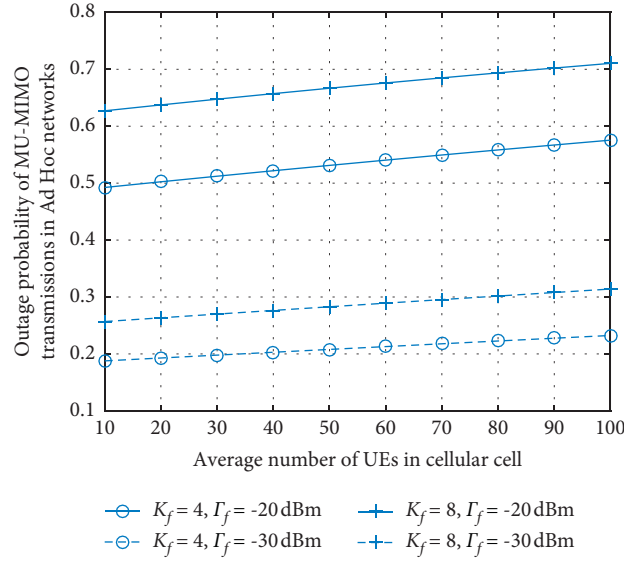
FIGURE 4: Outage probability in ad hoc networks (uplink interval) vs. average number of UE.
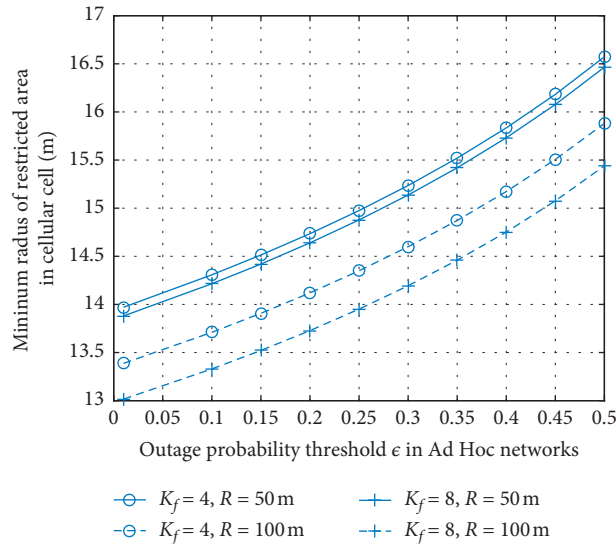

FIGURE 5: Minimum radius of restricted area in cellular cell vs. outage probability threshold in ad hoc networks.

It is obvious that there is a circle area with the BS as center and $D_{f,c}^{\min}$ as minimum radius. In the restricted area, the instantaneous outage probability of MU-MIMO transmissions in ad hoc networks does not exceed the threshold ε.

5. Numerical Results

In this section, we report the numerical results of computer simulations. In the HetNet, the coverage of cellular BS is assumed to be a circle area with 1 km radius. The UEs are located in the coverage area randomly. The simulation configurations are listed in Table 1.

Figure 2 shows the outage probabilities of MU-MIMO transmissions in cellular cell. With the increase of the intensity of ad hoc nodes, a UE experiences more severe cross-tier interference signals. On the other hand, the increasing

receiving UEs reduce the power of desired signal but may enhance the power of inter-beam interference signal. As a result, the outage probabilities of downlink MU-MIMO transmission in cellular cell increase with the intensity of the ad hoc nodes and the number of receiving UEs. Furthermore, because of the imperfect CSI feedback, the beams are prone to interfere with each other. The receiving UE will receive the inter-beam interference signal from other beams. Hence, the outage probabilities in case of imperfect CSI feedback are greater than those in case of perfect CSI feedback.

The outage probabilities of MU-MIMO transmissions in ad hoc networks in case of downlink interval and uplink interval in cellular cell are given in Figures 3 and 4, respectively. It is obvious that the number of receiving nodes and the SINR threshold have a significant effect on outage

probability. As described in Figure 2, the increase of the receiving nodes reduces the power of desired signal but enhances the power of inter-beam interference signal. Hence, the outage probability increases with the number of receiving nodes. On the other hand, the decrease of SINR threshold reduces the probability that the received SINR does not exceed the SINR threshold. Thus, the outage probability decreases accordingly.

As shown in Figure 3, when the distance between the cellular BS and a receiving node increases, the power of cross-tier interference signal the receiving node suffered is reduced. Hence, the outage probability decreases. However, if the distance exceeds a threshold, for instance 500 m, the effect of cross-tier interference signal is not significant. The outage probability decreases with the distance slowly. In Figure 4, the growth of UEs causes more severe cross-tier interference in case uplink interval in cellular cell. As a result, the outage probability increases with the number of UEs.

Note that there is a time gap between beam selection and data transmission in MU-MIMO transmission. A receiving node may perform SINR measurement and data transmission in different intervals of cellular cell. Since the cross-tier interference is different in downlink interval and uplink interval, the instantaneous SINR in data transmission may be different from the measured SINR. From Figures 3 and 4, the instantaneous outage probability may be different from the expected outage probability.

Figure 5 shows the relation between the radius of region area in cellular cell and the outage probability threshold. When a stricter threshold is imposed on the outage probability, i.e., the threshold decreases, the outage probability of more receiving ad hoc nodes could satisfy the threshold. Taking the distribution of ad hoc nodes into account, the nodes that are close to the cellular BS and could not meet the threshold are reduced. Hence, the restricted area in cellular cell becomes smaller. Furthermore, the decrease of the minimum distance between a pair of nodes enhances the power of desired signal but reduces outage probability. Consequently, the restricted area becomes smaller when the outage probability threshold is satisfied.

6. Conclusions

This paper investigates per-tier outage probability of MU-MIMO transmissions in HetNets with joint interference constraint. In the tier of cellular networks, a ZF-based precoding MU-MIMO scheme is employed. In the presence of cross-tier interference and unpredicted inter-beam interference, the closed-form expression of outage probability of downlink MU-MIMO transmissions is derived. Considering the capacity of ad hoc nodes, a max-SINR scheduler and codebook-based MU-MIMO transmission are applied. With the constraint of joint inter-node interference, inter-beam interference, and downlink/uplink cross-tier interference, the closed-form expression of outage probability in ad hoc networks is obtained. Furthermore, considering the QoS requirement of ad hoc networks in case of downlink interval, the restricted area in cellular cell is explored.

As a future work, the performance optimization of MU-MIMO transmissions using different interference management schemes is worthy of in-depth study.

Data Availability

The data used to support the findings of this study are available from the corresponding author upon request.

Conflicts of Interest

The authors declare that they have no conflicts of interest.

References

[1] P. Phaswana and M. Velempini, "Paper spectrum-aware transitive multicast on demand distance vector routing for military cognitive radio ad hoc networks," in *Proceedings of the 2019 IEEE AFRICON*, Accra, Ghana, September 2019.

[2] J. Liu and N. Kato, "A Markovian analysis for explicit probabilistic stopping-based information propagation in postdisaster ad hoc mobile networks," *IEEE Transactions on Wireless Communications*, vol. 15, no. 1, pp. 81–90, 2016.

[3] D. L. Guidoni, G. Maia, F. S. H. Souza, L. A. Villas, and A. A. F. Loureiro, "Vehicular traffic management based on traffic engineering for vehicular ad hoc networks," *IEEE Access*, vol. 8, pp. 45167–45183, 2020.

[4] Y. Zhong, T. Q. S. Quek, and X. Ge, "Heterogeneous cellular networks with spatio-temporal traffic: delay analysis and scheduling," *IEEE Journal on Selected Areas in Communications*, vol. 35, no. 6, pp. 1373–1386, 2017.

[5] J. Dai, W. Lv, and F. Ye, "Spectrum allocation scheme based on Stackelberg game in two-tier HetNet," in *Proceedings of the IEEE 13th International Conference Signal Process*, pp. 1270–1274, Chengdu, China, November 2016.

[6] H. B. Duk Kyung Kim and D. K. Kim, "Power control of femtocells based on max-min fairness in heterogeneous networks," *IEEE Communications Letters*, vol. 17, no. 7, pp. 1372–1375, 2013.

[7] K. Song, B. Ji, Y. Huang, M. Xiao, and L. Yang, "Performance analysis of heterogeneous networks with interference cancellation," *IEEE Transactions on Vehicular Technology*, vol. 66, no. 8, pp. 6969–6981, 2017.

[8] W. Zhang and S. Jiang, "Effect of node mobility on MU-MIMO transmissions in mobile ad hoc networks," *Wireless Communications and Mobile Computing*, vol. 2021, Article ID 9954940, 9 pages, 2021.

[9] S. Lee, S. Kim, Y. Park, S. Choi, and D. Hong, "Effect of unpredictable interference on MU-MIMO systems in Het-Net," *IEEE Access*, vol. 6, pp. 28870–28876, 2018.

[10] H. Kusumoto, H. Okada, K. Kobayashi, and M. Katayama, "Performance comparison between single-user MIMO and multi-user MIMO in wireless mesh networks," in *Proceedings of the 2012 15th International Symposium on Wireless Personal Multimedia Communications*, Taipei, Taiwan, September 2012.

[11] T. Erpek, Y. E. Sagduyu, Y. Shi, and S. Ponnaluri, "Rate optimization with distributed network coordination of multiuser MIMO communications," in *Proceedings of the 2018 IEEE 88th Vehicular Technology Conference (VTC-Fall)*, Chicago, IL, USA, August 2018.

[12] L. Liu, R. Chen, S. Geirhofer, K. Sayana, Z. Shi, and Y. Zhou, "Downlink MIMO in LTE-advanced: SU-mimo

vs. MU-MIMO," *IEEE Communications Magazine*, vol. 50, no. 2, pp. 140–147, 2012.

[13] R. V. Nee, "Breaking the gigabit-per-second barrier with 802.11ac," *IEEE Wireless Communications*, vol. 18, no. 2, p. 4, 2011.

[14] F. Kettlun, F. Rosas, and C. Oberli, "A low-complexity channel training method for efficient SVD beamforming over MIMO channels," *EURASIP Journal on Wireless Communications and Networking*, vol. 2021, no. 1, pp. 1–22, 2021.

[15] R. Yao, H. Nan, J. Xu, and G. Li, "Optimal BD-ZF precoder for multi-user MIMO downlink transmission," *Electronics Letters*, vol. 51, no. 14, pp. 1121–1123, 2015.

[16] K. M. Rege, K. Balachandran, J. H. Kang, and K. Karakayali, "Interference mitigation in heterogeneous networks with simple dirty paper coding," *Wireless Networks*, vol. 26, no. 4, pp. 2755–2767, 2020.

[17] J. L. Vicario, R. Bosisio, C. Anton-Haro, and U. Spagnolini, "Beam selection strategies for orthogonal random beamforming in sparse networks," *IEEE Transactions on Wireless Communications*, vol. 7, no. 9, pp. 3385–3396, 2008.

[18] J. Kingman, *Poisson Processes*, Oxford Univ. Press, London, UK., 1993.

[19] V. Chandrasekhar, M. Kountouris, and J. G. Andrews, "Coverage in multi-antenna two-tier networks," *IEEE Transactions on Wireless Communications*, vol. 8, no. 10, pp. 5314–5327, 2009.

[20] M. Haenggi, J. G. Andrews, F. Baccelli, O. Dousse, and M. Franceschetti, "Stochastic geometry and random graphs for the analysis and design of wireless networks," *IEEE Journal on Selected Areas in Communications*, vol. 27, no. 7, pp. 1029–1046, 2009.

[21] B. Blaszczyszyn, P. Mühlethaler, and Y. Toor, "Stochastic analysis of ALOHA in vehicular ad-hoc networks," *Annals of Telecommunications*, vol. 68, no. 1-2, pp. 95–106, 2013.

[22] F. Baccelli and A. Biswas, "On scaling limits of power law shot-noise fields," *Stochastic Models*, vol. 31, no. 2, pp. 1–17, 2014.